Ultrafast Spectroscopy of Non-Markovian Dynamics in a Dense Atomic Vapor

by

Virginia O. Lorenz

B.A., University of Colorado, 2001

M.S., University of Colorado, 2005

A thesis submitted to the
Faculty of the Graduate School of the
University of Colorado in partial fulfillment
of the requirements for the degree of
Doctor of Philosophy
Department of Physics
2007

This thesis entitled:
Ultrafast Spectroscopy of Non-Markovian Dynamics in a Dense Atomic Vapor
written by Virginia O. Lorenz
has been approved for the Department of Physics

Steven T. Cundiff

Chris H. Greene

Date

The final copy of this thesis has been examined by the signatories, and we find that both the content and the form meet acceptable presentation standards of scholarly work in the above mentioned discipline.

Lorenz, Virginia O. (Ph.D., Physics)

Ultrafast Spectroscopy of Non-Markovian Dynamics in a Dense Atomic Vapor

Thesis directed by Prof. Steven T. Cundiff

This thesis presents results from ultrafast spectroscopy experiments and theoretical calculations of non-Markovian dynamics in a dense atomic vapor. For a dense atomic vapor the excitation pulses are short compared to the duration of collisions and the time between collisions is long compared to the collision duration. Thus there are distinct timescales that correspond to regimes in which the phase-coherence of the atomic superpositions is retained (called the non-Markovian regime) and regimes in which the phase memory is lost (called the Markovian regime). This is not the case for most condensed phase systems, in which the time between dephasing interactions, the interaction duration and the pulse width are of similar order. Using the current theory of stochastic fluctuations of the energy levels due to collisions, we simulate and fit the signatures of phase memory from two-pulse transient four-wave mixing experiments, providing support for the theoretical model that is commonly used for more complex condensed phase systems. Further three-pulse experiments in conjunction with a theoretical derivation of the correlation function of frequency fluctuations using molecular dynamics simulations in an exciton picture provide insight into resonant effects in dense atomic vapors. In addition, distinct signatures of local field effects are observed and compared with theory. The results presented in this thesis provide support for theoretical models employed in more complex systems, contribute insight into the fundamental physics of dense atomic vapors, and exhibit the benefits of ultrafast spectroscopic techniques through the clarity of signatures representing system response.

Dedication

This thesis is dedicated to my parents.

Acknowledgements

I would like to thank Professor Steve Cundiff for being an excellent advisor, a sensitive mentor and an honest counselor. I deeply appreciate his uplifting words and steadfast support, which opened up opportunities for scientific growth and achievement I never could have imagined.

I am very thankful to Professor Chris Greene and Professor Shaul Mukamel for their inspiration, encouragement and generous support. I would also like to thank my other committee members Professor Eric Cornell, Professor Ralph Jimenez, Professor Allan Franklin and Professor John Bohn for their support and helpful comments.

From the many JILA staff members who helped me I would like to especially thank Hans Green and Todd Asnicar, who brought essential expertise and optimistic tenacity to numerous technical hurdles. I also thank Loree Kaleth for her administrative assistance. I would like to thank the Cundiff group members, past and present, as well as my graduate colleagues for their friendship and aid.

To my parents I owe a lifetime of thanks for their love, prayers and for guiding me towards wisdom and knowledge. To them and my brother, thank you for blessing my life. I give my utmost thanks to God.

Contents

Chapter

Appendix

Tables

Table

Figures

Figure

Chapter 1

Introduction

The research presented in this thesis falls under the general heading of "atomic, molecular and optical physics." This field encompasses the study of light-matter interaction on the atomic scale. The particular set of experiments described in this thesis allows us to focus on how the electronic state of a dense atomic vapor changes with time. In the experiments, an ultrashort pulse of light impinges on a dense vapor of atoms at a resonant frequency, exciting electrons into superpositions between a ground state and an excited state. Soon the electron superpositions become "out of sync," or dephase, due to changes in the atomic energy levels from collisions. These changes are a form of quantum dissipation, meaning they are not reversible. Probing with sequences of ultrashort laser pulses results in a representation of the dephasing process even as it begins, a regime of quantum dissipation often referred to as non-Markovian dynamics. This topic of ultrafast spectroscopy of non-Markovian dynamics in a dense atomic vapor is the primary focus of this thesis. A closely related phenomenon in which the emitted light is redshifted due to the high density of atoms, known as the local field effect, constitutes a secondary aspect of this thesis.

1.1 Historical Background and Overview of Main Results

This thesis research applies the relatively modern technique of ultrafast spectroscopy to the mature field of atomic vapors, resulting in an unusual perspective on dense vapors as well as ultrafast techniques and the systems to which they are commonly applied. In particular, the research of this thesis contributes to understanding the fundamental physics of atomic vapors, provides support to theoretical treatments commonly applied in condensed phase systems, and exhibits the benefits of ultrafast techniques through the clarity of signatures representing system response. An overview of the research including some historical background is given in this section.

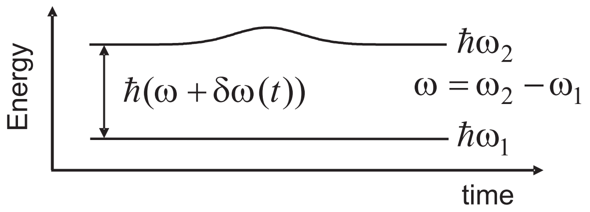

Figure 1.1: A schematic of the ground state and excited state energy levels of an atom undergoing a collision. During the collision the transition frequency fluctuates by a time-dependent amount $\delta\omega(t)$.

This thesis research is related to the more general question of how to model quantum dissipation [1]. Quantum dissipation generally refers to the irreversible loss of order in quantum systems. In an atomic vapor, the cause of quantum dissipation is atomic collisions. During a collision, the resonance frequency of an atom fluctuates, as shown in Fig. 1.1. A collision can be thought of as the transient formation of a dimer, with the amplitude of the resonance fluctuation in principle determined by the interatomic potential energy surfaces of the dimer. If we consider the superposition between ground and excited state as a function of time, shown in Fig. 1.2, the effect of the collision is to create a phase difference between the superpositions of an atom that has undergone a collision and one that has not undergone a collision. This loss of phase coherence is known as dephasing. If we overlay the superpositions of an unperturbed and perturbed atom (see Fig. 1.2), we can define the correlation time t_c as the time it takes for a perturbed atom to become out of phase with an unperturbed atom. The correlation time is a measure of the phase memory of the system, representing how long an atom can retain approximately the same phase as an unperturbed atom. In physics literature, dynamics which occur on timescales less than the correlation time are termed non-Markovian dynamics, while those which occur in timescales much greater than the correlation time are termed Markovian dynamics[1] . For non-Markovian dynamics the phase coherence is retained such that the evolution of the superpositions of the atoms is reversible. Conversely, for Markovian dynamics the phase coherence of the system is lost over the timescale of interest due to the randomization of the phases of the superpositions due to collisions, making the evolution irreversible. Stated from an experimental perspective, non-Markovian dynamics arise in experiment whenever the finite duration of collisions must be taken into account, while dynamics are Markovian whenever collisions can be considered to occur infinitely fast.

Historically, the effects of non-Markovian dynamics on frequency-domain lineshapes attracted interest about a century after the first studies of spectral emission lines in the mid-1800's. After decades of improving the technique of white-light spectroscopy, in the 1920's pressure-broadened lineshapes were resolved for a number of atomic vapors and theoretical treatments began to elucidate the underlying physics [2]. Initially, theories which approximated collisions between atoms and perturbers as infinitely fast in what is known as the impact

---

[1] The term “Markovian” is used because of its relationship to time evolution determined solely by the instantaneous state of the system. A more thorough definition is given in Ch. 2.

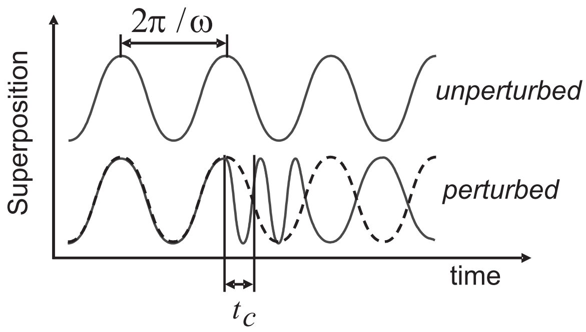

Figure 1.2: The superposition between a ground state and excited state as a function of time for an uperturbed (top) and perturbed (bottom) atom. The correlation time t_c is the time it takes for a perturbed atom to become out of phase with an unperturbed atom.

approximation were sufficient to describe the majority of experiments, with good agreement for linewidths at low densities.

Studies took on new emphasis with the improved intensities and spectral resolution provided by the advent of the laser in the 1960's. Initially, theoretical treatments employing the impact approximation were still sufficient to explain most experimental results [3, 4]. Starting in the 1970's, predictions were made for signatures of the finite duration of collisions to be manifested in frequency-domain lineshapes as a deviation from Lorentzian form, both near line center and at detunings from resonance on the order of the inverse duration of a collision [5]. These were quickly verified experimentally [6, 7]. A non-impact theory of the technique of frequency-domain four-wave mixing (FWM) was presented in 1986, and FWM experiments revealed non-impact behavior in the wings of helium-broadened sodium vapor lineshapes in 1989 [8, 9].

Because collisions occur on short timescales their frequency-domain manifestation is most dominant in the wings of the absorption lineshape [10]. Thus frequency-domain experiments are limited in their ability to probe the fastest dynamics by the inherently low signal-to-noise ratio and influence of other resonances in the wings of absorption lineshapes. This is in contrast to time-domain experiments in which the fastest dynamics dominate at short times and with high signal-to-noise ratio. In addition, unlike lineshapes, which are integrated over many collision durations, time-domain techniques can separate short timescales from long ones, providing a different perspective from frequency-domain studies of fast dynamics.

Time-domain techniques began with the first applications of pulsed lasers to spectroscopy in the 1970's and the development of the theory of transient nonlinear optics [11]. However, applications of ultrafast spectroscopy were made largely in condensed phase systems, with only a few ultrafast experiments in dense atomic vapors, which mainly studied propagation effects in transmission [12]. Initially the theory for ultrafast spectroscopy was based on the optical Bloch equations, which relied on the impact approximation [13, 14]. Once sub-picosecond probes of relaxation phenomena began revealing ultrafast dynamics in the 1980's theoretical treatments were proposed that modified the optical Bloch equations to include the finite duration of interactions, with a unified approach to transient nonlinear optical phenomena using Liouville operators published in 1983 [15, 16]. Ultrafast nonlinear spectroscopy is now commonly applied to such intricate systems as biological light-harvesting complexes to result in an incredibly sophisticated understanding of their structure and dynamics [17]. In molecular systems, studies of non-Markovian interactions of atoms in molecules and between molecules and solvents have provided detailed inter- and intramolecular information, such as how bonds stretch and molecules conform [18, 19].

One of the main difficulties in ultrafast molecular studies is the dephasing caused by interactions of the molecules with the solvent. These experiments are usually performed in liquid solutions, where the solvent-solute interactions often occur at femtosecond time scales, causing ultrafast dephasing, which obscures the non-Markovian dynamics at short times [20, 21, 22, 23]. In these experiments it is also common to have dephasing times on the order of the pulse duration. In contrast, in a dense atomic vapor the pulse duration, collision duration and dephasing time are all well-separated, making dense atomic vapors ideal systems in which to apply ultrafast spectroscopy to the study of non-Markovian dynamics.

Considering the above opportunities for contribution, we study the phase relaxation dynamics of a dense potassium vapor using ultrafast spectroscopy. The experimental results exhibit signatures characteristic of both Markovian and non-Markovian dynamics, which can be modeled using the non-Markovian theory commonly applied to more complex systems [15]. Studying such a model system lends support to the use of the non-Markovian theory. Through further experiments in conjunction with detailed theoretical derivations we also gain insight into long-range interactions in resonance-broadened vapors. This work contributes to the understanding of excitonic interactions in dense media in general and a resonance-broadened vapor in particular. The research described in this thesis takes advantage of the simple electronic structure and tunable density of dense atomic vapors to exhibit the benefits of ultrafast spectroscopic techniques through the clarity of signatures representing system response. Finally, we show that with time-domain techniques we are able to probe other effects that have proven difficult to separate from competing factors in the frequency domain, such as the local field effect.

1.2 Thesis Organization

This thesis is organized as follows. Chapter 2 includes an introduction to the ultrafast technique of transient four-wave mixing, which is a general technique that encompasses the experiments of this thesis. The density matrix formalism is described, leading to a derivation of the optical Bloch equations for homogeneously broadened and static inhomogeneously broadened systems. It is shown that the optical Bloch equations apply the impact approximation. Then the theory including non-Markovian dynamics is presented, which is used to model the two-pulse experimental results in the next chapter.

Chapter 3 contains the experimental setups and results. First the experimental components are described. Then the two-pulse TFWM experiment and results are presented along with fits from the non-Markovian theory derived in the previous chapter. The three-pulse and time-resolved experimental setups and results are then presented. Although the data for low temperatures and densities supports the theoretical treatment used in the two-pulse results, the higher temperature and density three-pulse data exhibits bi-exponential behavior that requires a more detailed analysis, presented in the next chapter.

Chapter 4 describes a theoretical approach to modelling the three-pulse results that derives the correlation function of frequency fluctuations in an exciton picture based on molecular dynamics simulations. First an introduction is made to the exciton formalism, then a description of the molecular dynamics simulation is given, followed by the procedure of determining the correlation functions and the calculated correlation functions and three-pulse photon echo peak shifts.

Chapter 5 describes the local field effect, with a derivation of the local field effect in the frequency-domain and time-domain, followed by experimental results and some preliminary calculations of propagation effects.

In the conclusion, Ch. 6, future ideas for buffer gas and transmission experiments are presented along with a summary of main results.

Appendices A-B.3 provide derivation details for Ch. 2. In particular, App. A covers the details of the derivation of the optical Bloch equations for a two-level system, App. B.1 describes the use of Feynman diagrams, App. B.2 provides details of the cumulant expansion and App. B.3 gives further response function derivation results.

Appendices C-E supplement the experimental chapter. App. C lists some attributes of potassium for reference. App. D describes the pulse picker mentioned in the experimental chapter and other experimental components. App. E describes the design and manufacture of the novel vapor cells used in the experiments.

App. F supplements Ch. 4 by providing the derivation of the exciton Hamiltonian for a 2-level system, while App. G gives detailed information about how to run the molecular dynamics package GROMACS.

Finally, App. H lists some useful constants and conversions.

Chapter 2

Theoretical Background for Transient Four-Wave Mixing Experiments

In order to provide a basis for interpreting the experimental results presented in this thesis, in this chapter an overview of the signatures of non-Markovian dynamics in a dense atomic vapor is presented. We start with a description of the transient four-wave mixing process and the fundamentals of nonlinear optics. The density matrix formalism is then presented to facilitate the theoretical derivations of the material response through the optical Bloch equations. First the cases of homogeneously broadened and static inhomogeneously broadened systems are considered and compared. Then it is shown that the typical optical Bloch derivation of the homogeneously broadened system response makes the Markov approximation for the dephasing process. Finally the theory that allows us to take non-Markovian dynamics into account is presented and distinctions are drawn between the signatures of non-Markovian dynamics and those of homogeneously and static inhomogeneously broadened systems. The derivation of the non-Markovian system response is carried out in detail for a three-level system and is the theoretical basis for much of the theoretical fitting made to the experimental data of this thesis.

2.1 Transient Four-Wave Mixing

Transient four-wave mixing (TFWM) is a time-domain spectroscopic technique used to study dynamics in a variety of systems. TFWM occurs when three input pulses of either the same or different frequencies successively excite a medium. The radiative output, which is the fourth wave, depends on the time sequence and separation of the input pulses. For the experiments presented in this thesis the field frequencies are degenerate, and thus we will only consider the degenerate case for the following derivations.

In the degenerate transient four-wave mixing process, three pulses with wavevectors $\mathbf{k}_1$, $\mathbf{k}_2$ and $\mathbf{k}_3$ and degenerate frequencies $\omega_1 = \omega_2 = \omega_3$ are incident on a material sample. Figure 2.1 is a schematic of TFWM. The first pulse, with wavevector $\mathbf{k}_1$, induces a polarization in the sample with a spatial phase across the vapor determined by its angle of incidence and wavelength. After some delay τ, the second pulse, $\mathbf{k}_2$, produces an excited state population whose amplitude is greatest in areas where the polarization left by the first pulse constructively interferes with the second pulse and least where they destructively interfere. Thus the excited state population is spatially modulated, forming an amplitude grating with periodicity $\mathbf{k}_2 - \mathbf{k}_1$. After a second delay T the third pulse, $\mathbf{k}_3$, scatters off the grating (i.e. creates a polarization that radiates) into the new direction $\mathbf{k}_3 + \mathbf{k}_2 - \mathbf{k}_1$.

By varying the relative delay between pulse $\mathbf{k}_1$ and $\mathbf{k}_2$, or pulse $\mathbf{k}_2$ and $\mathbf{k}_3$, the excited state dynamics of the system can be investigated. In particular, if the time delay between pulse $\mathbf{k}_1$ and $\mathbf{k}_2$, τ, is varied, the transient behavior of the induced polarization can be investigated. If the time delay between pulse $\mathbf{k}_2$ and $\mathbf{k}_3$, T, is varied, the transient behavior of the excited state population can be investigated. Stated another way, varying the time delay between pulses allows a characterization of the evolution of the intermediate density matrix states (described below). If the pulses are weak, the density matrix equations of motion can be expanded to third order in the field. As the fact that the signal is radiated in a new direction attests, the signal is generated completely by the nonlinear polarization. Thus the detected signal energy is proportional to the square of the third-order nonlinear polarization. Varying the first delay τ probes the off-diagonal density matrix elements ρ_{nm} representing the coherent superposition created between states n and m, while varying the second delay T probes the density matrix elements ρ_{nn} representing population and, in the case of a three-level system, ρ_{nm} representing Raman coherence [24]. It is from this density matrix expansion in orders of the field that the language used above, referring to the sequence, polarization (first-order) – population (second-order) – polarization (third-order), stems.

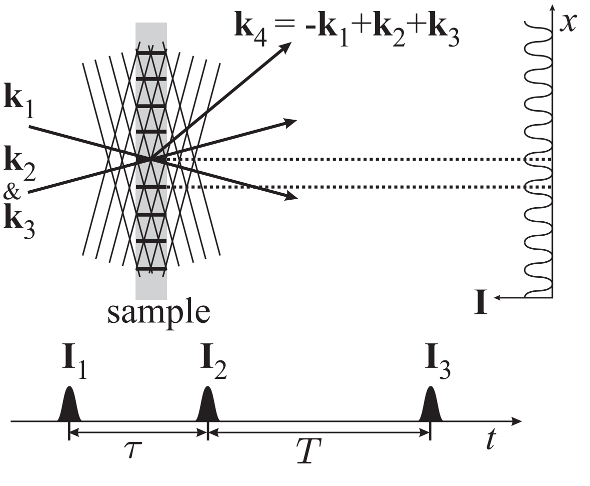

Figure 2.1: Schematic of transient four-wave mixing. The phase fronts of pulses $\mathbf{k}_1$ and $\mathbf{k}_2$ are depicted with lines perpendicular to the wavevectors. The resulting excited state population has an amplitude I which varies spatially across the sample. The dark bars across the sample represent the maxima of the excited state population grating. At the bottom of the diagram are the pulses labeled by their intensities, shown as they are delayed in time.

It is clear from this description that to predict the response of the material to the fields requires an understanding of how the polarization is coupled to the fields. The relationship between the material polarization and the incident fields is described by the Maxwell equations. In particular, the nonlinearity of the material is contained in the relation

$$\mathbf{D} = \mathbf{E} + 4\pi\mathbf{P}, \tag{2.1}$$

where the polarization $\mathbf{P}$ (dipole moment per unit volume) depends nonlinearly on the electric field $\mathbf{E}$ and contains all the information concerning the response of the medium to the field in what is known as the constitutive equation. If this equation were known, it would then be possible to find the solution of the Maxwell equations with appropriate boundary conditions for any field and material system. The constitutive equation is complicated, however, and therefore we must make approximations.

If the incident field is sufficiently weak[1] , it is appropriate to express the polarization $\mathbf{P}$ as a power series in the field strength $\mathbf{E}$ [25]. We do this specifically to third-order with three different incident fields to represent degenerate TFWM:

$$\mathbf{P}(\mathbf{k},\omega) = \mathbf{P}^{(1)}(\mathbf{k},\omega) + \mathbf{P}^{(2)}(\mathbf{k},\omega) + \mathbf{P}^{(3)}(\mathbf{k},\omega)$$

with

$$\begin{aligned}
\mathbf{P}^{(1)}(\mathbf{k},\omega) &= \chi^{(1)}(\omega) \cdot \mathbf{E}(\mathbf{k}_1,\omega), \\
\mathbf{P}^{(2)}(\mathbf{k},\omega) &= \chi^{(2)}(\omega) : \mathbf{E}(\mathbf{k}_1,\omega)\mathbf{E}(\mathbf{k}_2,\omega), \\
\mathbf{P}^{(3)}(\mathbf{k},\omega) &= \chi^{(3)}(\omega) : \mathbf{E}(\mathbf{k}_1,\omega)\mathbf{E}(\mathbf{k}_2,\omega)\mathbf{E}(\mathbf{k}_3,\omega),
\end{aligned} \tag{2.2}$$

where $\chi^{(n)}$ is the nth-order nonlinear susceptibility, a tensor of rank $(n + 1)$. In Eq. 2.3 the variable ω in the susceptibilities implies that each order of the polarization contains a sum over all the possible frequency combinations, including

---

[1] A loose definition of "sufficiently weak" is that the incident field is much less than the characteristic atomic field strength $E_{at} = e/a_0^2$, where $-e$ is the charge of the electron and a_0 is the Bohr radius of hydrogen.

negative frequencies, for that order. In addition, the dependence of the nth-order polarization $\mathbf{P}^{(n)}$ on wavevector $\mathbf{k}$ means that each order of the polarization contains a sum over all the possible combinations of wavevectors $\mathbf{k}_1 \dots \mathbf{k}_3$. The susceptibility (and therefore the polarization) is determined by the physical microscopic structure of the medium, and so it must be derived using quantum mechanics. Thus if we wish to understand the response of a medium to third order in the field, as we do in TFWM, we must find a way of deriving the third-order polarization. Because in general a medium will be made up of many components in different states, the density matrix formalism, which employs ensemble averages over the states, proves useful for this task.

2.2 Density Matrix Formalism

The physical properties of a material system can in general be described with a wavefunction $\psi(\mathbf{r}, t)$. The wavefunction obeys the Schrödinger equation $i\hbar(\partial\psi(\mathbf{r}, t)/\partial t) = H\psi(\mathbf{r}, t)$, and therefore its time evolution and observable properties can be fully determined. For an ensemble system of quantum objects each with state i, it is convenient to use the density matrix formalism, which gives a statistical description of the system. The density matrix operator of the system is then defined as the ensemble average of the outer product of each state vector of the system with itself. The average is over all of the possible states of the system, each state i having a probability weight w_i:

$$\rho \equiv \sum_i w_i |i\rangle\langle i| = \overline{|i\rangle\langle i|}. \tag{2.3}$$

The corresponding density matrix elements ρ_{nm} give the probability of the system to be in a certain physical state. This becomes clear if we use the eigenkets $|n\rangle$ of the system as the base kets of all the states, $|i\rangle = \sum_n a_n^i |n\rangle$. Then the diagonal elements $\rho_{nn} = \langle n|\rho|n\rangle = \overline{|a_n|^2}$ give the probability that the system is in energy eigenstate n. The off-diagonal elements $\rho_{nm} \equiv \langle n|\rho|m\rangle = \overline{a_n a_m^*}$ give the coherence between the levels n and m, that is, ρ_{nm} is nonzero only if the system is in a coherent superposition of the energy eigenstates n and m.

With the density matrix operator we can calculate the ensemble-averaged value of any observable quantity, including the polarization $\mathbf{P}$:

$$[\mathbf{P}] \equiv \sum_i w_i \langle i|\mathbf{P}|i\rangle = \sum_n \sum_m \langle n|\rho|m\rangle\langle m|\mathbf{P}|n\rangle = Tr(\rho\mathbf{P}). \tag{2.4}$$

To find how the expectation value of an observable quantity evolves with time in the system, it is sufficient to determine how the density matrix evolves in time. Because the wavefunction $|\psi\rangle$ obeys the Schrödinger wave equation, we can also find the equation of motion for ρ. Thus

$$\begin{aligned} \frac{\partial \rho}{\partial t} &= \sum_j w_j (|\dot{\psi_j}\rangle\langle\psi_j| + |\psi_j\rangle\langle\dot{\psi_j}|) = \frac{1}{i\hbar}\sum_j w_j (H|\psi_j\rangle\langle\psi_j| + |\psi_j\rangle\langle\psi_j|H) \\ &= \frac{1}{i\hbar}(H\rho - \rho H) = \frac{1}{i\hbar}[H, \rho]. \end{aligned} \tag{2.5}$$

The Hamiltonian H typically consists of two terms,

$$H = H_0 + H_{int}, \tag{2.6}$$

where H_0 is the Hamiltonian of the unperturbed system and H_{int} represents the interaction of the fields with the system. In the basis of the energy eigenfunctions, H_0 is diagonal and therefore $[H_0, \rho]_{nm} = (\epsilon_n - \epsilon_m)\rho_{nm}$, where ϵ_j is the energy of state j. In the electric dipole approximation in which the spatial dimension of the atom is considered much smaller than the incident wavelength, the electronic interaction Hamiltonian is given by $H_{int} = -\mu \cdot \mathbf{E}(t)$, where $\mu = -e\mathbf{r}$ is the electric dipole moment operator of the atom and $\mathbf{E}(t)$ is the incident field.

The equation of motion as it stands does not account for dissipative processes such as dephasing due to collisions and population decay. It is common to add phenomenological terms to the equation of motion that represent decay processes, using the assumption $\left(\frac{\partial \rho_{nm}}{\partial t}\right)_{relax} = \gamma_{nm}(\rho_{nm} - \rho_{nm}^{eq})$, where ρ_{nm}^{eq} is the equilibrium value to which ρ_{nm} relaxes at rate γ_{nm}, with $\rho_{nm}^{eq} = 0$ for $n \neq m$, corresponding to the inability of incoherent thermal processes to produce coherent superpositions of atomic states. Here γ_{nm} corresponds to the population relaxation rate T_1^{-1} if the state is diagonal or the dephasing rate T_2^{-1} if the state is off diagonal. Although the population decay term can be justified by quantizing the field [13], adding phenomenological dephasing terms is equivalent to making the Markov approximation for the coherence decay process, as will be shown below.

Thus the final form of the density matrix equation of motion including phenomenological decay terms is

$$\dot{\rho}_{nm} = -i\omega_{nm}\rho_{nm} - \frac{i}{\hbar}[-\mu \cdot \mathbf{E}(t), \rho]_{nm} - \gamma_{nm}(\rho_{nm} - \rho_{nm}^{eq}), \tag{2.7}$$

where $\omega_{nm} \equiv (E_n - E_m)/\hbar$ is the transition frequency. Because of the similarity of this formalism with that used to describe a spin-one-half particle in a magnetic field, these equations of motion are termed the optical Bloch equations[2] .

To find the polarization $\mathbf{P}$ using the density matrix via Eq. 2.4, we must first solve the density matrix equation of motion, Eq. 2.7. This is generally not possible to do exactly, and thus we consider a perturbative approach.

For weak fields an expansion can be made in terms of the interaction Hamiltonian, replacing H_{int} by λH_{int}, where λ ranges from zero to one to characterize the strength of the perturbation. The solution of Eq. 2.7 is then in the form of a power series in λ:

$$\rho_{nm} = \rho_{nm}^{(0)} + \lambda\rho_{nm}^{(1)} + \lambda^2\rho_{nm}^{(2)} + \lambda^3\rho_{nm}^{(3)}. \tag{2.8}$$

For Eq. 2.8 to be a solution of Eq. 2.7 for all values of λ, the coefficients of each

---

[2] The Bloch equations were initially developed by Bloch to simulate nuclear magnetic resonance experiments [14, 26]. They were later extended to provide a quantum-mechanical model of the coherent response of a dilute atomic vapor to a laser field. In this context the equations are called the optical Bloch equations [13, 14].

power of λ must satisfy Eq. 2.7 individually. The solutions starting with first order all take the same form; we obtain for the qth-order equation of motion

$$\dot{\rho}_{nm}^{(q)} = -(i\omega_{nm} + \gamma_{nm})\rho_{nm}^{(q)} - \frac{i}{\hbar}[-\mu \cdot \mathbf{E}(t), \rho^{(q-1)}]_{nm}. \tag{2.9}$$

This system of equations can be integrated directly because each equation uses previously solved orders and contains only linear terms of the current order. The qth-order solution is

$$\rho_{nm}^{(q)}(t) = -\frac{i}{\hbar}\int_{-\infty}^{t} dt' e^{(i\omega_{nm}+\gamma_{nm})(t'-t)}[-\mu \cdot \mathbf{E}(t'), \rho^{(q-1)}]_{nm}. \tag{2.10}$$

In the case of transient four-wave mixing, the third-order polarization is the quantity of interest. Following the above derivation, this means we must find the third-order solution to the density matrix equation of motion, $\rho^{(3)}$, and take the trace of its product with the polarization operator $\mathbf{P}(\omega) = N\mu$:

$$[\mathbf{P}^{(3)}]_{mn} = N\mathrm{Tr}(\rho^{(3)}\mu)_{mn}. \tag{2.11}$$

2.3 Optical Bloch Equations for Homogeneously and Static Inhomogeneously Broadened Systems

To make the physics of the polarization conceptually transparent let us first consider a two-level atomic system, with a ground state a and excited state b. We will consider both a homogeneously broadened system as well as a static inhomogeneously broadened system in order to form a basis of comparison with the theoretical approach to non-Markovian dephasing. Let there be only two incident fields, such that the second pulse $\mathbf{k}_2$ creates both the second-order population and third-order polarization. The incident fields are of the form $\mathbf{E}_i(\mathbf{r}, t) = \frac{1}{2}E_i(t)\mathrm{e}^{i(\mathbf{k}_i\cdot\mathbf{r}-\omega t)} + \text{c.c.}$, $i = 1, 2$, with ω nearly resonant with the atomic transition frequency $\omega_0 = \omega_b - \omega_a$. We specify that the third-order polarization of interest is in the direction $\mathbf{k}_4 = 2\mathbf{k}_2 - \mathbf{k}_1$.

The equations of motion $\rho_{ba} = \rho_{ab}^*$ and $\rho_D = \rho_{aa} - \rho_{bb}$ from Eq. 2.9 then become in the rotating wave approximation (see App. A for details)

$$\begin{aligned}\hat{\rho}_{ba}^{(n)}(\mathbf{r},t) &= \frac{i\mu_{ba}}{\hbar}\exp\big[-(\frac{1}{T_2}+i\Delta\omega)t\big] &(2.12)\\ &\times\int_{-\infty}^{t}\mathbf{E}(\mathbf{r},t')\rho_D^{(n-1)}\exp\left[\left(\frac{1}{T_2}+i\Delta\omega\right)t'\right]dt' \\ \rho_D^{(n)}(\mathbf{r},t) &= \frac{2i\mu_{ba}}{\hbar}\exp\left(-\frac{t}{T_1}\right) &(2.13)\\ &\times\int_{-\infty}^{t}\{-\mathbf{E}(\mathbf{r},t')\hat{\rho}_{ab}^{(n-1)}+\mathbf{E}^*(\mathbf{r},t')\hat{\rho}_{ba}^{(n-1)}\}\exp\left(\frac{t'}{T_1}\right)dt',\end{aligned}$$

where $\Delta\omega = \omega_0 - \omega$ and $\hat{\rho}_{ba}^{(n)} = \rho_{ba}^{(n)}\exp(i\omega t)$.

Choosing the third-order coherence only in the direction $\mathbf{k}_4 = 2\mathbf{k}_2 - \mathbf{k}_1$ results in (details in App. A)

$$\begin{aligned}&\hat{\rho}_{ba}^{(3)}(\mathbf{k}_4) = &(2.14)\\ &\quad -2i\rho^{(0)}\left(\frac{\mu_{ba}}{\hbar}\right)^3\exp\big[-(\frac{1}{T_2}+i\Delta\omega)t+i\mathbf{k}_4\cdot\mathbf{r}\big]\int_{-\infty}^{t}\int_{-\infty}^{t'}\int_{-\infty}^{t''}dt'dt''dt''' \\ &\quad\times\big\{\mathbf{E}_2(\mathbf{r},t')\mathbf{E}_2(\mathbf{r},t'')\mathbf{E}_1^*(\mathbf{r},t''')\exp\big[\gamma(t'-t'')+\frac{t'''}{T_2}+i\Delta\omega(t'+t''-t''')\big] \\ &\quad+\mathbf{E}_2(\mathbf{r},t')\mathbf{E}_1^*(\mathbf{r},t'')\mathbf{E}_2(\mathbf{r},t''')\exp\big[\gamma(t'-t'')+\frac{t'''}{T_2}+i\Delta\omega(t'-t''+t''')\big]\big\},\end{aligned}$$

where $\gamma = T_2^{-1} - T_1^{-1}$, $\mu_{ab} = \mu_{ba}$ and the population was assumed to start in the ground state, $\rho_D^{(0)} = \rho^{(0)}$, $\rho_{ba}^{(0)} = 0$.

We now consider delta-function field excitations separated by variable temporal delays. This assumption is valid when the pulse duration is much shorter than the decay times T_1 and T_2 as well as the inverse detuning $(\Delta\omega)^{-1}$. Then the field envelopes become $E_j(t) = \delta(t - t_j)$, $j = 1, 2$, where t_j is the pulse arrival time; we also assume on-resonance excitation and set $\omega = \omega_{ba}$.

For the case of a homogeneously broadened system, the phenomenological dephasing constants already account for the homogeneous width. Thus the polarization is $\mathbf{P}^{(3)}(\mathbf{r}, t) = \hat{\mathbf{P}}^{(3)}(\mathbf{r}, t)\exp(-i\omega t) + \text{c.c.}$, with

$$\hat{\mathbf{P}}^{(3)} = N\mu_{ab}\hat{\rho}^{(3)}_{ba}(\mathbf{r}, t, \omega_0), \tag{2.15}$$

where N is the number density. Substitution of Eq. 2.14 with delta-function pulses in the above equation yields the polarization in the homogeneous limit:

$$\hat{\mathbf{P}}^{(3)}(\mathbf{r}, t) = -i\rho^{(0)}CN\mu_{ba}\theta(t - t_2)\exp[i\mathbf{k}_4 \cdot \mathbf{r} - T_2^{-1}(t - t_1)] \tag{2.16}$$

where $\theta(t)$ is the Heaviside step function and C a constant.

We now consider the limit of the system being static inhomogeneously broadened [27]. In the case of an inhomogeneously broadened system, the product of the density matrix element and the inhomogeneous lineshape is integrated over frequency; thus $\hat{\mathbf{P}}^{(n)}$ becomes

$$\hat{\mathbf{P}}^{(n)} = N\int_0^\infty \mu_{ab}\hat{\rho}^{(n)}_{ba}(\mathbf{r}, t, \omega_0)g(\omega_0)d\omega_0, \tag{2.17}$$

where the lineshape function $g(\omega_0)$ obeys the normalizing condition $\int_0^\infty g(\omega_0)d\omega_0 = 1$.

To model static inhomogeneous broadening we employ a Gaussian form for the lineshape function, which is commonly used to represent the lineshape arising from a large number of frequencies (through application of the central limit theorem):

$$g(\omega_0) = (\sqrt{\pi}\delta\omega)^{-1}\exp[-(\omega_0 - \omega)^2/\Delta\omega^2]. \tag{2.18}$$

This results in a polarization given by

$$\begin{aligned}\hat{\mathbf{P}}^{(3)}(\mathbf{r}, t) =& \qquad\qquad (2.19)\\ &-i\rho^{(0)}DN\mu_{ba}\theta(t - t_2)\exp\big[i\mathbf{k}_4 \cdot \mathbf{r} - \frac{(t - t_1)}{T_2} - \frac{1}{4}(t - 2t_2 + t_1)^2(\Delta\omega)^2\big],\end{aligned}$$

where D is a constant. Note the homogeneous response can be retrieved by setting $\Delta\omega = 0$.

The behavior of the real-time signal as a function of delay is shown for the homogeneous case in Fig. 2.2 and the inhomogeneous case in Fig. 2.3. The real-time signal for the homogeneously broadened system is the free polarization decay, while for the static inhomogeneously broadened system it is the photon echo. In the latter case, the first pulse creates a coherent superposition between ground and excited state, which evolves according to each atom's resonance frequency until the second, conjugate pulse reverses the evolution to cause a rephasing, called the photon echo, the same delay later. The photon echo signal will have a width in time which is the inverse of the inhomogeneous width of the frequency distribution. Thus the pulses must be short, that is, wide in frequency such that they span the inhomogeneous width, for a photon echo to arise. An analogy is described in Fig. 2.4. The temporal behavior for both the homogeneous and static inhomogeneous limits are plotted in Fig. 2.5.

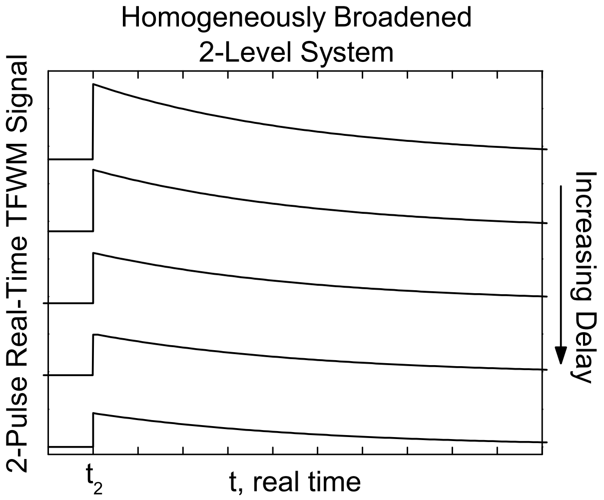

Figure 2.2: Calculated 2-pulse real-time TFWM signals for a homogeneously broadened system. The delay between pulses increases downward, with horizontal ticks spaced by the delay step size.

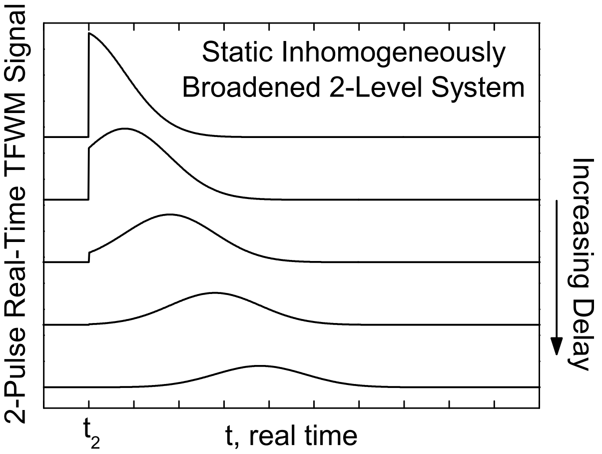

Figure 2.3: Calculated 2-pulse real-time TFWM signals for a static inhomogeneously broadened system. The delay between pulses increases downward, with horizontal ticks spaced by the delay step size.

The time-integrated signal is the integral over the square of the polarization:

$$\int_{-\infty}^{\infty} |\mathbf{P}^{(3)}(\mathbf{r},t)|^2 dt. \tag{2.20}$$

In the homogeneous limit the time-integrated signal is

$$J = A\theta(t-(t_2-t_1))\exp\left[-\frac{2}{T_2}(t_2-t_1)\right] \tag{2.21}$$

where A is a proportionality constant independent of $t_2 - t_1$.

The time-integrated signal for an inhomogeneously broadened system is

$$J = B\theta(t-t_2-t_1)\exp\left[-\frac{4}{T_2}(t_2-t_1)\right]\left\{1+\Phi\left[\frac{\Delta\omega}{\sqrt{\pi}}(t_2-t_1)\right]\right\} \tag{2.22}$$

where B is a proportionality constant independent of $t_2 - t_1$ and $\Phi(x) \equiv \frac{2}{\sqrt{\pi}}\int_0^{\pi} e^{-t^2}dt$.

The time-integrated behavior for both types of broadening is shown in Figs. 2.6 and 2.7. The decay of the TFWM signal for both the inhomogeneous and homogeneous cases is directly related to the dephasing of the coherent superposition between the ground and excited state. For the case of a homogeneously

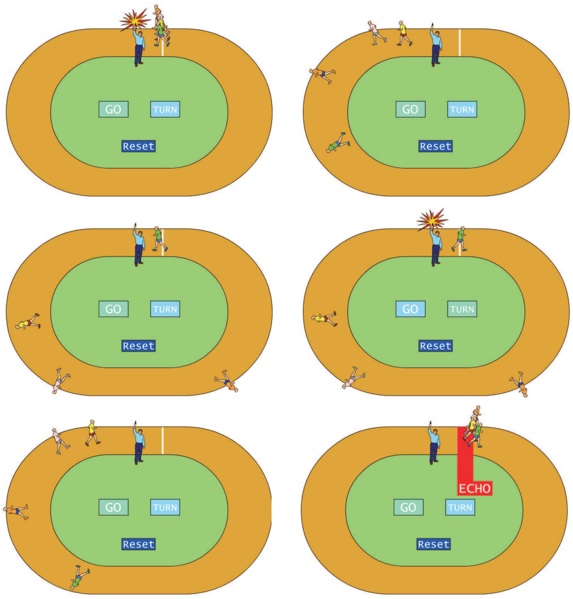

Figure 2.4: Runners on a track as an analogy for the photon echo. The runners represent oscillators, with their speeds the resonance frequencies, and the gun shot a resonant pulse. The first pulse creates a coherent superposition between the ground and excited state. During the ensuing delay, the atomic superpositions dephase from one another due to their different frequencies. A second conjugate pulse causes the oscillators to reverse their evolution, resulting in a rephasing of the coherence the same delay τ later, the photon echo. This interactive animation can be found on the Cundiff group website at http://jilawww.colorado.edu/˜cundiffs/Research-SemiCoherence.html, and is an echo (pardon the pun) of the front cover artwork of the November 1953 edition of *Physics Today*. [Created by J. Fall and V. Lorenz, JILA.]

broadened transition, the decay time of the TFWM signal is half the dephasing time, $T_2/2$, while for a static inhomogeneously broadened transition it is $T_2/4$. This difference of a factor of 2 between the homogeneous and inhomogeneous case can be understood based on the real-time signals. In the homogeneous case the peak of the real-time signal, the free polarization decay, occurs at $t = t_2$, while in the inhomogeneous case the peak of the real-time signal, the photon echo, occurs at $t = t_2 + (t_2 - t_1)$. When these signals are integrated over time, this difference in peak location results in the inhomogeneous response decaying twice as fast.

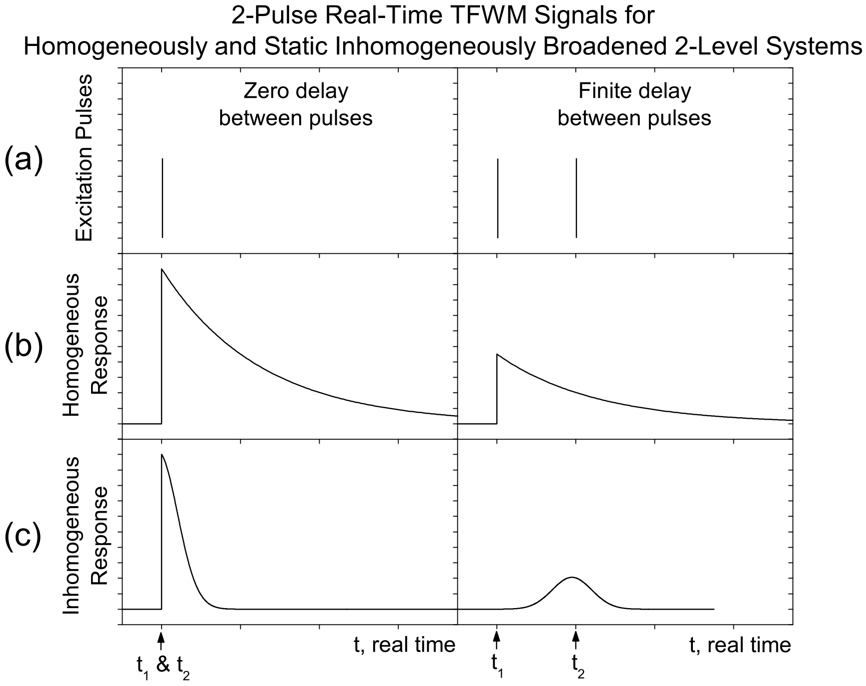

Figure 2.5: Calculated 2-pulse real-time TFWM signals for (a) two-pulse excitation in the case of a (b) homogeneously broadened and (c) static inhomogeneously broadened 2-level system. The two cases of zero delay between pulses and finite delay are shown.

In both cases the decay rate is then doubled because we are detecting the field squared, or the intensity. The time-integrated inhomogeneously broadened system response exhibits a peak at approximately $\delta\omega^{-1}$. This behavior is a result of the increasing area of the real-time signal at short times, shown in Fig. 2.7. There is only "half" a photon echo at zero delay due to causality. With increasing delay the "full" photon echo begins to develop, resulting in an initial increase of the time-integrated signal.

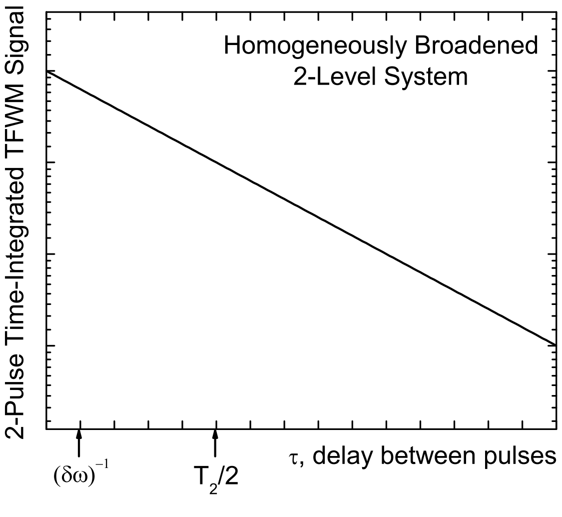

Figure 2.6: Calculated 2-pulse time-integrated TFWM signal for a homogeneously broadened system (natural log scale).

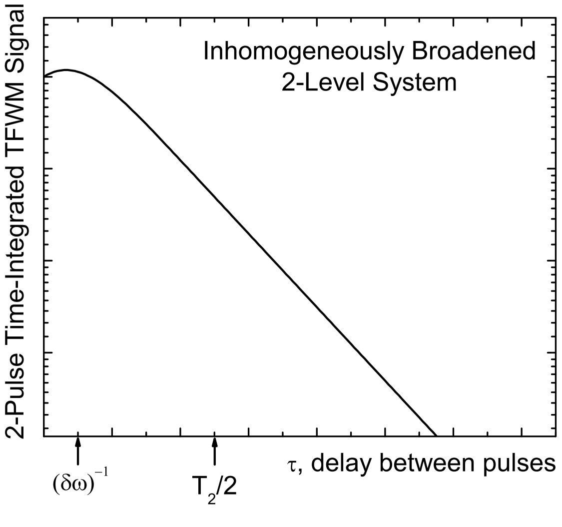

Figure 2.7: Calculated 2-pulse time-integrated TFWM signal for a static inhomogeneously broadened system (natural log scale).

2.4 The Markov Approximation

The above treatments of homogeneously and inhomogeneously broadened systems contain some important assumptions about the microscopic timescales of correlations. In particular, the treatment of the homogeneously broadened system above only accounts for exponential dephasing of the coherence, corresponding to a Lorentzian lineshape. In reality, no lineshape is perfectly Lorentzian. The finite duration of collisions results in deviations from Lorentzian behavior both at line center and in the wings of the absorption lineshapes [15]. This translates to non-exponential dephasing in time-domain experiments.

In this section the phenomenological approach used above is shown to be equivalent to making the Markov approximation for the dephasing process. In physics literature, Markovian evolution refers to time evolution determined solely by the instantaneous state of the system. Note this is not the same as the mathematical definition of a Markovian process, in which the time evolution is dependent on the previous state (the precise definition is provided in the next section). In this limit dephasing collisions are considered to occur infinitely fast, that is, the correlation time of the atomic superpositions is very short compared with the time scales of the nuclear dynamics. If we consider the optically-induced coherent superposition between ground and excited state as a function of time, the Markovian limit assumes collisions result in sudden phase jumps (see Fig. 2.8). In this section the time-domain response will be derived for a two-level system using the density matrix formalism including finite frequency fluctuations in the Markov approximation (also known as the impact approximation) [13]. It will be shown that linear frequency fluctuations result in dephasing of the coherence, and that the Markov approximation results in exponential dephasing. In the next section this treatment will be extended to non-Markovian dephasing.

To calculate the optical response including the finite duration of collisions the random frequency fluctuations at short times must be taken into account. To do so we add a time-dependent fluctuation to the excited state frequency. We start with the equation of motion from Eq. 2.9:

$$\dot{\rho}^{(q)}_{nm} = -(i\omega_{nm} + \gamma_{nm})\rho^{(q)}_{nm} - \frac{i}{\hbar}[-\hat{\mu} \cdot \mathbf{E}(t), \hat{\rho}^{(q-1)}]_{nm}.$$

We add a term to represent frequency fluctuations $\delta\omega(t)$:

$$\dot{\rho}^{(q)}_{nm} = -(i\omega_{nm} + i\delta\omega_{nm}(t) + \gamma_{nm})\rho^{(q)}_{nm} - \frac{i}{\hbar}[-\hat{\mu} \cdot \mathbf{E}(t), \hat{\rho}^{(q-1)}]_{nm}. \tag{2.23}$$

Now solving this equation we find

$$\begin{aligned} \rho^{(q)}_{nm}(t) &= -\frac{i}{\hbar}\int_{-\infty}^{t} dt' \mathrm{e}^{(i\omega_{nm}+\gamma_{nm})(t'-t)}[-\hat{\mu} \cdot \mathbf{E}(t'), \hat{\rho}^{(q-1)}]_{nm} \qquad (2.24)\\ &\quad \times \exp\Big[i\Big(\int_0^{t'} \delta\omega_{nm}(t'')dt'' - \int_0^{t} \delta\omega_{nm}(t')dt'\Big)\Big]. \end{aligned}$$

We now apply the ensemble average, which only affects the random variations in $\delta\omega(t)$:

$$\begin{aligned} \rho^{(q)}_{nm}(t) &= -\frac{i}{\hbar}\int_{-\infty}^{t} dt' \mathrm{e}^{(i\omega_{nm}+\gamma_{nm})(t'-t)}[-\hat{\mu} \cdot \mathbf{E}(t'), \hat{\rho}^{(q-1)}]_{nm} \qquad (2.25)\\ &\quad \times \langle \exp\Big[i\Big(\int_0^{t'} \delta\omega_{nm}(t'')dt'' - \int_0^{t} \delta\omega_{nm}(t')dt'\Big)\Big]\rangle. \end{aligned}$$

To solve we approximate the ensemble average of the product of exponentials to be the product of the ensemble averages and Taylor expand the exponentials. We consider only one of the $\delta\omega$ terms as the same treatment applies to both:

$$\begin{aligned} \langle \exp[-i\int_0^t \delta\omega(t')dt']\rangle &= 1 + i\int_0^t dt' \langle \delta\omega(t')\rangle \qquad (2.26)\\ &-\frac{1}{2}\int_0^t dt' \int_0^t dt'' \langle \delta\omega(t')\delta\omega(t'')\rangle + \cdots\\ &+\frac{(-i)^{2n}}{(2n)!}\int_0^t dt_1 \ldots \int_0^t dt_{2n} \langle \delta\omega(t_1)\ldots\delta\omega(t_{2n})\rangle + \cdots . \end{aligned}$$

Now we note that the fluctuations $\delta\omega(t)$ have zero mean (the random fluctuations are as often positive as negative), so terms odd in $\delta\omega(t)$ are zero. Then if we consider the first even term, the integrand, $\langle \delta\omega(t')\delta\omega(t'')\rangle$, is the two time correlation function of frequency fluctuations and ultimately will be used to determine the remaining terms. Thus it plays an important role in the theory and in the interpretation of experiment. At this point we must decide what form it shall take. To reproduce the results for a homogeneously broadened system above, we now take the Markov approximation.

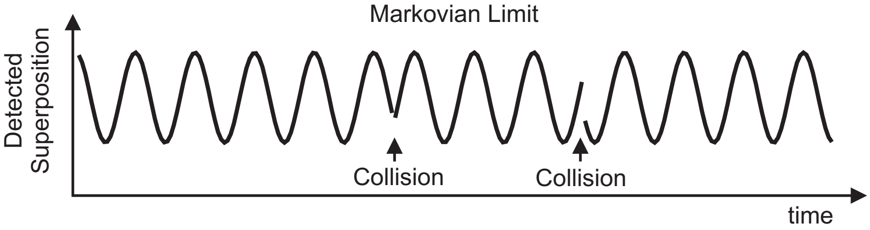

Figure 2.8: Superpositions in the Markovian limit. Collisions result in phase jumps.

The Markov approximation assumes that variations in ω are rapid compared to other changes such as population decay rates and dephasing rates such that the fluctuation at one instant in time can be considered completely uncorrelated with that of any different time. Thus we take the correlation function to be a delta function with an overall constant representative of the amplitude of the fluctuation:

$$\langle \delta\omega(t)\delta\omega(t')\rangle = 2\gamma_{ph}\delta(t-t').$$

The constant γ_{ph} can be set phenomenologically according to experimentally determined linewidths. The first even term of the expansion then is

$$\frac{1}{2}\int_0^t dt' \int_0^t dt'' \langle \delta\omega(t')\delta\omega(t'')\rangle = -\gamma_{ph}t. \tag{2.27}$$

We now assume that the fluctuations obey Gaussian statistics, that is, that they have a normal distribution. This assumption is reasonable if the fluctuations are made up of many small, random contributions with a finite mean and variance, qualities which satisfy the requirements of the central limit theorem. Making this approximation the higher order terms are simply factors of the two-time correlation function, resulting in a factor of $(2n)!/2^n$, equaling the number of permutations of $2n$ terms into n pairs. To restrict the permutations to distinguishable products, we divide by $n!$, resulting in the $2n$th term,

$$\begin{aligned}
&\frac{(-i)^{2n}}{(2n)!}\int_0^t dt_1 \ldots \int_0^t dt_{2n}\langle\delta\omega(t_1)\ldots\delta\omega(t_{2n})\rangle \\
&\quad= \frac{(-1)^n}{(2n)!}(2\gamma_{ph})^n\frac{(2n)!}{2^n n!}\int_0^t dt_1 \ldots \int_0^t dt_{2n}\delta(t_1-t_2)\ldots\delta(t_{2n-1}-t_{2n}) \\
&\quad= \frac{(-\gamma_{ph}t)^n}{n!}.
\end{aligned} \tag{2.28}$$

Using this result we then find a simple form for the expansion:

$$\langle\exp\big[-i\int_0^t \delta\omega(t')dt'\big]\rangle = \sum_{n=0}^{\infty}\frac{(-\gamma_{ph}t)^n}{n!} = \exp(-\gamma_{ph}t). \tag{2.29}$$

Inserting this result back into the density matrix element for both fluctuation terms we find the solution for the equation of motion:

$$\rho_{nm}^{(q)}(t) = -\frac{i}{\hbar}\int_{-\infty}^t dt' e^{(i\omega_{nm}+\gamma_{nm}+2\gamma_{ph})(t'-t)}[-\hat{\mu}\cdot\mathbf{E}(t'),\hat{\rho}^{(q-1)}]_{nm}. \tag{2.30}$$

Thus fluctuations with Markovian statistics result in exponential decay of the coherence. This equation is just that formed using phenomenological dephasing terms for a homogeneously broadened system, with the population and dephasing rates separated into $\gamma_{nm} - 2\gamma_{ph}$, $\gamma_{nm} = 0, n \neq m$. This approximation is not valid when the experiment probes timescales in which fluctuations do not occur instantaneously nor are obscured by fast dephasing dynamics. This brings us to the theory used to treat nonlinear optical interactions in the non-Markovian limit.

2.5 Non-Markovian Theory

The Markov approximation only holds for the limit in which either the experiment is insensitive to the retention of phase memory during collisions or the fluctuations are fast compared with the dephasing dynamics. With ultrashort pulses we are capable of resolving the response of a system on the timescale of collisions, and in a dense atomic vapor the dephasing time is longer than the collision duration, meaning the signal will no longer exhibit purely exponential dephasing. Modeling non-Markovian dynamics theoretically ultimately comes down to making a choice for the form of the fluctuations $\delta\omega$ and thus the form of the two-time correlation function of frequency fluctuations. To account for phase memory during collisions it is common to invoke the mathematical definition of a Markov process. In particular, according to the mathematical definition a stochastic process $x(t)$ is Markovian if its future probabilities $P(x(t_n))$ for every n are determined by the most recent states:

$$P(x(t_n) \leq x_n | x(t_{n-1}), \ldots, x(t_1)) = P(x(t_n) \leq x_n | x(t_{n-1})), \tag{2.31}$$

with $t_1 < t_2 ... < t_n$ [28]. This equation can be read as "The probability of a system being less than or equal to a value x_n at time t_n given all previous states is equal to the probability given only the most recent state, $x(t_{n-1})$." Applying this to the frequency fluctuations allows the fluctuations to depend on their most recent form, improving the treatment of the short-time limit in which non-Markovian dynamics are important. Furthermore, in a theorem proven by Doob, any random process x that is both Markovian and follows Gaussian statistics (also known as an Ornstein-Uhlenbeck process [29]) has a correlation function $C_x(\tau)$ of the form

$$C_x(\tau) = \sigma_x^2 e^{-\tau/\tau_r}, \tag{2.32}$$

where τ_r is the relaxation time and σ_x the standard deviation of x [30]. Using this correlation function is a common way of accounting for phase memory in condensed phase systems, often referenced simply as a stochastic model or the Kubo model [15, 31, 32, 33]. Another way of achieving this result theoretically is to invoke the overdamped Brownian oscillator model in the high temperature limit [16].

Note that in much of the literature as well as in this thesis the word "non-Markovian" refers to the dephasing process, not the fluctuations themselves. This is an important distinction to make because as just shown the stochastic model actually makes the *Markov* approximation for the dephasing *mechanism.* Thus the word "non-Markovian" is a descriptor for the dynamics of the coherence, not the dynamics of collisions. The stochastic model does not explicitly account for the dipole-dipole interaction between atoms and thus is limited in the physical insight it can provide. However, because of its frequent use in more complex systems the well-defined signatures of non-Markovian dynamics in a dense atomic vapor provide an important opportunity to test this theoretical description of dephasing [23].

Although it is possible to derive the dynamics including non-Markovian dephasing with steps similar to the previous section in which we insert the time-dependent resonance frequency into the density matrix equations of motion, there is a parallel approach that does not require us to keep track of the detailed form of intermediate equations [15]. This approach derives the nonlinear response in Liouville space, which was originally developed by Zwanzig [34, 35, 36, 37]. A major benefit of this formalism is that it does not require us to carry unused wavevector combinations only to discard them later, as is done in the optical Bloch equations, in which all permutations of the wavevectors of the fields must be carried to third order, at which point only terms in the direction of interest are chosen. By using Liouville operators instead we are able to specify the perturbation sequences of interest and only derive response functions for those sequences. Here a summary of the most important steps is provided for a three-level system in order to facilitate the discussion of the modeling of experimental results. The equations will also be simplified to the solution for a two-level system for comparison with the above results.

We begin with the Hamiltonian for a perturbed system from Eq. 2.6:

$$H = H_0 + H_{int}, \tag{2.33}$$

where H_0 is the Hamiltonian for the material system in the absence of the radiation field and H_{int} represents the radiation-matter interaction and is given by

$$H_{int}(t) = E(\mathbf{r}, t)V, \tag{2.34}$$

where V is the dipole operator of the atom. The evolution of the system is represented by the density matrix equation of motion, which takes the form of the Liouville equation

$$\frac{d\rho}{dt} = -i[H_0, \rho] - i[H_{int}, \rho], \tag{2.35}$$

which becomes in Liouville-space notation,

$$\frac{d\rho}{dt} = -iL_0\rho - iL_{int}\rho. \tag{2.36}$$

In Liouville space we employ Liouville (tetradic) operators, whose action on an ordinary (dyadic) operator A is given by

$$L_0 A \equiv [H_0, A], \tag{2.37}$$

$$L_{int} A \equiv [H_{int}, A]. \tag{2.38}$$

To simplify the coming expressions we now set $\hbar = 1$ and define the Liouville dipole operator

$$\mathcal{V} A \equiv [V, A]. \tag{2.39}$$

We are interested in calculating the polarization $P(\mathbf{r}, t)$, which is given by the expectation value of the dipole operator V:

$$P(\mathbf{r}, t) \equiv \langle\langle V|\rho(t)\rangle\rangle, \tag{2.40}$$

where double-angle-bracket notation is used to denote an inner product of operators. For any two operators,

$$\langle\langle A|B\rangle\rangle \equiv \mathrm{Tr}(A^\dagger B). \tag{2.41}$$

We also define a Liouville-space matrix element by

$$\langle\langle A|L|B\rangle\rangle \equiv \mathrm{Tr}(A^\dagger L B). \tag{2.42}$$

The third-order polarization of interest is obtained by calculating $\rho(t)$ perturbatively to third order in L_{int}:

$$\rho(t) = U(t, -\infty)\rho(-\infty) \equiv \rho(0) + \rho^{(1)} + \rho^{(2)} \cdots, \tag{2.43}$$

where U is the time-evolution operator, which when expanded takes the form

$$\begin{aligned} U(t, -\infty) &= 1 - i \int_{-\infty}^{t} d\tau G(t-\tau) L_{int}(\tau) \qquad (2.44)\\ &+(-i)^2 \int_{-\infty}^{t} d\tau_1 \int_{-\infty}^{\tau_1} d\tau_2 G(t-\tau_1) L_{int}(\tau_1) G(\tau_1-\tau_2) L_{int}(\tau_2) + \cdots, \end{aligned}$$

where the Green function $G(\tau)$ is the formal solution of the Liouville equation in the absence of the electromagnetic field:

$$G(\tau) \equiv \exp(-iL_0\tau). \tag{2.45}$$

The third-order polarization, written in the time-domain, then is

$$\begin{aligned} P^{(3)}(\mathbf{r}, t) &= (-i)^3 \int_0^\infty dt_1 \int_0^{t_1} dt_2 \int_0^{t_2} dt_3 \qquad (2.46)\\ &\times \langle\langle V|G(t_3) L_{int}(t_1-t_3) G(t_2-t_3) L_{int}(t_1-t_2) G(t_1-t_2) L_{int}(0)|\rho(-\infty)\rangle\rangle. \end{aligned}$$

Reading this equation from right to left reveals the evolution of the system: The system starts at $t = -\infty$ in state $\rho(-\infty)$. The interactions with the field are represented by $L_{int}(\tau)$ and occur at times $0 \leq (t_1 - t_2) \leq (t_1 - t_3) \leq t_1$. Each interaction is followed by an evolution in time according to $G(\tau)$ for the intervals

$(t_1 - t_2)$, $(t_2 - t_3)$ and t_3. At time t_1 the polarization is calculated. This equation for the polarization is the time-ordered expansion of the evolution operator. To simplify the following steps we make a transformation of time variables and define

$$\begin{aligned}
\tau_1 &= t_1, \\
\tau_2 &= t_1 - t_3, \\
\tau_3 &= t_1 - t_2, \qquad (2.47)
\end{aligned}$$

These new time variables allow us to order the interactions $0 \leq \tau_3 \leq \tau_2 \leq \tau_1$. Equation 2.46 then becomes

$$\begin{aligned}
P^{(3)}(\mathbf{r}, t) = (-i)^3 \int_0^\infty d\tau_1 \int_0^{\tau_1} d\tau_2 \int_0^{\tau_2} d\tau_3 \qquad (2.48) \\
\times \langle\langle V(\tau_1)|G(\tau_1 - \tau_2)L_{int}(\tau_2)G(\tau_2 - \tau_3)L_{int}(\tau_3)G(\tau_3)L_{int}(0)|\rho(-\infty)\rangle\rangle.
\end{aligned}$$

By inserting the incident fields and the appropriate dipole operators we have an explicit expression for the polarization. We write the field in the form

$$\mathbf{E}(\mathbf{r}, t) = [E_1 \exp(-i\omega_1 t) + E_2 \exp(-i\omega_2 t) + E_3 \exp(-i\omega_3 t)] + \text{c.c.}. \qquad (2.49)$$

Here E_j is the amplitude of the jth field and ω_j is its frequency. The total polarization is the sum over all possible permutations of wavevector and frequency. We choose to detect the polarization emitted in the direction $\mathbf{k}_4 = -\mathbf{k}_1 + \mathbf{k}_2 + \mathbf{k}_3$ with frequency $\omega_4 = -\omega_1 + \omega_2 + \omega_3$. In this case we need only consider the polarization

$$\begin{aligned}
P^{(3)}(\mathbf{k}_4, t) &= (-i)^3 \sum_{m,n,q=1,2,3} \int_0^\infty d\tau_1 \int_0^\infty d\tau_2 \int_0^\infty d\tau_3 \\
&\quad \times \exp\big[-i\omega_q(\tau_1) + i\omega_n(\tau_1 - \tau_3) + i\omega_m(\tau_1 - \tau_2)\big] \\
&\quad \times E_m(\tau_3)E_n(\tau_2)E_q(\tau_1)R(\tau_1, \tau_2, \tau_3, \tau_4), \qquad (2.50)
\end{aligned}$$

where the summation is over all $3! = 6$ permutations of the fields and we have separated the fields from the material response by defining the nonlinear response function, $R(\tau_1, \tau_2, \tau_3, \tau_4)$, which contains all relevant microscopic information:

$$R(\tau_1, \tau_2, \tau_3, \tau_4) \equiv \tag{2.51}$$
$$\langle\langle V(\tau_1)|G(\tau_1 - \tau_2)\mathcal{V}(\tau_2)G(\tau_2 - \tau_3)\mathcal{V}(\tau_3)G(\tau_3 - \tau_4)\mathcal{V}(\tau_4)|\rho(-\infty)\rangle\rangle.$$

The above equation for the polarization can serve as a general formal expression for any four-wave mixing process. Now if we make the assumption of delta-function pulses $E_i(\tau) = E_i\delta(\tau - \tau_i)$; $i = 1, 2, 3$; this expression simplifies to

$$P^{(3)}(\mathbf{k}_4, t) = \tag{2.52}$$
$$E_1E_2E_3 \exp[-i\omega_q(\tau_1) + i\omega_n(\tau_1 - \tau_3) + i\omega_m(\tau_1 - \tau_2)]R(\tau_1, \tau_2, \tau_3, \tau_4)$$

This results in a real-time signal given by

$$S(\mathbf{k}_4, t) = |E_1E_2E_3|^2|R(\tau_1, \tau_2, \tau_3, \tau_4)|^2. \tag{2.53}$$

To this point the derivation has not required that we specify the level structure of the material system, but we have reached the stage at which we must specify the Hamiltonian of the system. We choose the most general level structure in which four different, arbitrary levels a, b, c, d are sequentially excited through the four-wave mixing process. This is the most general case because a third-order experiment can at most couple four levels; thus, four levels are sufficient. We now specify the Hamiltonian H for this system interacting with a bath:

$$H = H_0 + H_{int} + H_B \tag{2.54}$$

with

$$H_0 = \sum_{\nu=a,b,c,d} |\nu\rangle\big[\epsilon_\nu - \frac{i}{2}\gamma_\nu\big]\langle\nu| \tag{2.55}$$

and

$$H_B = \sum_{\nu=a,b,c,d} |\nu\rangle H_B^\nu(Q_B)\langle\nu|. \tag{2.56}$$

Here ϵ_ν is the energy and γ_ν the inverse lifetime of the level ν. $H_B^\nu(Q_B)$ is an adiabatic Hamiltonian describing the bath degrees of freedom Q_B interacting with the system in the state ν. We assume the atoms are initially in the ground state, making $|\rho(-\infty)\rangle\rangle = \sum_a P(a)|a\rangle\rangle$, where $P(a)$ is the thermal equilibrium ground state population in the absence of a radiation field. To calculate the response function we write the matrix elements of the Green function Eq. 2.45:

$$\langle\langle\nu'\lambda'|G(t)|\nu\lambda\rangle\rangle = \delta_{\nu\nu'}\delta_{\lambda\lambda'}\exp\bigl[-i\omega_{\nu\lambda}t - \frac{1}{2}(\gamma_\nu - \gamma_\lambda)t\bigr], \tag{2.57}$$

with $\nu, \lambda = a, b, c, d$ and $\omega_{\nu\lambda} \equiv \epsilon_\nu - \epsilon_\lambda$. Now the bath Hamiltonian is combined with the Hamiltonian representing the interaction with the fields to simplify the following expressions. This choice amounts to including frequency fluctuations $\delta\omega$ by modifying the electronic dipole operator. Note modification could alternatively be made to the Green function by adding a $\delta\omega$ to H_0, where it can be seen more directly to be a fluctuation of the resonance frequency [31]; the current approach results in simpler expressions later on. The modified dipole operator then takes the form

$$V(\tau) = \sum_{\nu,\lambda=a,b,c,d;\nu\neq\lambda} \mu_{\nu\lambda}\exp_+\left(-i\int_0^\tau d\tau_1 U_{\nu\lambda}(\tau_1)\right)|\nu\rangle\langle\lambda|. \tag{2.58}$$

Here $\exp_+$ is the positive-time-ordered exponential and $U_{\nu\lambda} \equiv H_\nu - H_\lambda$. The semiclassical approximation is made by replacing $\exp_+$ by an ordinary exponential and treating $U_{\nu\lambda}(\tau)$ as an ordinary function of time (not an operator) denoted $\delta\omega_{\nu\lambda}(\tau)$. Then

$$V(\tau) = \sum_{\nu,\lambda=a,b,c,d;\nu\neq\lambda} \mu_{\nu\lambda}\exp\left(-i\int_0^\tau d\tau_1 \delta\omega_{\nu\lambda}(\tau_1)\right)|\nu\rangle\langle\lambda|. \tag{2.59}$$

Given the matrix elements of the Green function Eq. 2.57 and the form of the dipole operator Eq. 2.59 we can now calculate the response functions. From the definition of the Liouville dipole operator Eq. 2.39, we can write the expression for the response function in terms of the dyadic dipole operator V:

$$R(\tau_1, \tau_2, \tau_3, \tau_4) = \tag{2.60}$$
$$\langle\langle V(\tau_1)|G(\tau_1 - \tau_2)[V(\tau_2), G(\tau_2 - \tau_3)[V(\tau_3), G(\tau_3)[V(\tau_4), |\rho(-\infty)\rangle\rangle]]]$$

All of the response functions will take the same form, namely

$$R(\tau_1, \tau_2, \tau_3, \tau_4) = \prod_{\nu\lambda} \langle\langle G\rangle\rangle F(\tau_1, \tau_2, \tau_3, \tau_4), \tag{2.61}$$

where the product is over the contributing matrix elements of the Green function and F is the four-point correlation function of the dipole operator, defined for the excitation of a four-level system as

$$F(\tau_1, \tau_2, \tau_3, \tau_4) \equiv \langle V_{ab}(\tau_1)V_{bc}(\tau_2)V_{cd}(\tau_3)V_{da}(\tau_4)\rho(-\infty)\rangle. \tag{2.62}$$

Using the four-point correlation function allows us to use the same four dipole operators for every response function. A minus sign accrues for every time a density operator is acted on from the right, as evident from the definition $[V, A] \equiv VA - AV$.

The real system in which we are interested for the experiments in this thesis can be modeled as a three-level system with two excited states b and c radiatively coupled to a ground state a but not radiatively coupled to one another. A given four-point correlation function can only represent variations on four dipole operators, with each operator acting once. This means that to model a three-level system we cannot use just one four-point correlation function. For example, it might be thought that the appropriate four-point correlation function for a three-level system with levels a, b, c is $\langle V_{ab}V_{ba}V_{ac}V_{ca}\rangle$. However, this function does not include two-level physics because each operator must act once, meaning sequences involving only a and b or a and c are not covered. Another way of stating this is that the formalism using four-point correlation functions assumes that the incident pulses are narrowband and only excite one transition at a time. In the experiments of this thesis, the pulses are broadband and simultaneously excite two excited states. This theoretical situation arises from our assumption of plane-wave fields as well as delta-function durations, a strange but useful fiction. Thus to model a three-level system we must use two 2-level four-point correlation functions as well as the one given in the example. Thus we need the following correlation functions:

$$^2F(\tau_1, \tau_2, \tau_3, \tau_4) \equiv \langle V_{am}(\tau_1)V_{ma}(\tau_2)V_{am}(\tau_3)V_{ma}(\tau_4)\rho(-\infty)\rangle, \tag{2.63}$$

$$^3F(\tau_1, \tau_2, \tau_3, \tau_4) \equiv \langle V_{ab}(\tau_1)V_{ba}(\tau_2)V_{ac}(\tau_3)V_{ca}(\tau_4)\rho(-\infty)\rangle, \tag{2.64}$$

where the superscripts 2 and 3 represent 2- and 3-level physics, respectively, and $m = b, c$.

To choose the correct time sequences we must know which sequences of dipole operators will contribute to a response in the chosen direction, $\mathbf{k}_4 = -\mathbf{k}_1 + \mathbf{k}_2 + \mathbf{k}_3$. These sequences, called pathways, can be represented quite nicely using diagrams, useful particularly for higher-order, multi-level response. Appendix B.1 gives an introduction to the use of these so-called double-sided Feynman diagrams. The pathways contributing to the material response are shown in Fig. 2.9. The first (last) two diagrams correspond to two- (three-) level physics. For two-level physics there will be two distinct pathways (for each of b and c) contributing to the response for the time ordering $(-\mathbf{k}_1, \mathbf{k}_2, \mathbf{k}_3)$, corresponding to diagrams labeled $^2R_2^m$ and $^2R_3^m$ and the perturbation sequences (reading right to left) (ma, mm, am, aa) and (ma, aa, am, aa), $m = b, c$. We can write the response functions in terms of the four-point correlation function of the dipole operator ^2F defined above. For three-level physics there also will be two pathways contributing to the response for the time ordering $(-\mathbf{k}_1, \mathbf{k}_2, \mathbf{k}_3)$, labeled $^3R_2^n$ and $^3R_3^n$, corresponding to the perturbation sequences (reading right to left) (na, nm, am, aa), (na, aa, am, aa). We can write these response functions in terms of the four-point correlation function of the dipole operator ${}^3F$ defined above. The R labels for each response function have been written according to the pathways they represent. The first superscript represents 2- or 3-level physics. For 2-level physics, the subscript represents an excited-state (2) or ground-state (3) population to second order. For 3-level physics, the subscript represents a Raman coherence (2) or ground state population (3) to second order. The second superscript is the final excited state that forms a coherence with the ground state at third order. The response functions then are

$$\begin{aligned}
&(ma, mm, am, aa) \quad {}^2R_2^m(\tau_1,\tau_2,\tau_3) = {}^2F(0,\tau_2,\tau_1,\tau_3)\mathrm{e}^{-i\omega_{ma}(\tau_1-\tau_2-\tau_3)},\\
&(ma, aa, am, aa) \quad {}^2R_3^m(\tau_1,\tau_2,\tau_3) = {}^2F(0,\tau_3,\tau_1,\tau_2)\mathrm{e}^{-i\omega_{ma}(\tau_1-\tau_2-\tau_3)},\\
&(na, nm, am, aa) \quad {}^3R_2^n(\tau_1,\tau_2,\tau_3) = \\
&\qquad\qquad {}^3F(0,\tau_2,\tau_1,\tau_3)\mathrm{e}^{-i\omega_{na}(\tau_1-\tau_2)-i\omega_{nm}(\tau_2-\tau_3)-i\omega_{ma}(-\tau_3)},\\
&(na, aa, am, aa) \quad {}^3R_3^n(\tau_1,\tau_2,\tau_3) = {}^3F(0,\tau_3,\tau_1,\tau_2)\mathrm{e}^{-i\omega_{na}(\tau_1-\tau_2)-i\omega_{ma}(-\tau_3)},
\end{aligned} \tag{2.65}$$

where the exponentials are the matrix elements of the Green function, calculated based on Eq. 2.57 for each duration and perturbation sequence; we assume the population decay rates are slow compared to the dephasing rates and can be neglected. The total contribution from the Green functions for each perturbation sequence $\nu_1\lambda_1, \nu_2\lambda_2, \nu_3\lambda_3$ can be calculated from the general function $G_{\nu_3\lambda_3}(\tau_1 - \tau_2)G_{\nu_2\lambda_2}(\tau_2-\tau_3)G_{\nu_1\lambda_1}(\tau_3)$, where $G_{\nu\lambda}$ is the Green function matrix element for ν, λ and the time arguments remain as written (no substitutions necessary). For the time ordering $(\mathbf{k}_2, -\mathbf{k}_1, \mathbf{k}_3)$ there will also be four response functions; a parallel derivation for these is provided in App. B.2.

Using the four-point correlation function reduces the calculation of the response functions of all contributing pathways to finding the forms of (in our case) two four-point correlation functions, those for two-level and three-level physics. In App. B.2 we derive the solution for the most general form of the correlation function ${}^4F$, which assumes the excitation of four different arbitrary levels a, b, c, d (in

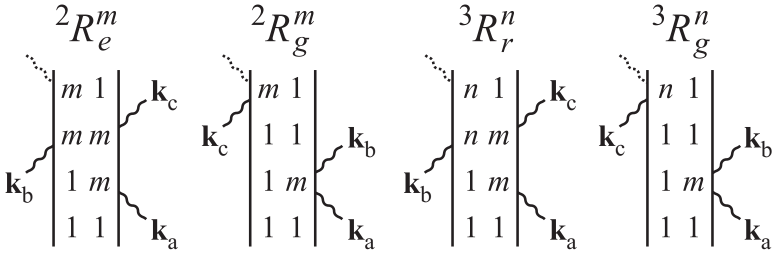

Figure 2.9: Double-sided Feynman diagrams representing the relevant pathways for 3-pulse TFWM in a 3-level system for signal in direction $-\mathbf{k}_1 + \mathbf{k}_2 + \mathbf{k}_3$ and time ordering $(-\mathbf{k}_1, \mathbf{k}_2, \mathbf{k}_3)$, with $m, n = b, c$; $m \neq n$. The diagrams for all time orderings are shown in App. B.

that order) following the derivation of Mukamel [15]. The four-point correlation function based on the definition in Eq. 2.59 for this case has the form

$$\begin{aligned} {}^4F(\tau_1, \tau_2, \tau_3, \tau_4) &= \mu_{ab}\mu_{bc}\mu_{cd}\mu_{da}\langle \exp\Big\{ i\Big[\int_0^{\tau_1} d\tau \delta\omega_{ab}(\tau) + \int_0^{\tau_2} d\tau \delta\omega_{bc}(\tau) \\ &\quad + \int_0^{\tau_3} d\tau \delta\omega_{cd}(\tau) + \int_0^{\tau_4} d\tau \delta\omega_{da}(\tau) \Big] \Big\} \rangle \end{aligned} \tag{2.66}$$

In order to solve this expression without simply truncating its Taylor expansion to second order we apply the cumulant expansion [38, 39, 40]. This is carried out in detail in App. B.2. To overview the steps taken, first we make the ansatz that F has an exponential form: $F = \exp(\mathcal{F})$. We then expand $\mathcal{F}$ in orders of the fluctuation $\delta\omega$, and substitute this expansion back into the ansatz. Collecting terms of like order of $\delta\omega$ and comparing with the original Taylor expansion of F allows us to solve for the orders of $\mathcal{F}$ in terms of the orders of F. We then insert these solutions into the ansatz and truncate at $\mathcal{F}^{(2)}$. Thus instead of just neglecting higher order correlations starting with Eq. 2.66, this method allows us to partially resum the perturbation series for F. The result for the 4-level four-point correlation function is

$$
\begin{aligned}
{}^{4}F(\tau_1,\tau_2,\tau_3,\tau_4) &= \mu_{ab}\mu_{bc}\mu_{cd}\mu_{da} \qquad (2.67)\\
&\times \exp\Big\{-\frac{1}{2}\big[g_{ab}(\tau_1-\tau_2)+g_{ab}(\tau_1-\tau_4)-g_{ab}(\tau_2-\tau_4)\\
&-g_{ac}(\tau_1-\tau_2)-g_{ac}(\tau_3-\tau_4)+g_{ac}(\tau_1-\tau_3)+g_{ac}(\tau_2-\tau_4)\\
&+g_{ad}(\tau_3-\tau_4)+g_{ad}(\tau_1-\tau_4)-g_{ad}(\tau_1-\tau_3)\\
&+g_{bc}(\tau_1-\tau_2)+g_{bc}(\tau_2-\tau_3)-g_{bc}(\tau_1-\tau_3)\\
&+g_{bd}(\tau_2-\tau_3)-g_{bd}(\tau_1-\tau_4)+g_{bd}(\tau_2-\tau_4)\\
&+g_{cd}(\tau_2-\tau_3)+g_{cd}(\tau_3-\tau_4)-g_{cd}(\tau_2-\tau_4)\big]\Big\},
\end{aligned}
$$

where we have defined the line shape function

$$g_{\alpha\beta}(\tau) \equiv \int_0^{\tau} d\tau_1 \int_0^{\tau_1} d\tau_2 \langle \delta\omega_{\alpha\beta}(\tau_2)\delta\omega_{\alpha\beta}(0)\rangle.$$

Using this expression we can determine the 2-level physics correlation function by substituting $c \to a$:

$$
\begin{aligned}
{}^{2}F(\tau_1,\tau_2,\tau_3,\tau_4) &= \mu_{am}^4 \exp\big[-g_{am}(\tau_1-\tau_2)+g_{am}(\tau_1-\tau_3) \qquad (2.68)\\
&-g_{am}(\tau_2-\tau_3)-g_{am}(\tau_1-\tau_4)+g_{am}(\tau_2-\tau_4)-g_{am}(\tau_3-\tau_4)\big],
\end{aligned}
$$

where m represents the excited states b, c. For the four-point correlation function representing three-level physics we make the additional substitution $d \to b$ to find

$$
\begin{aligned}
{}^{3}F(\tau_1,\tau_2,\tau_3,\tau_4) &= \mu_{am}^2\mu_{an}^2 \exp\Big\{-\frac{1}{2}\big[\,2g_{am}(\tau_1-\tau_2)+2g_{an}(\tau_3-\tau_4) \qquad (2.69)\\
&-g_{am}(\tau_1-\tau_3)+g_{am}(\tau_1-\tau_4)+g_{am}(\tau_2-\tau_3)-g_{am}(\tau_2-\tau_4)\\
&-g_{an}(\tau_1-\tau_3)+g_{an}(\tau_1-\tau_4)+g_{an}(\tau_2-\tau_3)-g_{an}(\tau_2-\tau_4)\\
&+g_{mn}(\tau_1-\tau_3)-g_{mn}(\tau_1-\tau_4)-g_{mn}(\tau_2-\tau_3)+g_{mn}(\tau_2-\tau_4)\big]\Big\}.
\end{aligned}
$$

Determining the response functions for a three-level system is now reduced to inserting the time sequences of Eq. 2.65 into the above equations for each pathway. Doing so gives us the final results for the third-order response functions for a three-level system in direction $-\mathbf{k}_1+\mathbf{k}_2+\mathbf{k}_3$ and time ordering $(-\mathbf{k}_1,\mathbf{k}_2,\mathbf{k}_3)$ (equations for the other time ordering are in App. B.3)[3] :

$$\begin{aligned}
{}^2R_2^m(\tau_1,\tau_2,\tau_3) &= \mu_{am}^4 \mathrm{e}^{-i\omega_{ma}(\tau_1-\tau_2-\tau_3)} \\
&\times \exp\Big\{\frac{1}{2}\big[-g_{am}(-\tau_2)+g_{am}(-\tau_1)-g_{am}(\tau_2-\tau_1) \\
&-g_{am}(-\tau_3)+g_{am}(\tau_2-\tau_3)-g_{am}(\tau_1-\tau_3)\big]\Big\}, \\
{}^2R_3^m(\tau_1,\tau_2,\tau_3) &= \mu_{am}^4 \mathrm{e}^{-i\omega_{ma}(\tau_1-\tau_2-\tau_3)} \\
&\times \exp\Big\{\frac{1}{2}\big[-g_{am}(-\tau_3)+g_{am}(-\tau_1)-g_{am}(\tau_3-\tau_1) \\
&-g_{am}(-\tau_2)+g_{am}(\tau_3-\tau_2)-g_{am}(\tau_1-\tau_2)\big]\Big\}, \\
{}^3R_2^n(\tau_1,\tau_2,\tau_3) &= \mu_{am}^2\mu_{an}^2 \mathrm{e}^{-i\omega_{na}(\tau_1-\tau_2)-i\omega_{nm}(\tau_2-\tau_3)-i\omega_{ma}(-\tau_3)} \\
&\times \exp\Big\{-\frac{1}{2}\big[\,2g_{am}(-\tau_2)+2g_{an}(\tau_1-\tau_3) \\
&-g_{am}(-\tau_1)+g_{am}(-\tau_3)+g_{am}(\tau_2-\tau_1)-g_{am}(\tau_2-\tau_3) \\
&-g_{an}(-\tau_1)+g_{an}(-\tau_3)+g_{an}(\tau_2-\tau_1)-g_{an}(\tau_2-\tau_3) \\
&+g_{nm}(-\tau_1)-g_{nm}(-\tau_3)-g_{nm}(\tau_2-\tau_1)+g_{nm}(\tau_2-\tau_3)\big]\Big\}, \\
{}^3R_3^m(\tau_1,\tau_2,\tau_3) &= \mu_{am}^2\mu_{an}^2 \mathrm{e}^{-i\omega_{na}(\tau_1-\tau_2)-i\omega_{ma}(-\tau_3)} \\
&\times \exp\Big\{-\frac{1}{2}\big[\,2g_{an}(-\tau_3)+2g_{am}(\tau_1-\tau_2) \\
&-g_{am}(-\tau_1)+g_{am}(-\tau_2)+g_{am}(\tau_3-\tau_1)-g_{am}(\tau_3-\tau_2) \\
&-g_{an}(-\tau_1)+g_{an}(-\tau_2)+g_{an}(\tau_3-\tau_1)-g_{an}(\tau_3-\tau_2) \\
&+g_{nm}(-\tau_1)-g_{nm}(-\tau_2)-g_{nm}(\tau_3-\tau_1)+g_{nm}(\tau_3-\tau_2)\big]\Big\},
\end{aligned}$$

with $m,n=b,c$; $m\neq n$. The sum of the above response functions gives the polarization. Thus we have for the spectrally integrated polarization for time

---

[3] To convert the above equations to notation with times *between* pulses t_1, t_2 and t_3 (with t_1 the time of pulse 1, t_2 the delay between pulses 1 and 2 and t_3 the delay between pulses 2 and 3), use the conversion equations $\tau_1=t_1+t_2+t_3$, $\tau_2=t_1+t_2$ and $\tau_3=t_1$.

ordering $(-\mathbf{k}_1, \mathbf{k}_2, \mathbf{k}_3)$:

$$\begin{aligned} P_{SI}^{(3)}(t) = \big[& {}^2R_2^2(\tau_1,\tau_2,\tau_3) + {}^2R_2^3(\tau_1,\tau_2,\tau_3) + {}^2R_3^2(\tau_1,\tau_2,\tau_3) \\ & + {}^2R_3^3(\tau_1,\tau_2,\tau_3) + {}^3R_2^2(\tau_1,\tau_2,\tau_3) + {}^3R_2^3(\tau_1,\tau_2,\tau_3) \\ & + {}^3R_3^2(\tau_1,\tau_2,\tau_3) + {}^3R_3^3(\tau_1,\tau_2,\tau_3)\big]. \end{aligned} \tag{2.70}$$

The TFWM signal can in turn be calculated by performing an integral over the square of the polarization,

$$S = \int_{-\infty}^{\infty} |P^{(3)}(t)|^2 dt. \tag{2.71}$$

Now that we have the response functions in terms of the lineshape functions g the last step is to decide the form of the two-time correlation function of frequency fluctuations to find the form of g. To model a system with non-Markovian dephasing we use the stochastic model described at the beginning of this section. In particular, we assume the modulation of the i to j transition $\delta\omega_{ij}$ obeys the stochastic two-time correlation function of frequency fluctuations

$$\langle \delta\omega_{ij}(t_1)\delta\omega_{ij}(t_2)\rangle = \Delta_{ij}^2 \exp(-\Lambda_{ij}|t_2 - t_1|) \tag{2.72}$$

and

$$\langle \delta\omega_{ij}(t)\rangle = 0, \tag{2.73}$$

where Δ_{ij} corresponds to the root-mean-squared amplitude of the frequency fluctuations and Λ_{ij}^{-1} is their time scale. The angle brackets denote an ensemble average over the stochastic process. Figure 2.10 is a schematic of the stochastic correlation function. The stochastic model results in a line shape function given by

$$\begin{aligned} g_{ij}(t) &= \int_0^t d\tau_1 \int_0^{\tau_1} d\tau_2 \langle \delta\omega_{ij}(\tau_1 - \tau_2)\delta\omega_{ij}(0)\rangle \\ &= \frac{2\Delta_{ij}^2}{\Lambda_{ij}^2}\big[\exp(-\Lambda_{ij}t) + \Lambda_{ij}t - 1\big]. \end{aligned} \tag{2.74}$$

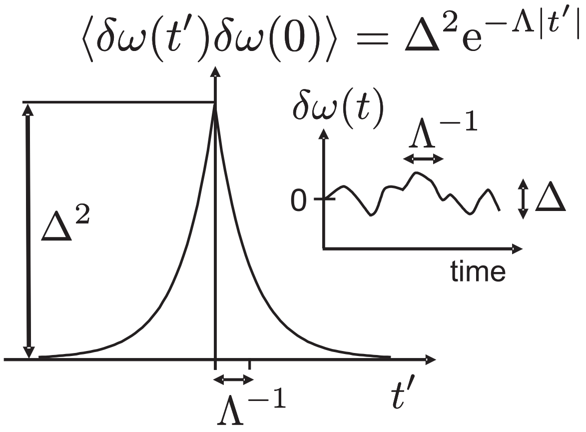

Figure 2.10: Schematic of stochastic correlation function.

In order to compare these results with the two-pulse derivations above, we reduce the equations to the two-pulse case by setting $\tau_1 = \tau_2$. The response functions for the two possible interaction pathways corresponding to 2- and 3-level physics then are

$$\begin{aligned}
{}^2R_2^m = {}^2R_3^m = \mu_{am}^4 \mathrm{e}^{-i\omega_{ma}(\tau_1 - 2\tau_2)} \exp\big[\, & 2g_{am}(-\tau_2) + g_{am}(-\tau_1) \\
& - g_{am}(\tau_2 - \tau_1) - g_{am}(\tau_1 - \tau_2)\big], \\
{}^3R_2^n = {}^3R_3^n = \mu_{am}^2\mu_{an}^2 \mathrm{e}^{-i\omega_{na}(\tau_1-\tau_2) - i\omega_{ma}(-\tau_2)} \exp\Big\{ & -\frac{1}{2}\big[3g_{am}(-\tau_2) + 2g_{an}(\tau_1 - \tau_2) \\
& + g_{am}(-\tau_1) - g_{am}(\tau_2 - \tau_1) - g_{an}(-\tau_1) + g_{an}(-\tau_2) + g_{an}(\tau_2 - \tau_1) \\
& + g_{mn}(-\tau_1) - g_{mn}(-\tau_2) - g_{mn}(\tau_2 - \tau_1)\big]\Big\}. \qquad (2.75)
\end{aligned}$$

The sum of the response functions gives the polarization in Eq. (2.71) that is then numerically integrated to obtain the TFWM signal. The results of this non-Markovian calculation for the case of a two-level system are plotted for the time-resolved and time-integrated cases in Figs. 2.11 and 2.12.

The 2-pulse results including non-Markovian dephasing look very similar to the static inhomogeneous broadening case derived earlier. Indeed, one way to think about this result is in terms of the system being "inhomogeneously broadened" at short times and "homogeneously broadened" at long times. These two limits correspond to timescales in which fast modulations of the transition energy dominate the response (homogeneous broadening) and short timescales in which the static distribution of transition energies dominates (inhomogeneous broadening). Like the static inhomogeneously broadened case, the rise of the time-integrated signal from zero delay is due to the integration up to the full area of the real-time signal, a photon echo [41]. This is similar to the inhomogeneously broadened case derived earlier in that at zero time, there is only half of a photon echo because of causality; the photon echo cannot arrive until after the second pulse, and if τ is zero, only half of the echo can form. Thus as τ is increased from zero to positive delay, the signal rises because of the integration over the developing photon echo.

The non-Markovian photon echo arises from varying atomic spacing at short delays, not Doppler broadening nor static inhomogeneous broadening, from which the photon echo phenomenon was originally observed [42]. At short delay the atoms do not move and thus their resonance frequencies remain constant over the delay. The atoms are at varying distances from one another, resulting in a distribution of transition frequencies due to the varying dipole-dipole interactions, making the vapor effectively inhomogeneously broadened. In this regime the evolution of the coherent superposition between ground and excited state is reversible, and thus the real-time signal is a photon echo. For longer delays, collisions begin to take effect, randomizing the phases of the superpositions such that they cannot rephase as well to produce a photon echo. This intermediate regime occurs when τ is approximately equal to the correlation time. This is in contrast to the static inhomogeneous case, in which the peak of the signal is determined only by the decay of the photon echo, not the loss of photon echo-like behavior. The loss of photon echo-like behavior is clearly exhibited in the real-time signal shown in Fig. 2.11. As the delay between pulses is increased, the photon echo signal decreases, resulting in peaks of the real-time signal at shorter and shorter delays, until eventually the photon echo fails to arrive at all.

The parameters Δ and Λ representing the amplitude and duration of fluctuations determine the timescale of the crossover from homogeneous to inhomogeneous broadening in the time-integrated signal. The decay constant at long times is $T_2 = \Lambda/(2\Delta)^2$. The effect of varying Δ and Λ are shown in Figs. 2.13 and 2.14, respectively. It can be seen that varying Δ results primarily in an increase of the dephasing rate, which affects the location of the peak of the signal versus delay. Varying Λ primarily affects the delay of the peak, faster fluctuations resulting in earlier crossovers from inhomogeneous to homogeneous broadening.

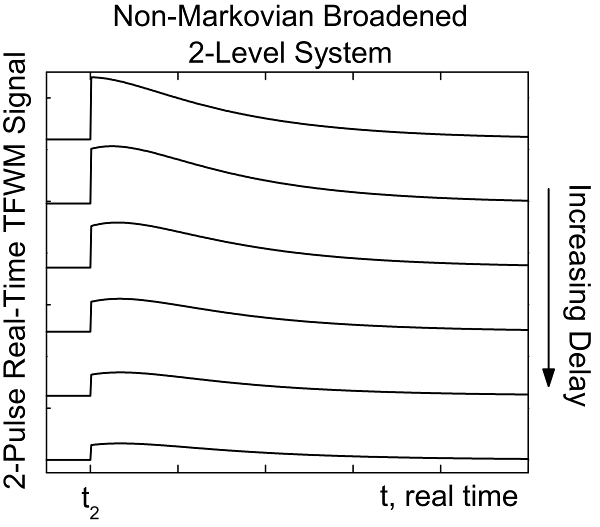

Figure 2.11: Calculated 2-pulse time-resolved TFWM signal for a non-Markovian broadened 2-level system.

To see the effect on the TFWM signal of having two excited states instead of just one, we calculate the 2-pulse TFWM signal for the case of a three-level system using the response functions derived above. We choose the spacing of the excited state energy levels to match that between the potassium D_1 and D_2

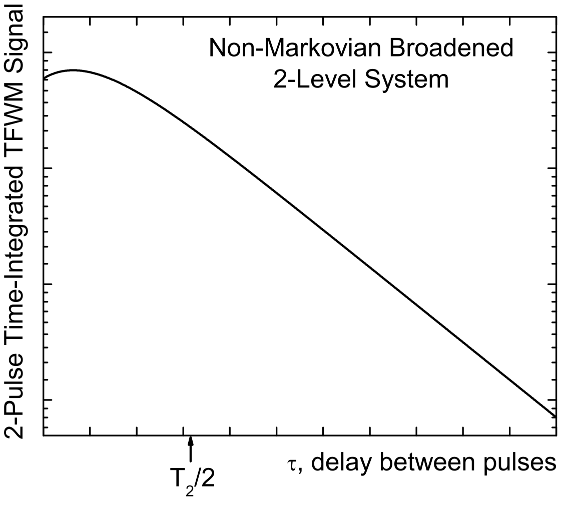

Figure 2.12: Calculated 2-pulse time-integrated TFWM signal for a non-Markovian broadened 2-level system (natural log scale).

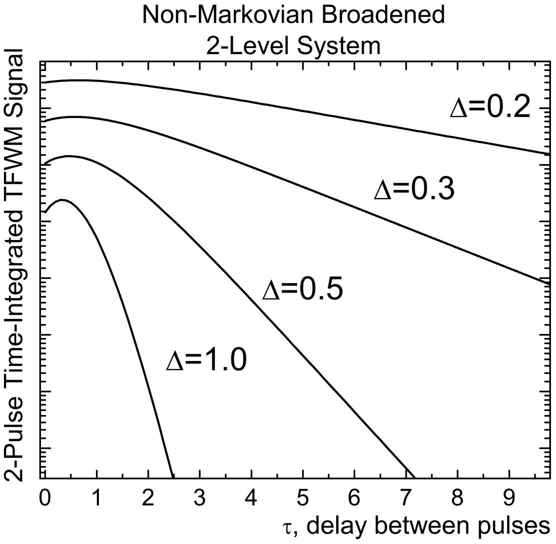

Figure 2.13: Calculated 2-pulse time-resolved TFWM signal for a non-Markovian broadened 2-level system (natural log scale). Varying the correlation function parameter Δ, representing the root-mean-square amplitude of the fluctuations.

lines studied in the experiments. The resulting time-integrated 2-pulse TFWM

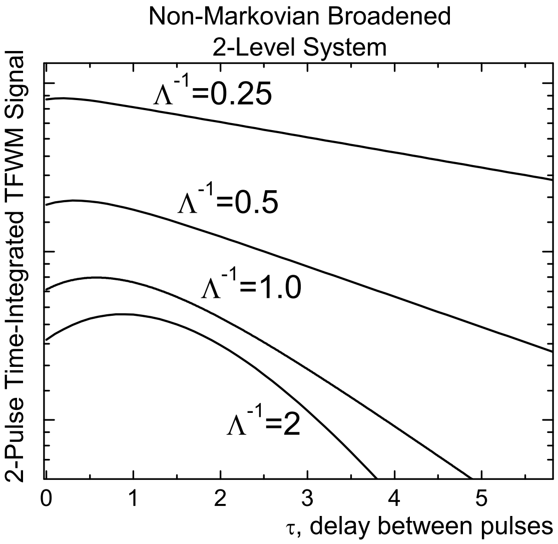

Figure 2.14: Calculated 2-pulse time-integrated TFWM signal for a non-Markovian broadened 2-level system (natural log scale). Varying the correlation function parameter Λ^{-1}, representing the timescale of the fluctuations.

signal is shown in Fig. 2.15. The beating exhibited by the signal is a result of the quantum interference of the two excited state pathways, with the beat frequency corresponding to the frequency difference between the levels. In addition, if the levels have different dipole moments or are excited with different intensities the amplitude of the modulation in the beats will decrease.

Finally, we consider the case of 3-pulse TFWM. Although the particular sequence and arrangement of pulses will be described in detail in the experimental chapter, we consider here how separating the second and third pulses gains added insight into the physics of non-Markovian dynamics. In particular, it has been shown that varying the delay τ between the first and second pulse for various values of the delay T between the second and third pulse allows the mapping out of the correlation function of frequency fluctuations [43]. This may not be surprising considering that the response functions are so intimately related to the correlation

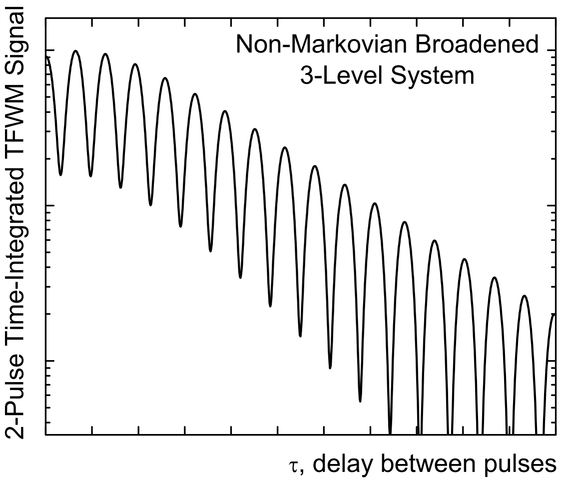

Figure 2.15: Calculated 2-pulse time-integrated TFWM signal for a non-Markovian broadened 3-level system (natural log scale).

function through the line shape functions. Physically this seems reasonable as well considering that varying the second delay probes changes that occur while the system is in the intermediate density matrix state corresponding to population. By changing that time interval we have access to the timescales of the randomization process that result in the loss of rephasing capability. That is, because the photon echo cannot arise until after the third pulse reverses the evolution of the coherent superposition created by the first pulse, varying the second-third pulse delay "exposes" the coherence to variable durations of randomizing collisions. It is just these randomizing collisions that determine the form of the correlation function.

In terms of the actual signals, the effect of increasing the second delay is to shift the peak of the TFWM signal versus the first delay τ towards zero. In other words, increasing the second delay decreases the inhomogeneous system response that determines the peak location in the TFWM signal versus τ. The time-integrated three-pulse TFWM signals for various second delays T are plotted in Fig. 2.16. By determining the peak delay of these signals and plotting this delay as a function of T, a form for the correlation function of frequency fluctuations can be found. This "photon echo peak shift" thus reveals the form of the microscopic correlations involved in the dephasing process. As seen in Fig. 2.17, for the stochastic model chosen in the above derivation we indeed find an exponential peak shift. The exact relationship between the peak shift and the correlation function is just that exhibited by the response functions derived above. In some molecular systems this relationship can be shown to take a more direct form, particularly for systems which exhibit both a fast and slow peak shift decay [43]. The next two chapters on the experimental results and correlation function theory will explore the relationship between the peak shift and the correlation function in more detail for our system.

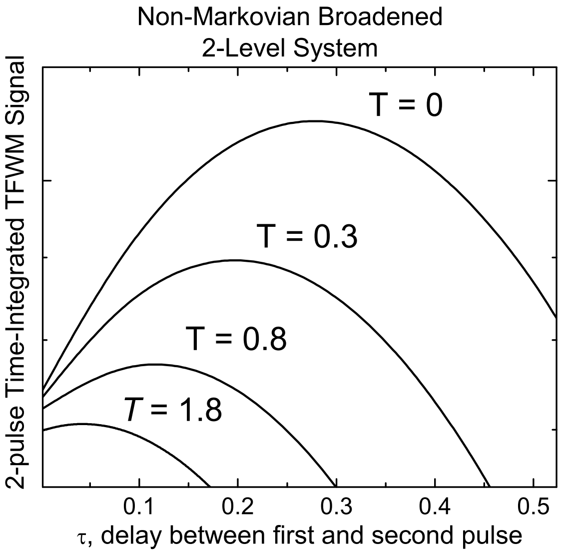

Figure 2.16: Calculated 3-pulse time-integrated TFWM signal for a non-Markovian broadened 2-level system (natural log scale).

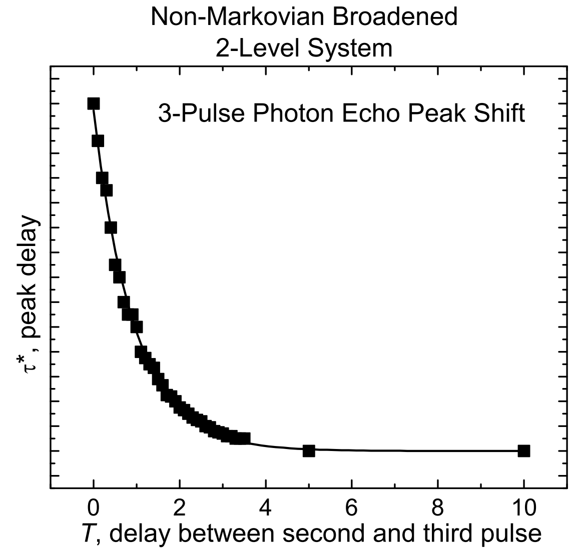

Figure 2.17: Calculated 3-pulse photon echo peak shift for a non-Markovian broadened 2-level system.

Chapter 3

Transient Four-Wave Mixing Experiments and Results

Transient four-wave mixing (TFWM) applied to the study of non-Markovian dynamics is often called the photon echo technique, referring to the photon echo as the signature of non-Markovian dephasing[1] . In this chapter the experimental setups and results will be presented for two- and three-pulse photon echo as well as the time-resolved version of three-pulse photon echo. The results will be analyzed in light of the theoretical results of the previous chapter. Through this analysis the scope of the stochastic theory as well as the effects of resonance broadening will become apparent.

3.1 Experimental Components

Potassium is the element of choice for these experiments because of its simple electronic structure, with energy levels easily accessed by a Ti:sapphire laser (see Fig. 3.1 for a diagram of the optically active energy levels). Potassium is an alkali metal containing 19 electrons, with one valence electron in the 4*s* shell. The two lowest excited states of this valence electron correspond to the D$_1$ and D$_2$ lines at 769.896 nm (1.61 eV, $12,985.17$ cm^{-1}) and 766.490 nm (1.62 eV, $13,042.88$ cm^{-1}), respectively[2] . These lines correspond to the $4^2S_{1/2} \rightarrow 4^2P_{1/2}$

---

[1] Two-pulse photon echo is also known as parametric scattering [27] or self-diffracted TFWM.

[2] The phrase "D lines" comes from Frauenhofer's study of the spectrum of the sun in the early 1800's, resulting in a paper in 1821. He labeled the strongest dark lines across the visible

and $4^2S_{1/2} \rightarrow 4^2P_{3/2}$ fine structure transitions that are split through the spin-orbit interaction. Potassium was chosen over other candidate alkali metals to simplify experiment and theory. In particular, it was chosen over sodium because the potassium D lines are easily attainable by a Ti:sapphire laser, whereas the D lines for sodium lie in the yellow part of the spectrum, which would require a dye laser. Potassium was chosen over rubidium and cesium because the hyperfine splitting of potassium is less than that of these other alkalis, with the potassium hyperfine splitting negligible due to broadening at the experimental densities and temperatures used [45]. Additional properties of potassium are given in App. C.

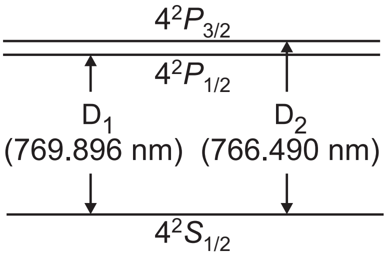

Figure 3.1: Optically active energy levels.

In these experiments a Kerr-lens modelocked Ti:sapphire laser with an extended cavity was used because of its low repetition rate of ~ 26 MHz to reduce accumulation of population in the excited state. The laser pulses are dispersion compensated by a prism pair just downstream of the laser output coupler, resulting in pulses ~ 160 fs long by the time they reach the cell, approximately double the Fourier-transform limited width of 70 fs. Simulations were run to determine the effects of temporal chirp on TFWM and the signals were found to be unaffected by temporal chirp. The pulses are focused onto the interface between the

---

spectrum by the capital letters A in the red to H in the violet; the D line turned out to be a doublet, thus becoming D_1 and D_2. It was not until twenty-seven years later that the connection was made to the already-known spectral lines of sodium. His notation remains in use today for sodium, and I assume that the similarity of the doublets in other alkali metals promotes their being called the "D lines" also [44].

sapphire window and the potassium vapor by a 25 cm focal-length achromatic doublet lens to minimize chromatic dispersion (a 15 cm singlet lens was used in the two-pulse experiments, which are not as sensitive to dispersion). The broad ($\sim$ 13 nm FWHM) laser spectrum excites both the potassium D_1 and D_2 lines, which are well-separated, resulting in quantum beats at the difference frequency (as derived in the previous chapter). This is in contrast to molecular vibronic spectra, which often contain multiple, overlapping transitions [23]. In addition to the D lines the pulses off-resonantly excite other levels which were examined via the fluorescence as a function of temperature and input laser power, shown in Fig. 3.2. Intensity dependence was measured for the major transitions and both linear and square dependence was found, corresponding to the off-resonant single- and two-photon excitation of higher-lying states such as the atomic 6S and 4D lines and a distinctive molecular band at 670 nm. These do not contribute to the resonant TFWM signal but do reveal the presence of potassium dimers.

The cell used to hold the potassium vapor is custom-made at JILA and consists of a titanium body with a sapphire window for optical access. A detailed description of the potassium cell, its historical development, and directions for its manufacture can be found in App. E. To keep the potassium from condensing onto the sapphire window, higher temperature is maintained at the window than the back of the cell. The densities of the vapor are determined using phenomenological formulae relating the vapor pressure of potassium to temperature, from which the densities are then calculated based on the ideal gas equation[3] [47]. Temperatures up to 800°C are achieved, corresponding to a number density of $\sim 9 \times 10^{18}$ cm^{-3}. For the data presented in this chapter the TFWM signals are detected in reflection because the absorption length of the potassium vapor is on

---

[3] Note the treatment of potassium as an ideal gas is less valid for higher densities and pressures at which phenomenological formulae have been shown to deviate [46]. Thus uncertainties probably arise primarily from the assumption of ideal gas behavior.

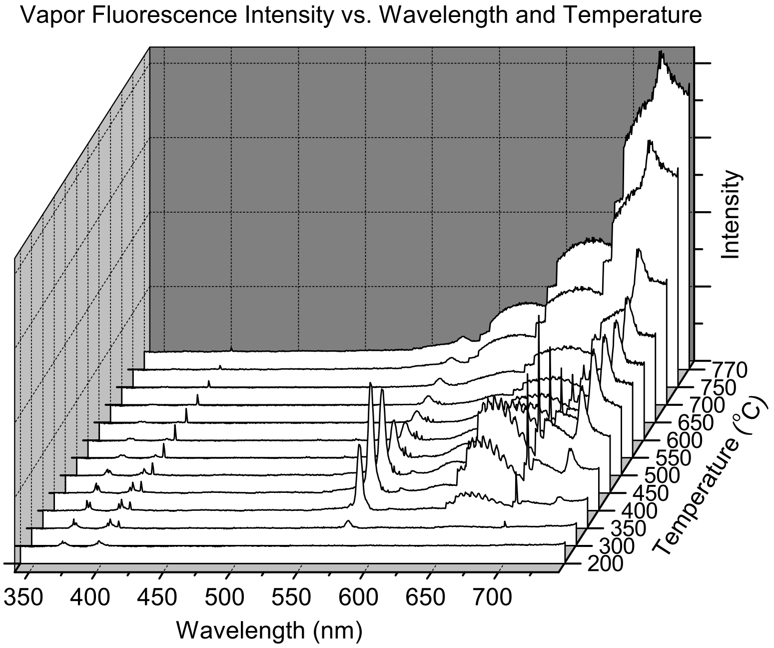

Figure 3.2: Detected fluorescence from potassium vapor excited at 768 nm versus wavelength for various temperatures.

the order of the wavelength of the incident light at these densities. Transmission cells were also manufactured and data were taken in transmission as well; the transmission cells and data are presented in App. E. This quality of short absorption length makes the vapor effectively thin for reflection experiments, which minimizes reshaping of the excitation pulses and reabsorption of the signal. In addition, it has been shown that the reflected signal is equivalent to the transmitted signal for an optically thin sample [48].

The nominal radiative lifetime of potassium is $\sim$ 26 ns, but this is known to be extended due to the trapping of radiation (the emission and reabsorption of real photons) at high densities [49]. To determine the actual radiative lifetime we employed a home-built pulse picker (see App. D for details) to divide down the repetition rate and used a photo-multiplier tube to detect the vapor fluorescence excited by laser pulses with center wavelength tuned to the D lines. The repetition rate was divided by 50, and data were collected using a fast oscilloscope for a series of temperatures ranging from 450°C to 600°C. The fluorescence decay was most visible at 450°C, shown in Fig. 3.3(a), with a decay time of ~ 0.16 μs. The effects of radiation trapping decrease with temperature and density as shown in Fig. 3.3(b), which could be due to the decreasing optical depth in reflection. Thus the extended cavity laser does not have a sufficiently low repetition rate to allow all of the excited state population to relax back to the ground state between pulses. To determine the effects of radiation trapping on transient four-wave mixing experiments, two-pulse TFWM data were taken with and without pulse picking. It was found that the dephasing rate is slightly suppressed due to radiation trapping. The dephasing rate reaches a steady value versus repetition rate starting around 1 MHz. Thus dividing down by 20 pulses seems to be sufficient to reduce the influence of radiation trapping. The pulse picker was used in collecting the two-pulse TFWM data presented here but was not used in the three-pulse experiments due to the pulse picker's heavy toll on pulse intensites and because the signatures of interest in these experiments are not very sensitive to the change in dephasing rate due to radiation trapping. Signal intensities were checked for compliance with cubic dependence on intensity for all of the TFWM data to ensure the suitability of a perturbative treatment. The intensity was found to have a significant influence on the negative delay signal strength of 2-pulse TFWM data, with a larger negative delay signal for lower intensities. This is important for studying the local field effect as described in Ch. 5 but does not affect the signatures of interest in this chapter.

The major broadening mechanisms in a vapor of pure potassium atoms are Doppler and resonance broadening. Doppler broadening arises from the blue- and

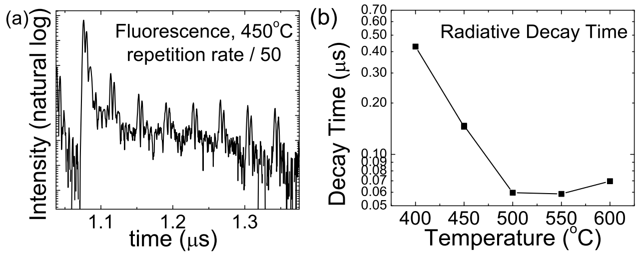

Figure 3.3: (a) Oscilloscope trace of fluorescence intensity versus time. The vapor is excited every 50th pulse, with remnants of the other pulses represented as the smaller peaks. The exponential decay is the radiative decay of the excited state population. (b) The measured decay times as a function of temperature.

red-shifted spectral contributions of atoms moving towards or away from the incident pulses. The varying atomic velocities result in contributions from a large variety of spectral components, resulting in a Gaussian (inhomogeneous) lineshape. Resonance broadening is due to the dipole-dipole interaction between ground- and excited-state atoms of the same species. If the vapor is resonance broadened, the dominant mechanism for dephasing is collisions. Because the dephasing collisions arise from the behavior of like atoms, the vapor is homogeneously broadened in this limit. In order to study the non-Markovian dephasing process we then work at densities at which resonance broadening dominates over Doppler broadening. These densities correspond to temperatures above $\sim$ 350°C (see Fig. 3.4). Thus the experimental results shown below were taken with the vapor above this temperature, which corresponds to densities $> 8 \times 10^{16}\text{cm}^{-3}$.

We now introduce the two- and three-pulse photon echo experiments and results.

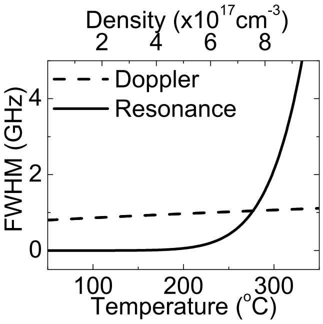

Figure 3.4: Theoretical linewidths for resonance and Doppler broadening.

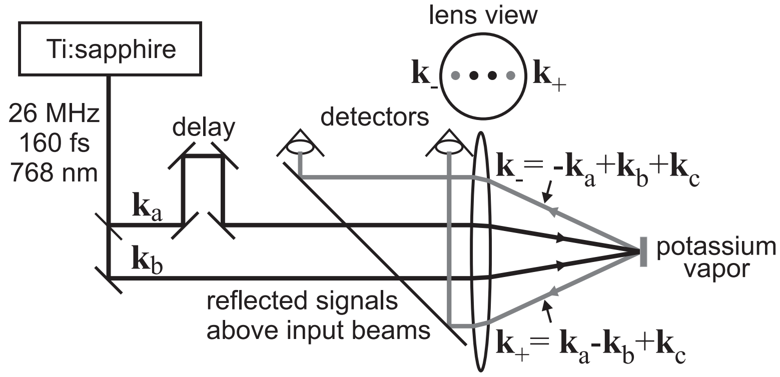

Figure 3.5: The 2-pulse photon echo experimental setup.

3.2 The Two-Pulse Photon Echo Experiment and Results

As a description was given for three-pulse TFWM in the previous chapter, here we give only a brief description of the two-pulse transient four-wave mixing process, which when applied to the study of non-Markovian dynamics is called the two-pulse photon echo technique (2PE). In the 2PE experiment, shown in Fig. 3.5, two pulses with wavevectors $\mathbf{k}_a$ and $\mathbf{k}_b$ and center frequency tuned to resonance are incident on the dense vapor. The first pulse, with wavevector $\mathbf{k}_a$, induces a coherence between the ground and excited states of the atoms with a spatial phase across the vapor determined by its angle of incidence and wavelength. After some delay τ, the second pulse, $\mathbf{k}_b$, produces an excited state population whose amplitude is greatest in areas where the coherence left by the first pulse constructively interferes with the second pulse and least where they destructively interfere. Thus the excited state population is spatially modulated, forming an amplitude grating with periodicity $\mathbf{k}_b - \mathbf{k}_a$. At the same time it creates the grating, the second pulse also scatters off the grating (i.e. creates a coherence that radiates) into the direction $2\mathbf{k}_b - \mathbf{k}_a$. This background-free signal is time-integrated by a slow photodiode detector. The scattered signal has an intensity proportional to the amplitude of the population grating. By varying the time delay between pulses, τ, the transient behavior of the induced polarization can be investigated. Note that the use of subscripts a and b instead of numbers is to represent the fact that signals in either direction can be detected, and thus there is a different ordering corresponding to positive and negative delay depending on which signal is detected. That is, for the signal in direction $2\mathbf{k}_b - \mathbf{k}_a$ "negative delay" corresponds to $\mathbf{k}_b$ arriving first, while for the signal in direction $2\mathbf{k}_a - \mathbf{k}_b$ negative delay corresponds to $\mathbf{k}_a$ arriving first. Thus we do not label the wavevectors with numbers in order to prevent confusion of the geometrical orientation with the pulse sequence.

Typical experimental results are shown in Fig. 3.6. The detected signal intensity is plotted as a function of the delay between pulses. The signal exhibits quantum beats due to that fact that two energy levels are excited, as was confirmed theoretically in the previous chapter. The important aspect of this signal is that it initially increases at short times, peaks and then exponentially decays at long times. This behavior corresponds to that predicted in the previous chapter for a non-Markovian broadened system. Thus the 2PE signal contains signatures of both non-Markovian and Markovian dynamics. Indeed, the dynamical signatures are well-separated (see Fig. 3.6) as an initial rise of the signal caused by the integration of the developing photon echo, a flat signal at short delays due to non-Markovian scattering, and exponential dephasing due to pure homogeneous broadening. The extra dip near zero delay is a result of the signal following the integration of the pulses, which have a finite duration. The 2PE experiment was performed for a series of densities and temperatures. The results are plotted in Fig. 3.7. As temperature and density increase, the range of non-Markovian dynamics decreases. This agrees with the reasoning that the collision duration and time between collisions should decrease with increasing temperature and thus that the range of non-Markovian dephasing should decrease with temperature. This argument is made more quantitative below through the application of the non-Markovian theory.

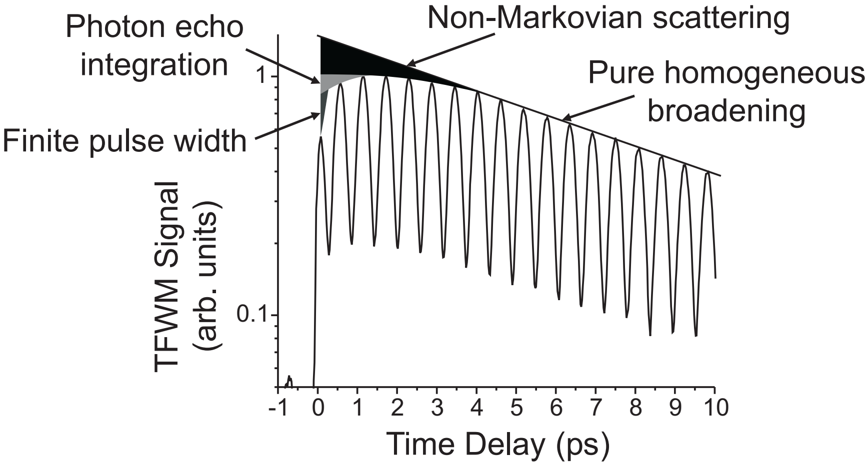

Figure 3.6: Experimental two-pulse photon echo signal for potassium vapor at 500°C (number density $\sim 3.4 \times 10^{17}$ cm^{-3}) with dynamical signatures labeled. Quantum beats are due to the excitation of both the potassium D resonance lines.

In this experiment the dephasing time, collision duration and pulse width are all well-separated. Based on thermal velocities calculated assuming ideal gas behavior and the range of the attractive part of a typical interatomic potential energy surface, at 700°C the collision duration is approximately 0.5 ps. This collision duration is much less than the time between collisions of 2 ps (based on the dephasing time) and much greater than the pulse duration of 180 fs. In ad-

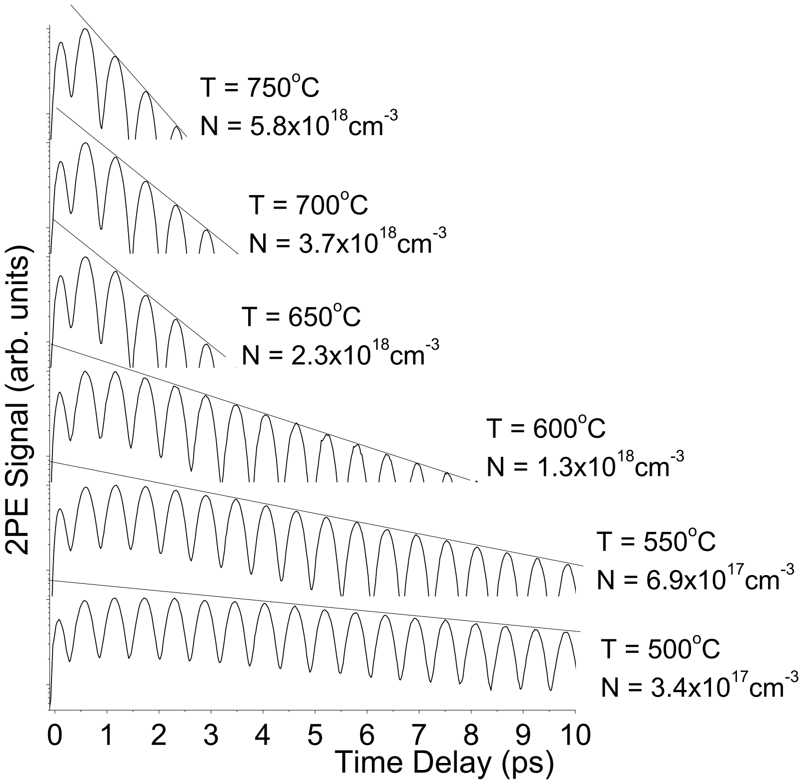

Figure 3.7: Experimental two-pulse photon echo signals for various temperatures and densities (log scale), with lines drawn to highlight the non-exponential behavior at short times. The non-Markovian behavior decreases with increasing temperature and density.

dition, this estimated value for the collision duration agrees well with the delay at which the signal peaks, which according to the theory corresponds to approximately the correlation time Λ^{-1}. In condensed phase systems the timescale of fluctuations can be on the order of 200 fs [18], with dephasing due to solvent interaction also occuring at ultrafast timescales [20]. Thus the above experimental results exhibit unusually well-separated contributions from homogeneous and inhomogeneous broadening as compared to molecules in the condensed phase. We also note that we do not need to be concerned with contributions from other time orderings that occur during pulse overlap. Indeed, with such a model system, this is an opportunity to test the non-Markovian theory derived in the previous chapter that is often used in more complex molecular systems. To do so we use the response functions derived in the previous chapter for 2PE in a three-level system. Least-square fits are made to the experimental data with the only fitting variables being the parameters of the stochastic correlation function Δ_{ij} and Λ_{ij} for the two transitions.

Theoretical results match quite well with the experimental results via least-square fits, as shown in Fig. 3.8. The discrepancy near zero delay is due to the assumption of delta-function pulses in time, which does not allow for finite pulse width effects. The fit parameter Λ_{ij} corresponds to the decay rate of the correlation function and determines the time scale of the deviation of the 2PE signal from exponential behavior at short delays. To confirm that these signatures arise from non-Markovian dephasing, fits were made to the data for various temperatures and as expected Λ_{ij} increases with increasing temperature, as shown in Fig. 3.9. This represents a decreasing collision duration. The magnitude of the excited state frequency fluctuations is represented by the parameter Δ_{ij}, which is also plotted in Fig. 3.9. The ratio $\kappa = \Lambda_{ij}/\Delta_{ij}$ is of order 1, which means that the broadening mechanism is intermediate and not in either the homogeneous or inhomogeneous limits.

The excellent fit between theory and experiment demonstrate that the stochastic model adequately describes the dynamics. The stochastic model does not take into account memory in the bath, as occurs, for example, in semiconductors due to electron-LO-phonon scattering [50]. Memory in the bath results in oscillatory dephasing, so the fact that we do not see oscillatory dephasing implies that a model that includes such a microscopic description of the bath [51, 52] is not needed[4] . The stochastic model does not include resonance broadening effects;

---

[4] For an atomic system “the bath” is all the other atoms.

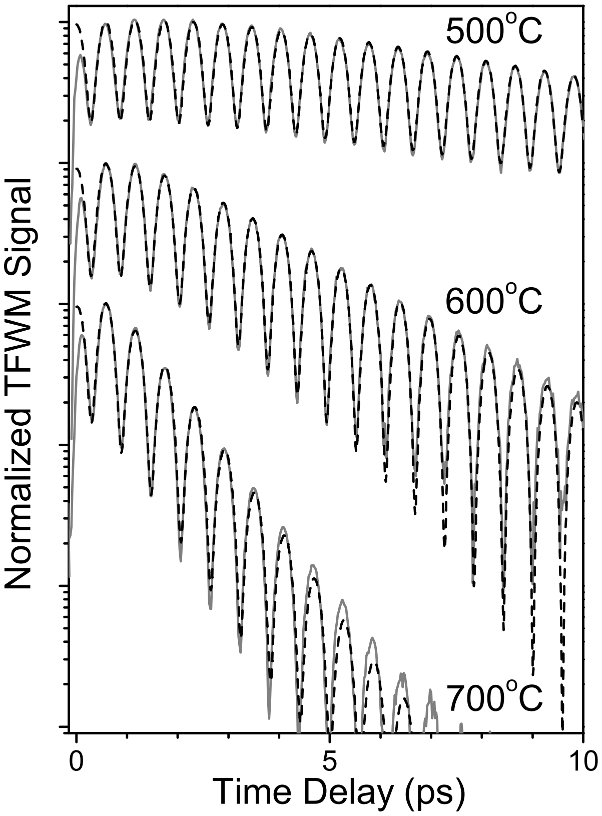

Figure 3.8: Typical experimental 2-pulse photon echo signals (solid grey lines) for potassium vapor at 500°C ($N \approx 3.4 \times 10^{17}\text{cm}^{-3}$), 600°C ($N \approx 1.3 \times 10^{18}\text{cm}^{-3}$), and 700°C ($N \approx 3.7 \times 10^{18}\text{cm}^{-3}$), with curves offset for clarity. The dashed lines are least-square fits assuming a stochastic modulation of the electronic transition frequency during collisions.

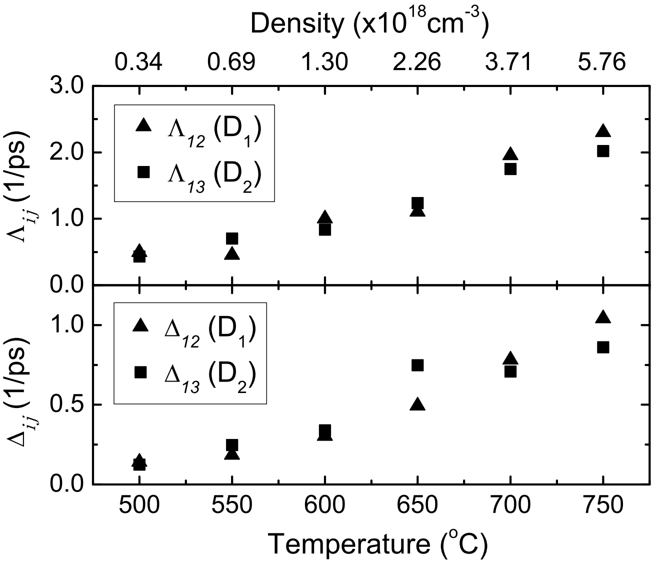

Figure 3.9: Stochastic theoretical fitting parameters Λ_{ij}, the timescale of the excited state frequency fluctuations, and Δ_{ij}, their magnitude, for the D$_1$ (square) and D$_2$ (triangle) line.

thus, differences will exist in comparison with a foreign-gas broadened vapor in which the interaction range and therefore the collision duration is relatively small. The deviation of the inverse collision duration from square-root dependance on temperature may indicate the importance of the resonant interactions. This can be explored experimentally by introducing a buffer gas to the potassium vapor, which would decrease the interaction range and bring the system to the Markovian, homogeneously broadened limit (see Ch. 6 for a description). Performing such an experiment would grant the ability to determine signatures unique to resonance broadening. In addition, further insight can be gained with a three-pulse photon echo experiment, which as mentioned in the last chapter can enable the mapping out of the correlation function of the system [43, 53, 54]. This latter experiment is the subject of the next section.

3.3 The Three-Pulse Photon Echo Experiment and Results

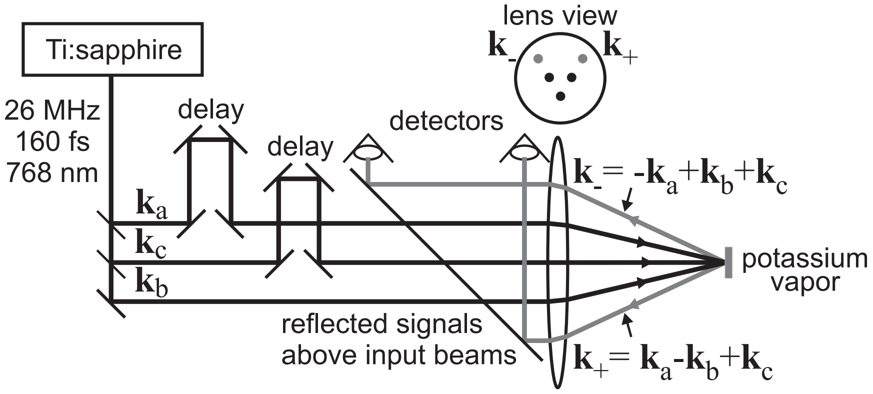

Figure 3.10: The time-integrated 3-pulse photon echo experimental setup. The signals are detected in reflection due to the small absorption length ($\sim \lambda/2$) of the potassium vapor.

The experimental setup for three-pulse TFWM, known as three-pulse photon echo (3PE) in non-Markovian spectroscopy, is shown in Fig. 3.10. Figure 3.11

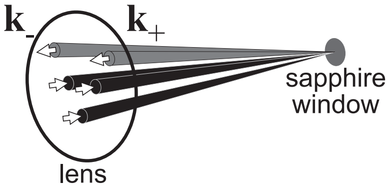

Figure 3.11: The three-pulse photon echo experimental geometry.

shows the pulse geometry. The 3PE technique extends the previous experimental arrangement by adding a third pulse. The pulses once again are labeled alphabetically to imply that time ordering is dependent on the geometry of the detected signal. The first pulse excites a coherence between the ground and excited states. During the ensuing delay τ, dephasing occurs due to collisions. Then the second pulse arrives and converts the remaining coherence to excited-state or ground-state population. During the second delay T, loss of population and spectral redistribution occurs due to natural decay and collisions, and the system's ability to rephase and form a photon echo decreases. The third and final pulse forms a third-order coherence that radiates as the signal. The time-integrated 3PE is measured by scanning the first delay τ for various fixed values of the second delay T, with negative delay corresponding to the conjugate pulse coming second. A schematic of the pulse ordering for different time delays is shown in Fig. 3.12. The 3PE signal is more sensitive to the beam geometry that the two-pulse case. In particular, the beams must be parallel to observe the proper population decay as a function of T, as shown in Fig. 3.13.

As exhibited by the data shown in Fig. 3.14, and considering only the $\mathbf{k}_-$ signal for simplicity, for $\tau > 0$ the overall signal versus τ (ignoring the quantum beating due to simultaneous excitation of both excited states) rises, peaks, and then exponentially decays. This is the same behavior as exhibited by the 2-pulse photon echo signal. Across the peak, the real-time signal changes from a

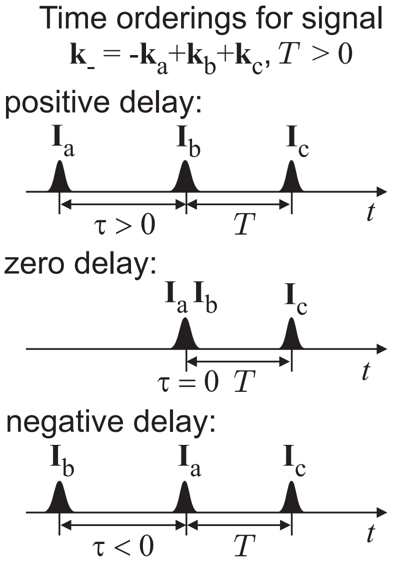

Figure 3.12: Time delays of the three-pulse photon echo experiment.

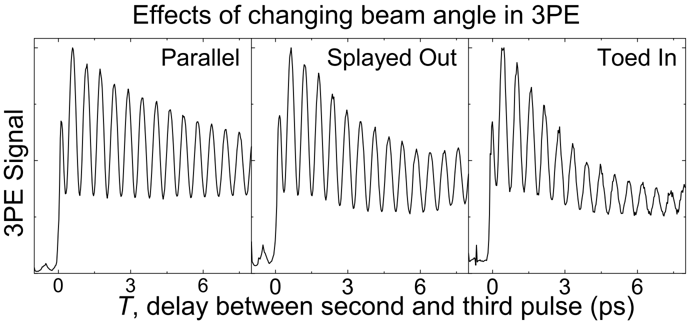

Figure 3.13: Dependence of the population decay (taken by varying T for fixed τ) on beam angle. The beams must be aligned parallel before the focusing lens for the population decay to be properly measured.

photon echo to free polarization decay, corresponding to the crossover from non-Markovian to Markovian dynamics. As the second delay T is increased, the signals reveal how the system's ability to form a photon echo changes. For the case of the first delay τ being less than the correlation time, we can divide the dynamics into three regimes as a function of the second delay T (see Fig. 3.15). For T less than the correlation time, the non-Markovian dynamics at short times results in a real-time signal that is a photon echo, but the intensity is slightly decreased due to the collisions that occur during the second delay. The dotted line in the schematic represents what the signal would be if T were zero. For T much greater than the correlation time, the dephasing during the second delay completely precludes a photon echo from forming, as shown in the figure for the Markovian regime. In the time-integrated signal, this results in a shift of the peak toward $\tau = 0$. Thus varying the second delay allows a probe of the loss of photon echo-like behavior during the transition to homogeneous broadening. To determine the peak shift, data are taken as a function of τ for the second delay T at the beat maxima of the population signal for best signal-to-noise. The scans of τ for each of these T are then analyzed by fitting a Gaussian to each beat, determining the maxima delays versus τ of the Gaussian fits, and fitting these delays in turn with a Gaussian to find the overall peak of the 3PE signal. Three-pulse photon echo data were taken for a series of temperatures and densities. The resulting 3PE peak shifts, or 3PEPS, are shown for a series of temperatures in Fig. 3.16.

For some molecular systems the 3PEPS reveals the two-time correlation function of frequency fluctuations directly [23]. However, this is only possible due to a theoretical simplification arising from the presence of both fast and slow modulation in the system. For a dense atomic vapor, such simplifications do not necessarily occur, but a qualitative form for the correlation function can be found from the 3PEPS. The experimental peak location versus τ is exponential at lower temperatures and thus qualitatively supports the use of an exponential correlation function in modeling two-pulse experiments, as was done for the 2PE signals above [55]. The peak shift is bi-exponential above 500°C. The fitting functions shown in the figure are of the form

$$\Delta_1^2 \exp(-\Lambda_1 T) + \Delta_2^2 \exp(-\Lambda_2 T), \tag{3.1}$$

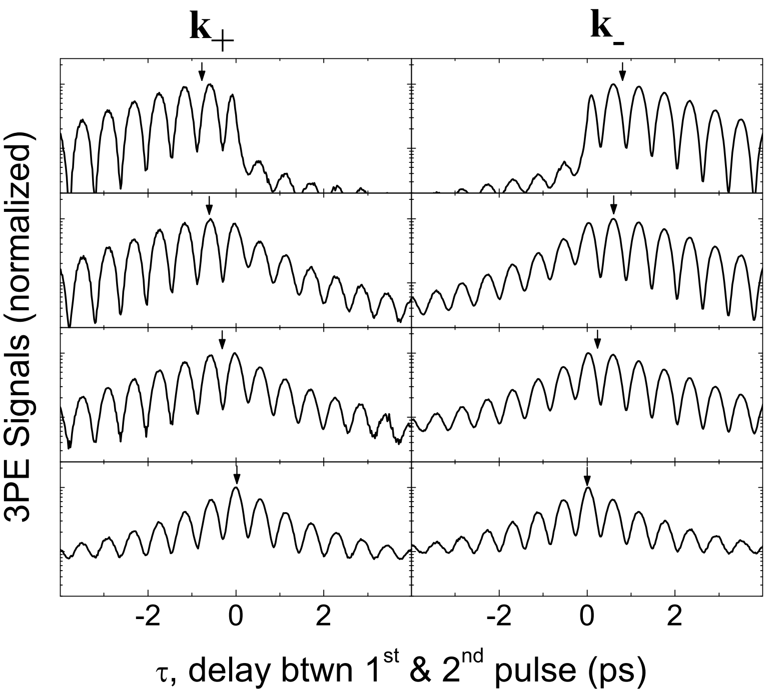

Figure 3.14: Experimental 3-pulse photon echo signals at 600°C (1.3×10^{18}cm^{-3}) for $T = 0.58$ ps to 36 ps. The peak of the signal, marked by an arrow in the figure, shifts to $\tau = 0$ ps due to the loss of rephasing capability.

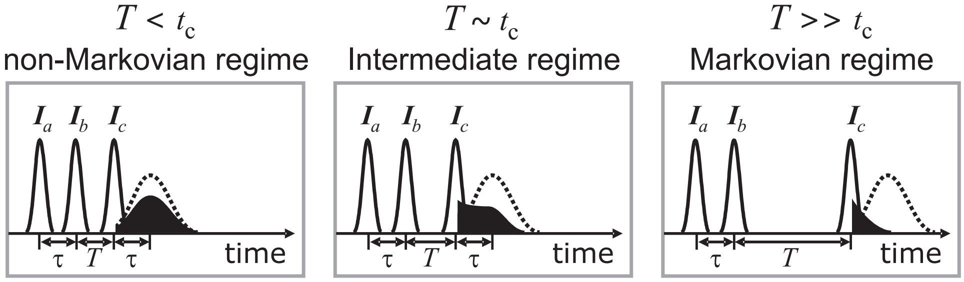

Figure 3.15: Schematic of regimes for $\tau < t_c$ (τ in the non-Markovian regime). Real-time signals are shown in solid black for the cases of T in the non-Markovian, intermediate and Markovian regimes. Dotted lines represent the signal for perfect rephasing.

where the subscripts 1 and 2 refer to the fast and slow exponentials, respectively.

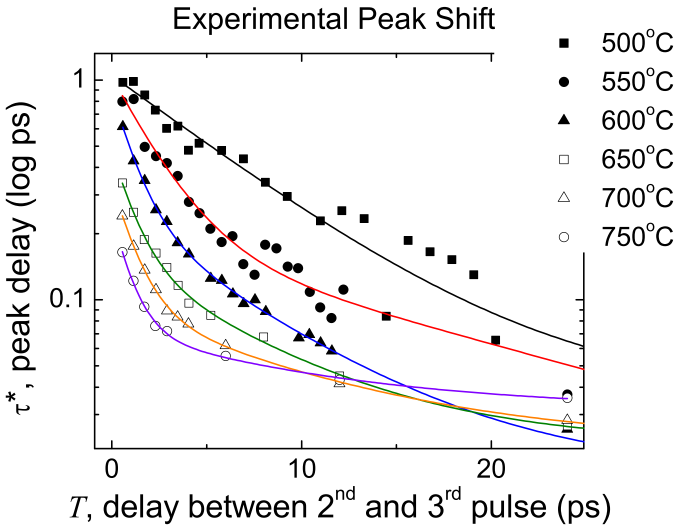

Figure 3.16: 3PEPS for a series of temperatures and densities with bi-exponential fits (lines).

The amplitudes Δ_i^2 and time constants $1/\Lambda_i$ for the exponentials are plotted in Fig. 3.17. This bi-exponential behavior could represent the presence of two collision mechanisms, such as both short-range/binary/hard and long-range/many-body/soft collisions, the latter being due to resonance effects at these high densities [56]. Alternatively, it could be due to contributions from higher-order powers of the correlation function [57]. The current theory does not account for resonance broadening, which dominates at these high densities [58]. To take resonance effects into account and gain a more complete description of the system response, we performed molecular dynamics simulations in an exciton picture and calculated the correlation function of one-exciton frequency fluctuations. Using these correlation functions we then calculated the 3PEPS signals [59]. This work is presented in the next chapter.

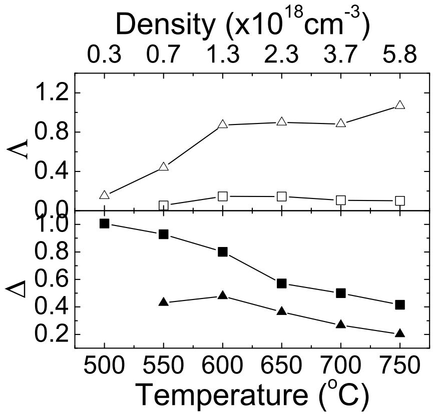

Figure 3.17: Experimental 3-pulse photon echo peak shift fitting parameters Δ and Λ for the fast (square) and slow (triangle) exponentials.

3.4 The Time-Resolved Three-Pulse Photon Echo Experiment and Results

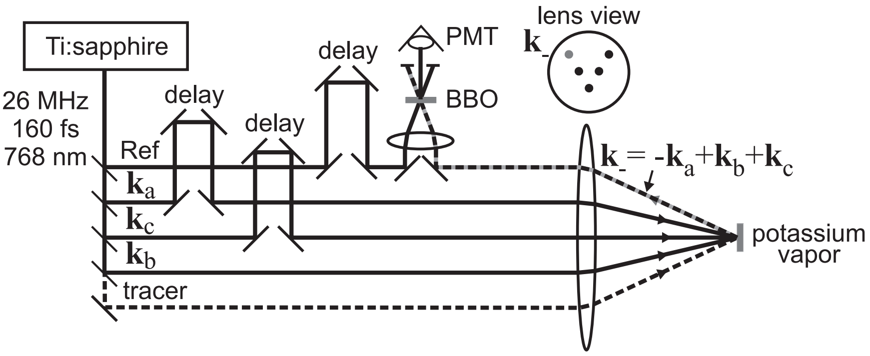

Figure 3.18: The time-resolved 3-pulse photon echo experimental setup.

We also performed the time-resolved version of the 3PE experiment to gain more insight into the correlation function experimentally. In the time-resolved version of 3PE (time-gated 3PE), a reference pulse is correlated with the emitted 3PE signal at a particular τ and T in a BBO crystal for up-conversion, resulting in a time-resolved scan of the nonlinear response. In the setup, shown in Fig. 3.18, the beam from the laser is split into five arms, three corresponding to the three beams used for four-wave mixing, one used as a tracer for the TFWM signal from the vapor, and one used as a reference for upconversion of the TFWM signal. Three delay stages are used to form the delays between pulses, with two stages before the cell for the τ and T delays and one after the cell for signal upconversion with the reference. Data are taken for various τ and T as a function of the delay between the signal and the reference, t. Results are shown in Fig. 3.19.

The presence of the photon echo is clearly seen in the time-resolved signal (Fig. 3.19). As a function of τ we can see that the signal exhibits a free polarization decay and a photon echo for small T. As τ is increased, the photon echo moves to the corresponding delay. As T is increased this photon echo-like behavior goes away. This is an unusually clear example of the utility of the three-pulse photon echo technique for probing non-Markovian dynamics.

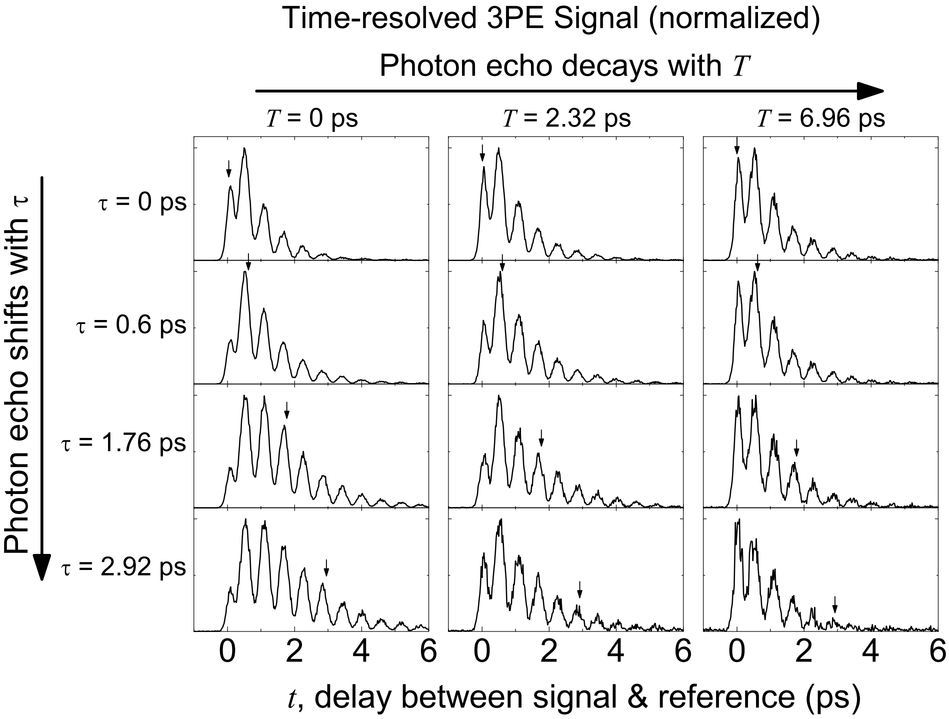

Figure 3.19: Experimental time-resolved 3-pulse photon echo signals at 600°C ($1.3 \times 10^{18}\text{cm}^{-3}$). Small arrows point to $t = \tau$, the photon echo location for perfect rephasing. Photon echo strength clearly decreases with increasing T.

Chapter 4

Correlation Functions from Molecular Dynamics Simulations in an Exciton Picture

In this chapter the experimental three-pulse photon echo results are compared to calculated correlation functions of frequency fluctuations from molecular dynamics simulations in the exciton formalism. Although fits using the stochastic model are excellent for the two-pulse photon echo experimental results, the bi-exponential behavior of the 3PEPS at high density cannot be explained by a single exponential correlation function. Even if it could, the insight the stochastic theory provides into the dynamics of the system is limited by our assumed correlation function. In addition, adding resonance effects is interesting from a purely theoretical point of view as to how it might change the 3PEPS as well as potential experimental signals for varying buffer gas pressure and the spectra obtained from 2D spectroscopy, in which crosspeaks reveal excitonic coupings (see Ch. 6 for a brief description of the latter). Understanding the influence of excitonic effects would provide insight into the interactions of a resonance-broadened vapor in particular as well as other disordered excitonic systems such as molecular aggregates, semiconductors and biological systems. Potassium vapor is an ideal system in which to study disordered excitons due to its electronic simplicity and its easily adjusted density and temperature.

4.1 The Exciton Formalism

The model used for the two-pulse experiment is the equivalent of a foreign gas model because we do not consider the interaction of atoms with atoms but rather assume the interactions of a particular atom can be averaged into the fluctuations of “the bath,” which in the case of a vapor are “all the other atoms.” This model holds for foreign-gas broadened vapors because dephasing collisions are short-range and thus spatially extended couplings of energy levels do not arise. For a resonance-broadened vapor, the range of interaction between atoms is significantly more long-range, meaning at the least binary interactions must be taken into account. The exciton model facilitates binary as well as higher-order interactions [60]. The concept of excitons enables us to write a diagonal Hamiltonian for a system which fits neither the concept of a solid with bands nor that of a random ensemble of separated atoms. This is done by working intermediately between k-space and real space using the orthogonal states of excitons. An exciton can be considered a quasiparticle representing a system of coupled oscillators. Generally, for a system of N atoms there will be N one-exciton (all electrons in the ground state except one electron in the excited state) states and $N(N-1)/2$ two-exciton (all electrons in the ground state except two) states, and so on. A schematic of such a level scheme is shown in Fig. 4.1. An example derivation of the exciton levels for a system of two 2-level atoms is given in App. F. The fluctuating exciton Hamiltonian (including two-exciton states) is

$$H_S = \sum_m \Omega_m \hat{B}_m^\dagger \hat{B}_m + \sum_{m,n}^{m\neq n} (J_{mn} \hat{B}_m^\dagger \hat{B}_n + K_{mn} \hat{B}_m^\dagger \hat{B}_n^\dagger \hat{B}_m \hat{B}_n), \tag{4.1}$$

where

$$\hat{B}_m^\dagger = |m1\rangle\langle m0| \tag{4.2}$$

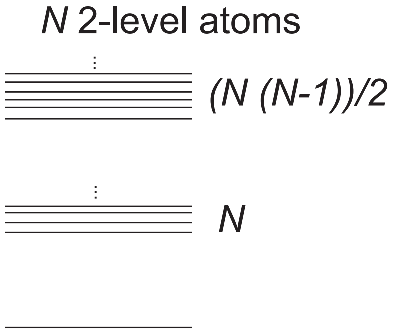

Figure 4.1: Schematic of one- and two-exciton states for N atoms.

and

$$\hat{B}_m = |m0\rangle\langle m1| \tag{4.3}$$

are the exciton creation and annihiliation operators, J_{mn} is the one-exciton coupling parameter between atoms m and n and K_{mn} that for the two-exciton. For 2 atoms ($N = 2$) we have the following relationship between the atom basis and exciton basis:

Atom basis $\rightarrow$ exciton basis:
atoms m, states a states e_m
$|ma\rangle|ma\rangle \rightarrow |e_m e_m\rangle$
1 ground state:
$|10\rangle|20\rangle \rightarrow |00\rangle$
$N = 2$ one-exciton states:
$|10\rangle|21\rangle \rightarrow |01\rangle$
$|11\rangle|20\rangle \rightarrow |10\rangle$
$N(N-1)/2 = 1$ two-exciton states:
$|11\rangle|21\rangle \rightarrow |11\rangle$.

As a first step to improving the theoretical treatment we decided to consider only the formation of one-exciton states. Within the one-exciton formalism there are a number of ways we could imagine improving the theoretical treatment of dense vapors. One approach is to attempt an analytical model in which N one-exciton states are assigned a distribution of values corresponding to the typical energies for a particular density. Unlike atoms in molecules that oscillate about some mean distance from other atoms, atoms in a vapor vary drastically in distance from one another. Thus the experimental bandwidth of the incident pulses would be the restraining factor on the range of energies such that only excitons with energies within the laser bandwidth would contribute. The fluctuations of the exciton energy levels then could be applied via a stochastic model for each exciton energy level. This approach would represent binary interactions as well as provide additional fitting parameters, but still assumes a form for the correlation functions.

An alternative approach would be to use molecular dynamics (MD) simulations, in which we consider a cluster of atoms that undergo a dynamic trajectory. This approach would not need the stochastic model as an assumption, but rather would calculate a correlation function based on the configurations of the atoms from the simulated trajectories using interatomic potential energy surfaces. This approach and its results are described in this chapter. To calculate the correlation function from molecular dynamics (MD) simulations we took four main steps: 1. simulate trajectories of an ensemble of atoms, 2. determine the resonant exciton couplings $J_{m,n}$ based on distances between atom pairs for each snapshot of the trajectory, 3. diagonalize the one-exciton Hamiltonian and 4. calculate the correlation functions and peak shifts. We begin with a description of the MD simulation.

4.2 Molecular Dynamics Simulations

For the MD simulation, a 600 ps dynamic trajectory for a simulation unit cell containing 10 to 40 potassium atoms in the gas phase was generated from the ground state potential energy surface (PES) of K_2 using the molecular dynamics package GROMACS [61] (see App. G for details about the package). The ground state potential energy surface was approximated by a Buckingham potential function fit to the $1^1\Sigma_g^+$ ground state surface of K_2, which was calculated via a one-electron non-empirical pseudopotential method by [62]. The Buckingham potential function is represented as

$$V(r) = A\exp(-Br) - \frac{C}{r^6}. \tag{4.4}$$

The fit to the ground state is shown in Fig. 4.2. The ground state potential function was truncated in the simulation at 5 nm, at which distance the potential reaches a value 10^{-7} times less than the potential minimum.

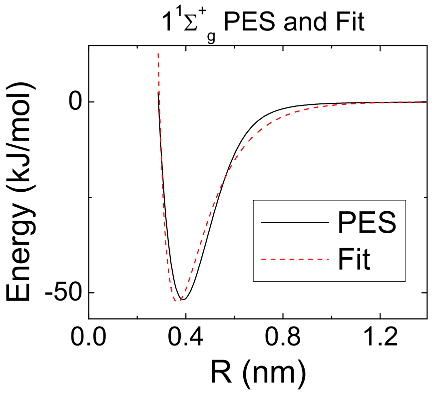

Figure 4.2: The $1^1\Sigma_g^+$ ground state surface and Buckingham potential fit used in the molecular dynamics simulation. [Surfaces provided in S. Magnier *et al.*, J. Chem. Phys. **121**, 1771 (2004).]

Twenty runs were performed for each temperature, each run 6000 steps long with a 0.002 ps time step, with the atom positions written to the output every 10 steps, resulting in a resolution of 0.02ps. Weak temperature coupling to a bath at the experimental temperatures of the cell window was applied through a Berendson algorithm provided by the GROMACS program. The Berendson algo-

Table 4.1: Simulation box side lengths for 10 and 20 atoms.

Temp (°C)	Density (m^{-3})	Box (nm) 10 atoms	Box (nm) 20 atoms
300	4.815×10^{21}	127.585	160.748
350	1.8355×10^{22}	81.6736	102.902
400	5.660×10^{22}	56.1127	70.6976
450	1.4775×10^{23}	40.7528	51.3453
500	3.375×10^{23}	30.9439	38.9869
550	6.920×10^{23}	24.3574	30.6884
600	1.298×10^{24}	19.7504	24.8839
650	2.2625×10^{24}	16.4111	20.6767
700	3.706×10^{24}	13.9219	17.5405
750	5.7610×10^{24}	12.0181	15.1418

rithm slowly corrects for deviations of the system temperature T as determined from atom velocities from the bath temperature T_0 according to the equation $dT/dt = (T_0 - T)/\tau$, where τ was set to be 0.1 ps in the simulations. No pressure coupling was applied (i.e. the box size remained constant throughout the simulation). The box size was scaled to include the same number of atoms for each temperature (see Table 4.2 for a list of box side lengths for the temperatures considered). The temperatures used for this scaling were the experimental temperatures at the vapor cell nut (where the potassium rests in liquid form and determines the vapor pressure). Atomic positions were set by the C command `rand()` for each run, and initial velocities were randomly generated for each run by the GROMACS program according to the Maxwell distribution for an ideal gas.

4.3 Resonant Exciton Couplings

The resonant couplings arise from the attractive or repulsive nature of atomic interaction, so interatomic potential energy surfaces represent the amplitude and range of the transition frequency fluctuations for the case of pairwise interaction. Thus for each snapshot of the trajectory, the resonant exciton couplings $J_{m,n}$ were determined for each pairwise atomic distance as the value of the difference between the $1^1\Sigma_u^+$ excited state potential energy surface and the $1^1\Sigma_g^+$ ground state surface of K_2 [62]. Only the $1^1\Sigma_u^+$ was used in the calculation; all other surfaces dissociating to 4s + 4p (as plotted in Fig. 4.3) were not taken into account, nor were transitions from the other ground state (see both ground states in Fig. 4.4). The surfaces used in this calculation are plotted in Fig. 4.5. The $J_{m,n}$ were input into the fluctuating Frenkel exciton Hamiltonian, defined by

$$\hat{H}_S = \sum_m \Omega_m \hat{B}_m^\dagger \hat{B}_m + \sum_{m,n}^{m\neq n} J_{m,n} \hat{B}_m^\dagger \hat{B}_n, \tag{4.5}$$

where Ω_m is the excitation energy of atom m, chosen to be $\Omega_m = \Omega = 13024.0162\ \mathrm{cm}^{-1}$ [60]. Two-exciton states, or quartic couplings, were not taken into account.

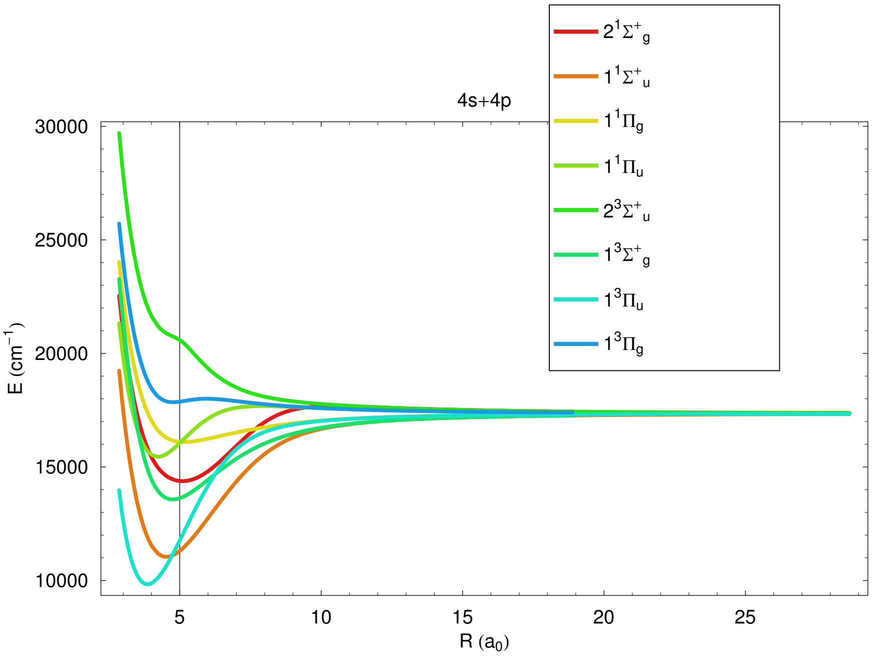

Figure 4.3: All of the potential energy surfaces dissociating to 4s+4p. [As provided in S. Magnier *et al.*, J. Chem. Phys. **121**, 1771 (2004).]

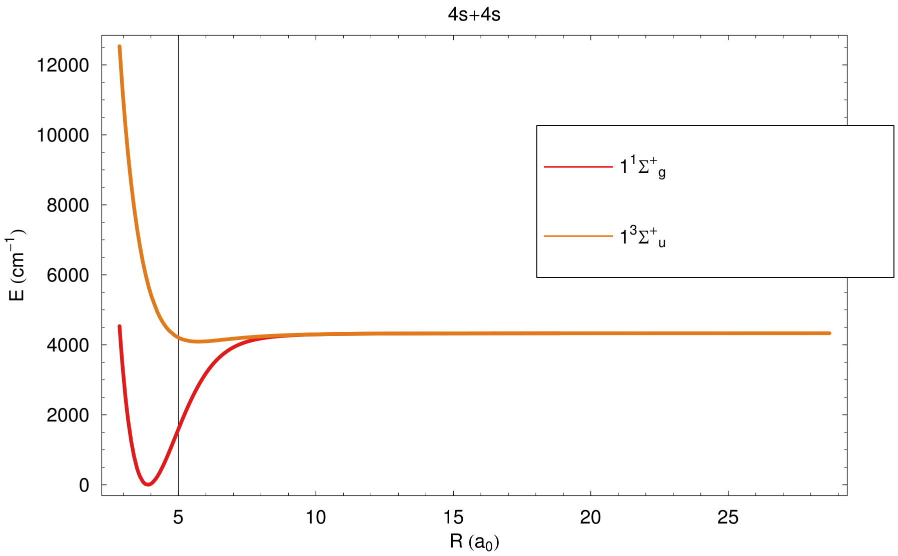

Figure 4.4: All of the ground state potential energy surfaces. [As provided in S. Magnier *et al.*, J. Chem. Phys. **121**, 1771 (2004).]

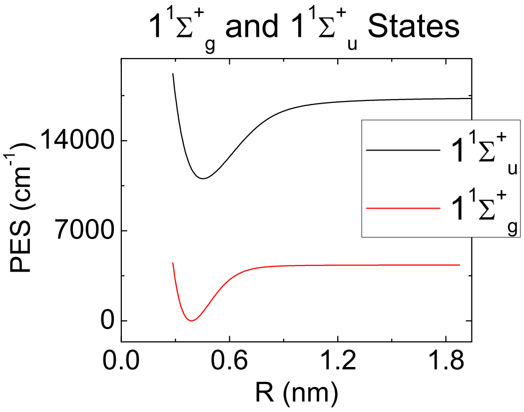

Figure 4.5: The PES whose difference was used to determine the resonant exciton couplings.

4.4 Diagonalizing the Exciton Hamiltonian

By diagonalizing the exciton Hamiltonian we obtained the one-exciton states used to calculate the frequency fluctuations $\delta\omega_i = \Omega - H_S[i]$, where i denotes the ith diagonal one-exciton matrix element [60]. To attempt proper bookkeeping,

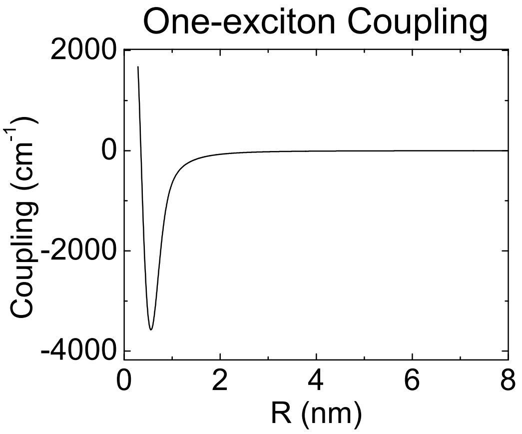

Figure 4.6: The difference between the $1^1\Sigma_u^+$ excited state potential energy surface and the $1^1\Sigma_g^+$ ground state surface, used to determine the resonant exciton couplings.

the eigenvalues and associated eigenvectors for each snapshot were compared with those of the previous snapshot. If any element of the eigenvectors was found to have changed by an amount greater than $\epsilon = 0.3$ cm^{-1}, the eigenvectors were reordered to minimize the number of elements that underwent such change. Although this removed most misorderings that masqueraded as avoided crossings, there were some "real" avoided crossings within eigenvectors that could not be reconciled frame-to-frame. In experiment only fluctuations within the laser bandwidth (~ 200 cm^{-1}) contribute to the response; a survey of the range of exciton energies revealed that most interactions stay within the laser bandwidth, representing the fact that the majority of collisions occur beyond the range of the most attractive or repulsive parts of the potential energy surfaces.

4.5 The Correlation Functions and Peak Shifts

The correlation functions were calculated for each run using the formula

$$C(\tau_j) = \frac{\langle \sum_{i=0}^{N} \delta\omega(t_i - \tau_j)\delta\omega(t_i) \rangle}{\langle \sum_{i=0}^{N} \delta\omega(t_i)\delta\omega(t_i) \rangle}, \tag{4.6}$$

where the brackets denote an ensemble average over all the one-exciton states and N is the number of frames in the trajectory. The fluctuations $\delta\omega$ are approximated to be periodic with period equal to t_N, and times only up to $\tau_{N/2}$ are considered in the final form of the correlation function. The resulting correlation functions, averaged over all runs for each of various temperatures and numbers of atoms, are plotted along with the experimental peak shift results in Figs. 4.7-4.8.

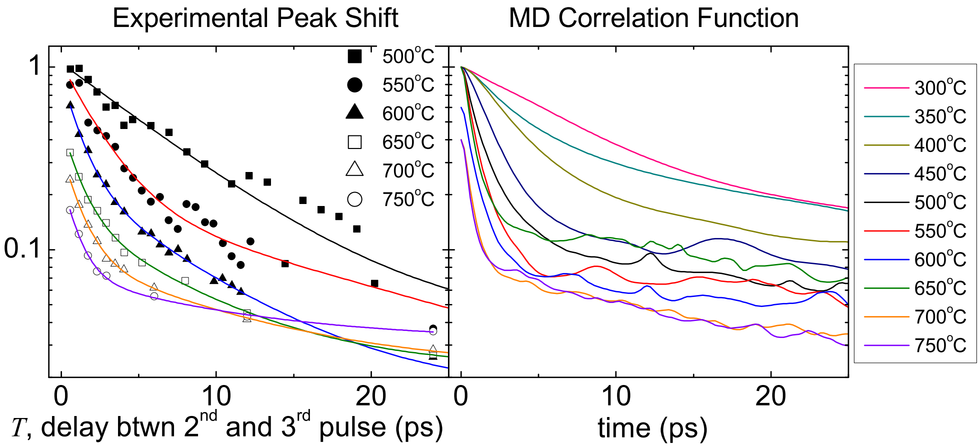

Figure 4.7: Experimental peak shifts (left) and theoretical correlation functions from molecular dynamics simulations with 20 atoms, averaged over 20 runs (right). The theoretical curves have been scaled to optimize their match with the experimental peak shifts.

In comparing the simulations with 10 atoms with the experimental results, good agreement is apparent. However, when the number of atoms is increased to

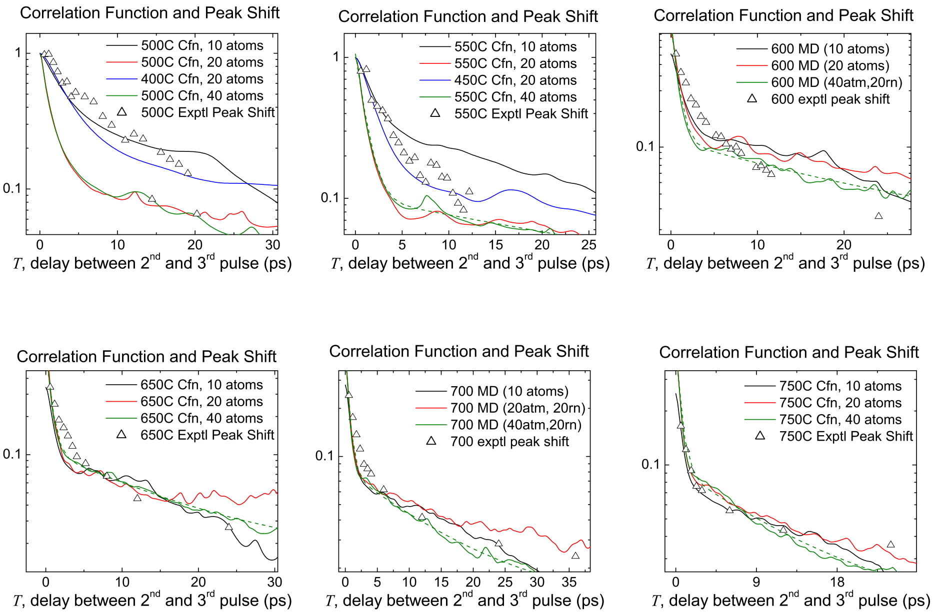

Figure 4.8: Experimental peak shifts (triangles) and correlation functions from molecular dynamics simulations with 10, 20 and 40 atoms (lines), scaled to optimize fit with experimental peak shifts.

20, the behavior is similar only when comparing with lower temperatures than those used in experiment. Simulations were performed for 40 atoms (as shown in Fig. 4.8) and were found to be similar to the 20 atom case; thus, the correlation functions can be considered to have converged with respect to the number of atoms by 20 atoms. Simulations were also performed for 2 atoms, resulting in correlation functions with much longer decay times, following the general trend seen in going from 10 to 20. These correlation functions did not match as well as the 10-atom case to the experimental peak shifts. The important features the simulation and experimental results have in common are the single-exponential to bi-exponential transition across temperature as well as the similar ratio of slow to fast exponential amplitudes with temperature.

To determine the source of the two exponential time constants in the cor-

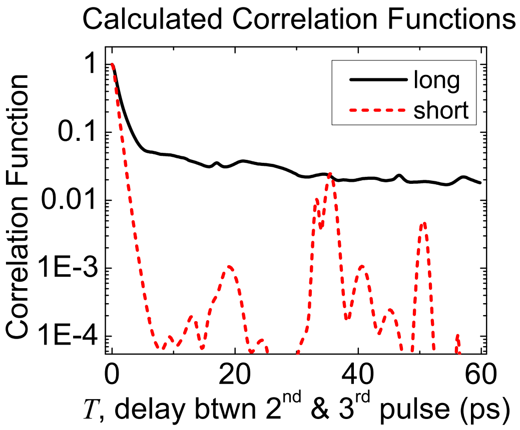

Figure 4.9: Correlation function from molecular dynamics simulation for potassium vapor at 500°C ($N \approx 3.4 \times 10^{17}$), with both short and long couplings.

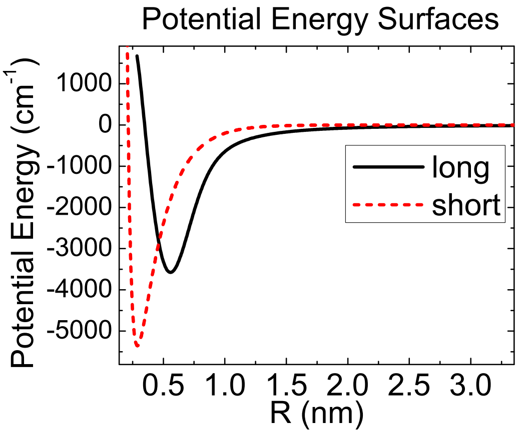

Figure 4.10: Potential energy surfaces used to compare short and long couplings.

relation function, we replaced the one-exciton potential energy surface with a shorter-range potential. This resulted in a single exponential decay, revealing that the slow decay is due to long-range, or resonant, interactions (see Figs. 4.9 and 4.10). In addition we used this surface to check whether the change in going from 10 to 20 atoms might be due to the box size being smaller than the range of the one-exciton PES. Using the short-range PES case, the box size was always much larger than the range of the PES. However, when the number of atoms was decreased to 10, the correlation function exhibited a slower exponential decay similar to that found when using the long one-exciton PES.

The correlation function temperature behavior does not agree as well with experiment when the number of atoms is increased, which may imply that the range of the potential is less than that represented by the potential energy surface used in the derivation. To check that the similar temperature behavior of the experimental peak shifts and the calculated correlation functions is real, the peak shifts were calculated using the correlation function parameters derived above within the theory of Ch. 2. There were thus four input parameters to the calculation corresponding to the Δ's and Λ's of the biexponential fits. Results are shown in Fig. 4.11. Only the correlation functions for 40 atoms were considered, but the most important aspect of the results is their similar behavior with the correlation functions used to calculate them, showing that bi-exponential correlation functions result in bi-exponential peak shifts. Thus the fast decaying part of the experimental peak shifts does seem to arise from the correlation functions.

The main assumptions made in the theoretical calculations are 1. using only ground-state atoms in the MD simulation and 2. the inclusion of only one of the eight dipole-allowed 4S+4P potential energy surfaces in calculating the exciton Hamiltonian (this also means we ignore the fine structure and hyperfine splitting). The first assumption means we do not take into account the fact that the experiment is sensitive only to the frequency fluctuations of excited atoms. The way to account for excited atoms would be to take for each snapshot the overlap integral between the exciton states for a system with all ground state atoms and the exciton states for a system with all atoms in ground except one in the excited state. In this way the evolution of the system as detected by experiment would be properly described. Concerning the second assumption, including all the po-

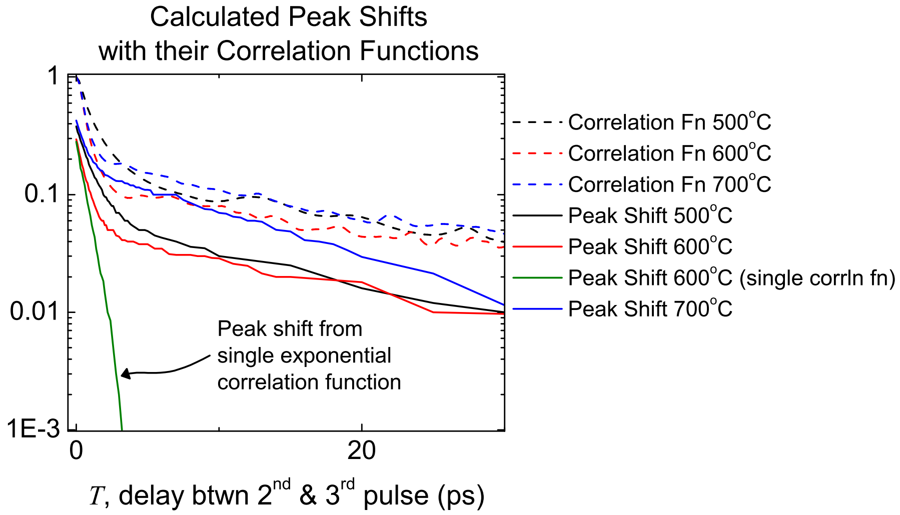

Figure 4.11: Calculated peak shifts and their correlation functions.

tential energy surfaces would change the characteristic timescales and amplitudes of fluctuations in some way. To actually include all the surfaces properly seems to be a challenging task that might not result in significant changes in behavior from a more qualitative approach, at least as a function of temperature and density.

To conclude, the above results show that peaks shifts based on correlation functions calculated from MD simulations in an exciton picture exhibit similar behavior as a function of temperature and density to experimental peak shifts. Our theoretical approach to modeling uses classical trajectories to result in remarkably realistic simulations of quantum dissipation. In addition, the behavior of the correlation functions versus temperature and density reveal the effects of resonance broadening at high densities and temperatures. This unusually simple electronic system has provided the opportunity to derive a correlation function from first principles with relatively few simplifications compared to molecular systems. This work has implications for other disordered excitonic systems such as molecular aggregates, semiconductors and biological systems.

Chapter 5

The Local Field

In 1880, Lorentz and Lorenz were both interested in the same problem: the connection between the index of refraction of a transparent body, and its density [63, 64, 65]. They found that for high-density materials the microscopic field plays a significant role in determining the index of refraction, which can be accounted for using the concept of a local field. Doing so reveals that the local field causes a redshift of the resonance lineshape called the Lorentz-Lorenz shift. It was not until a century later that the Lorentz-Lorenz shift was detected in experiment, using resonant selective reflection in a dense potassium vapor [66]. The study revealed a greater frequency shift than that predicted by the Lorentz and Lorenz, which was attributed to collisional contributions. Later work disagreed with this explanation of the extra shift [67, 68, 69]. In order to reduce the influence of additional frequency shifts we work in the time domain using transient four-wave mixing (TFWM). The results of the TFWM experiment reveal a clear local field contribution. In this chapter the influence of the local field will be derived for the frequency domain and time domain, followed by experimental TFWM results and a preliminary calculation of the propagated local field in a dense potassium vapor.

5.1 Definition of the Local Field

When an electromagnetic field is incident on a material system, a typical atom of the system experiences not only the externally applied field but also a microscopic field due to the induced polarization of the surrounding atoms in the material. The effective, or local, field is the sum of the external and internal fields incident on a typical atom in the ensemble, represented as $\mathbf{E}_{loc} = \mathbf{E}_{Max} + \mathbf{E}_{int}$, where $\mathbf{E}_{Max}$ is the macroscopic field determined by the Maxwell equations and $\mathbf{E}_{int}$ is the internal field from the induced polarization of the surrounding atoms. In order to count the field contributions of nearby atoms only once, we define the internal field as the difference between the nearby field calculated through a detailed microscopic treatment and that calculated from the macroscopic polarization P. Thus $\mathbf{E}_{int} = \mathbf{E}_{mic} - \mathbf{E}_{\mathbf{P}}$, where $\mathbf{E}_{mic}$ is the microscopic contribution of nearby atoms and $\mathbf{E}_{\mathbf{P}}$ is the field from these same surrounding atoms calculated from the macroscopic polarization $\mathbf{P}$ of the medium. In this way we replace the macroscopic field by the internal field that properly takes nearby contributions into account. The range over which nearby atoms must be considered can be approximated as a sphere whose radius is large enough to encompass atoms whose configuration and locations result in fields that cannot be averaged out, and large enough such that the polarization resulting from the atomic dipoles can be considered evenly distributed throughout the volume. For a random configuration of atoms the field due to atoms inside the sphere, E_{mic}, is zero [70], resulting in the internal field $\mathbf{E}_{int} = -\mathbf{E}_{\mathbf{P}}$. The macroscopic field is the same as that from a sphere with radius R containing a charge distribution with total dipole moment $\mathbf{p} = \frac{4\pi R^3}{3}\mathbf{P}$: $\mathbf{E}_{\mathbf{P}} = -L\mathbf{P}$ [70], where $L = \frac{1}{3\epsilon_0}$ (SI units), called the Lorentz constant. Thus in the end the total field amounts to the Maxwell field minus the internal field calculated using the macroscopic polarization,

$$\mathbf{E}_{loc} = \mathbf{E}_{Max} - L\mathbf{P}, \tag{5.1}$$

hence the referencing of this treatment as a "mean-field" approach.

5.2 Frequency-Domain Manifestation of the Local Field

The local field is manifested in frequency-domain experiments as a redshift of the resonance line center. This can be derived starting from the definition of the polarization $\mathbf{P}(\omega) = \chi(\omega)\mathbf{E}(\omega)$, with the local field $\mathbf{E}(\omega) = E_{Max}(\omega) + L\mathbf{P}(\omega)$:

$$\mathbf{P}(\omega) = \chi(\omega)[\mathbf{E}_{Max}(\omega) + L\mathbf{P}(\omega)]. \tag{5.2}$$

Solving for $\mathbf{P}$, we find,

$$\mathbf{P}(\omega) = \frac{\chi(\omega)}{1 - L\chi(\omega)}\mathbf{E}_{Max}(\omega). \tag{5.3}$$

Now substituting this into the equation for the total field $\mathbf{E}(\omega)$ we find

$$\mathbf{E}(\omega) = \mathbf{E}_{Max}(\omega) + \frac{L\chi(\omega)}{1 - L\chi(\omega)}\mathbf{E}_{Max}(\omega) = \frac{\mathbf{E}_{Max}(\omega)}{1 - L\chi(\omega)} \tag{5.4}$$

Using the definition of χ for a two-level atomic system with resonance frequency ω_0 and population decay rate γ gives

$$\begin{aligned}\frac{1}{1 - L\chi(\omega)} &= \frac{1}{1 - \frac{LA}{\omega_0^2 - \omega^2 - i\omega\gamma}} = \frac{\omega_0^2 - \omega^2 - i\omega\gamma}{(\omega_0^2 - LA) - \omega^2 - i\omega\gamma} \\ &= 1 + \frac{LA}{(\omega_0^2 - LA) - \omega^2 - i\omega\gamma},\end{aligned} \tag{5.5}$$

where A represents the strength of material response and is proportional to the dipole moment squared. It can be seen from the above equation that accounting for local field effects results in a redshift of the resonance frequency represented by the LA term in the denominator. The local field thus results in a modified definition of the dielectric constant ϵ of the material based on what is known as the Lorentz-Lorenz law:

$$\frac{\epsilon - 1}{\epsilon + 2} = \frac{4\pi}{3} N\alpha, \tag{5.6}$$

where N is the density of the material and α is the atomic polarizability[1] .

Maki *et al.* measured the reflectivity spectrum from the interface between a dense potassium vapor and the sapphire window of an atomic vapor cell to determine the resonant structure of the dielectric constant for both linear and nonlinear response. They worked at number densities high enough for local-field effects to be important [2] [66]. In a method known as selective reflection [71], they measured the highly wavelength-dependent reflectivity near the D resonance lines. The ratio of reflected intensity to incident intensity was measured as a function of the optical frequency. Their results reveal a shift greater than that predicted solely by the Lorentz-Lorenz shift, which they attribute to a collisional shift contribution. To rule out the modifications that may arise from atom-window interactions, they noted that the mean interatomic separation was much smaller than the penetration depth of light into the medium, meaning the number of atoms which interacted with the sapphire window was neglible compared to the number of atoms contributing to the measured response. They support the assumption of a collisional contribution by comparing the linear experimental results with non-linear experimental results that contain local field contributions to higher order. The collisional contribution is difficult to theoretically affirm, however, and later papers have proposed other possible contributions beyond those due to collisions between potassium atoms [67, 68, 69, 56].

---

[1] This is also known as the Clausius-Mosotti relation for longer wavelengths.

[2] Later papers showed that the Lorentz-Lorenz shift cannot be ignored at lower densities, where inhomogeneous broadening dominates, either. [68, 67]

5.3 Time-Domain Manifestation of the Local Field

In 2-pulse TFWM the local field results in a signal for the "wrong delay." As was shown in the Ch. 3, the two-pulse TFWM signal from a 2-level system not including local field effects is zero for negative delays, that is, for delays in which the conjugate pulse arrives last. Here we derive the nonlinear time-domain response for a 2-level system including local field effects. We will see that the local field allows a breaking of the "proper" time ordering, resulting in a signal for negative delay [72].

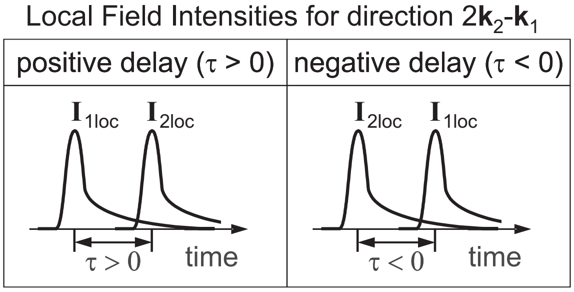

Figure 5.1: Schematic of local field intensities interacting in a 2-pulse TFWM experiment for the signal in direction $2\mathbf{k}_2 - \mathbf{k}_1$. Including local field effects, for $\tau < 0$ the tail of $\mathbf{I}_{2loc}$ can act after $\mathbf{I}_{1loc}$ to create a signal for negative delay.

To derive the time-domain response we use the local field defined above as the incident field of the optical Bloch equations. Note that $\mathbf{P}$ depends on the off-diagonal matrix elements ρ_{nm}, meaning there will arise a recursive relationship in the optical Bloch equations that represents the polarization acting on itself. This results in a negative delay signal due to the decaying tail of the induced polarization interacting with the next pulse such that signals for both time orderings are allowed (see Fig. 5.1). Using the local field we have for the coherence at third order:

$$\dot{\rho}^{(3)}_{mn}(t) = \frac{-iLN\mu^2_{nm}}{\hbar}[\rho^{(2)}_{mm}(t)\rho^{(1)}_{mn}(t) + \rho^{(1)}_{mm}(t)\rho^{(2)}_{mn}(t)$$
$$-\rho^{(2)}_{mn}(t)\rho^{(1)}_{nn}(t) - \rho^{(1)}_{mn}(t)\rho^{(2)}_{nn}(t)] + \big[i(\omega - \omega_{nm}) - \gamma_{nm} + \frac{iLN\mu^2_{nm}}{\hbar}\big]\rho^{(3)}_{mn}(t)$$
$$+\frac{iLN\mu_{nm}}{2\hbar}[\rho^{(2)}_{mm}(t) - \rho^{(2)}_{nn}(t)]\mathbf{E}_{Max}(\mathbf{r}, t) \tag{5.7}$$

As seen in the above equation, the coherence at third order depends directly on the coherence at first order, representing the recursive relationship of the polarization acting on itself. This result is unlike that of the derivation which did not include local field effects, in which the third-order coherence equation of motion Eq. 2.9 was only directly dependent on the current and penultimate order. The results of this derivation calculated for delta function pulses are shown in Fig. 5.2. A negative delay signal appears when the local field is included. The decay rate for negative delay is faster than that for positive delay by a factor of 2, which arises from the convolution of the free polarization decay at first order with that at third order. The ratio of the signal amplitude for positive and negative delay is directly related to the Lorentz-Lorenz shift according to $B/A = [\Delta\omega_L/\gamma]^2$, where A (B) is the amplitude of the signal at $\tau = 0$ when extrapolated from positive (negative) delay and $\Delta\omega_L = \mu^2 NL/\hbar$ is the Lorentz-Lorenz shift. Thus the shift $\Delta\omega_L = \gamma \times \sqrt{B/A}$ can be extracted directly from experimental TFWM data. The original theory derived above predicts a value for the Lorentz constant of $L = 1/3\epsilon_0$. It should be noted that in the derivation resulting in the above equation we have ignored a dependence on $\rho^{(1)*}_{mn}$ at second order; in addition, the treatment may be improved through a more thorough inclusion of the recursive relationship of the local field on the polarization for each order.

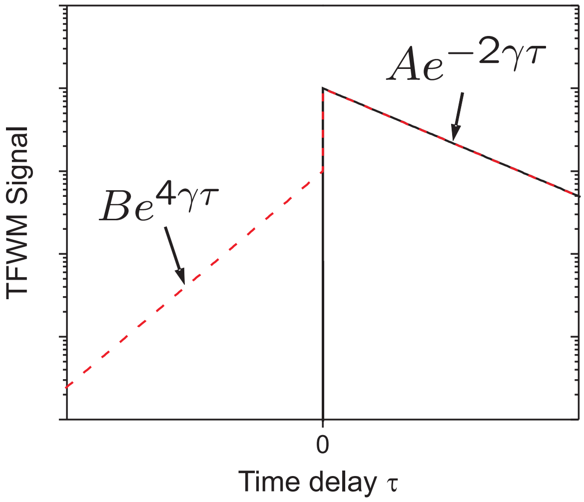

Figure 5.2: Calculated 2-pulse TFWM signal for a 2-level system with (dashed) and without (solid) local field.

5.4 Transient Four-Wave Mixing Experimental Results

A representative 2-pulse TFWM signal from the experiment described in Ch. 3 is now shown in full including negative time delay in Fig. 5.3. Although the ratio of the decay rate for positive and negative delay agree with theory, we find the strength of the local field contribution L as determined by fitting the signal amplitudes for negative and positive delay B/A to be less than predicted by a factor of 20. This discrepancy could have a number of causes. Radiation trapping was one candidate considered, but using the pulse picker to decrease the repetition rate did not significantly modify the amplitude ratio. Excitation-induced effects (often revealed by a decreasing dephasing rate with increasing excited state population) was also considered [73], and indeed decreasing the incident intensity resulted in a larger local field effect, but still did not make a great enough difference to match with theory. It has been noted that at the depth at which these experiments probe, the local field is not yet fully formed [56], which would support a decreased shift. In addition, the opposite limit in which the fields penetrate further into the vapor and are influenced by propagation effects is not included in the theoretical treatment. To test whether the discrepancy is due either to an incompletely formed local field or propagation effects, we performed some preliminary calculations of pulse fields reflected from and transmitted through a dense atomic vapor, including local field effects. These calculations are briefly summarized below.

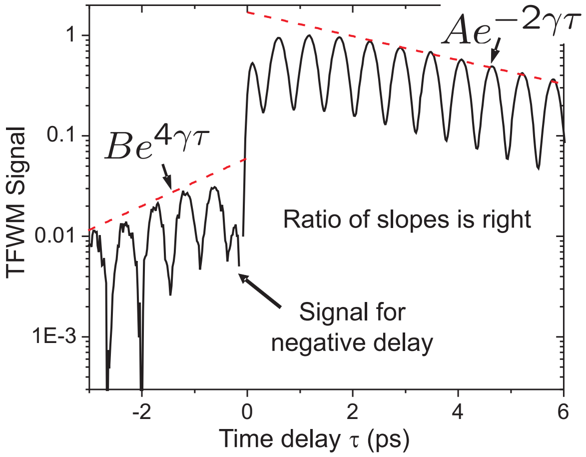

Figure 5.3: Experimental 2-pulse TFWM signal for a 2-level system, with slopes labeled.

5.5 Preliminary Calculations of Propagation

This section presents a calculation of pulse fields reflected from and transmitted through a dense atomic vapor, including local field effects. The structure under consideration is shown in Fig. 5.4. This treatment is based on the formalism of Sipe [74] and to this point only includes the linear response.

We use the following equations for the reflected ($E^{+}_{refl}(z,t)$) and transmitted ($E^{+}_{trans}(z,t)$) fields:

$$E^{+}_{refl}(z,t) = \int_0^\infty \frac{d\omega}{2\pi}\left[\frac{n_1 - n_2(\omega)}{n_1 + n_2(\omega)}\right] E_{-}(\omega) e^{-i\omega(t - n_1 z/c)} \tag{5.8}$$

and

$$E^{+}_{trans}(z,t) = \int_0^\infty \frac{d\omega}{2\pi}\left[\frac{2n_1}{n_1 + n_2(\omega)}\right] E_{-}(\omega) e^{-i\tilde{\omega} n_2(\omega) z} e^{-i\omega t} \tag{5.9}$$

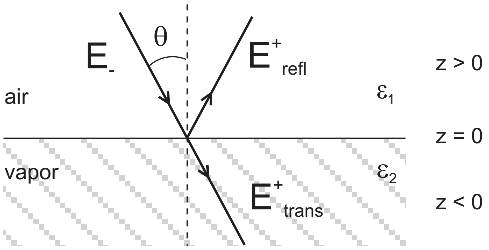

Figure 5.4: Structure considered for the propagation calculations. In the calculations θ is set to zero (normal incidence).

where $\tilde{\omega} = \omega/c$, and

$$E_-(\omega) = e^{-(\omega-\omega_0)^2/\Delta^2} \tag{5.10}$$

is the incident field for $\omega > 0$ and $\Delta << \omega_0$.

The index of refraction of the vapor, $n_2(\omega)$ (see Fig. 5.5), is defined to be $n_2(\omega) = \sqrt{\epsilon(\omega)}$, where

$$\epsilon(\omega) = 1 + \chi(\omega) = 1 + \frac{e^2 f N/\epsilon_0 m}{(\bar{\omega}_{21}^2 + \gamma_{p12}^2) - \omega^2 - 2i\omega\gamma_{p12}} \tag{5.11}$$

Here $\bar{\omega}_{21} = \sqrt{\omega_{21}^2 - e^2 f N L/\epsilon_0 m}$.

Note in these calculations ω is in units of rad/sec, ν in units of 1/s. Below is a list of parameter values used in the calculations:

- laser center frequency is on resonance: $\nu_{laser} = \nu_0 = 3.9 \times 10^{14}$ 1/s
- laser pulse FWHM $\delta\nu = 1.02 \times 10^{13}$ 1/s, which corresponds to $\delta\lambda = 20$ nm (see Fig. 5.6)
- oscillator strength $f = 1$
- index of refraction of "air" $n_1 = 1$
- local field parameter $L = 1/3$
- density $N = 3.7 \times 10^{23}$ m^{-3} (corresponds to temperature $T = 700$°C)

- dephasing rate $\gamma_{p12} = 1.16 \times 10^{12}$ 1/s.

Note the index of refraction of the vapor is determined with the parameters f, L, N, and γ_{p12}, but the resulting amplitude of the real and imaginary parts are not consistent with experiment. In particular, the calculated index of refraction is only a little above 1 at 700°C, compared to ~ 6 in experiment. This means that in these results the fields are modified by the vapor resonance less strongly than in experiment. The figures that follow are largely self-explanatory.

The results for the transmitted field shown in Figs. 5.8 and 5.9 exhibit the well-known signature of propagation effects in the form of Bessel-function behavior, sometimes referred to as dynamic beating [12]. Experimental results measuring the linear response through upconverted reflected pulses show no sign of dynamic beating, implying that propagation effects are not an issue in the reflected TFWM signals. This result in turn means the signatures of non-Markovian dynamics are properly assigned and are not being confused with propagation effects. Experimental results in transmission using a 14 μm-thick transmission cell on the other hand exhibit pronounced dynamic beating, as shown in App. E. These calculations of propagation effects can in turn be used to model the development of local field effects in the nonlinear response of dense vapors as a function of penetration depth and density.

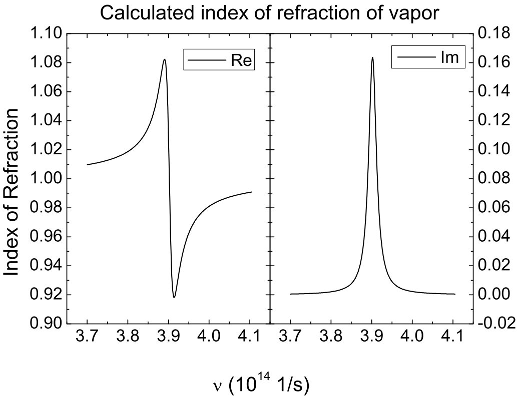

Figure 5.5: Index of refraction of vapor, real (left) and imaginary (right) parts.

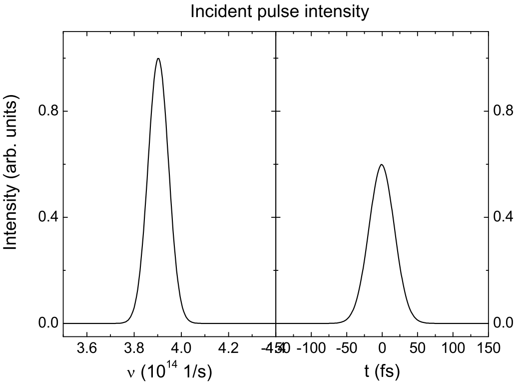

Figure 5.6: Incident pulse versus frequency (left) and time (right).

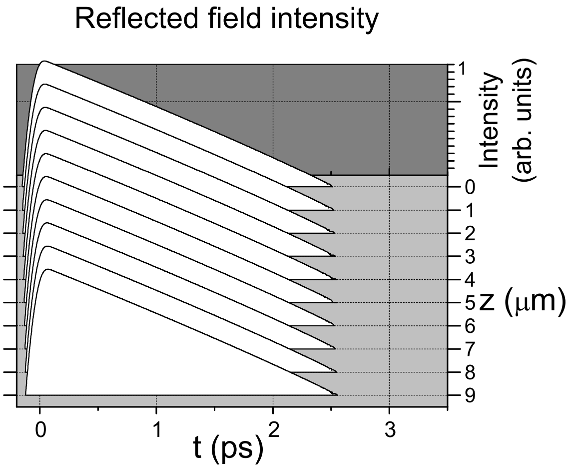

Figure 5.7: Reflected field intensity $|E^{+}_{refl}(z,t)|^2$.

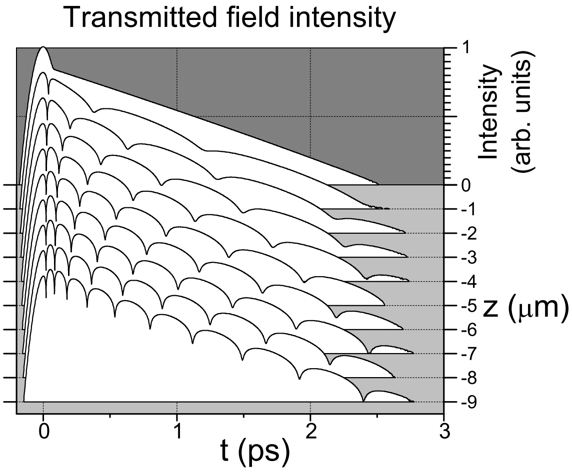

Figure 5.8: Transmitted field intensity $|E^{+}_{trans}(z,t)|^2$.

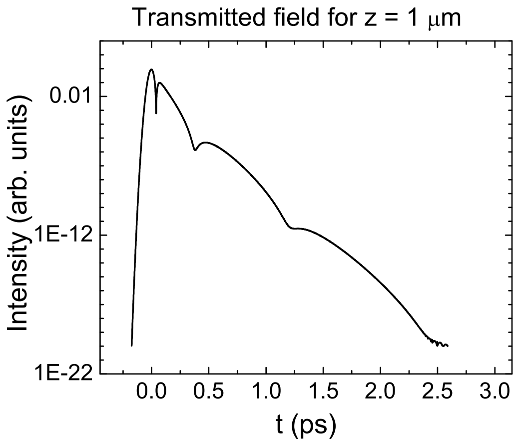

Figure 5.9: Transmitted field intensity $|E^{+}_{trans}(z,t)|^2$ for $z = 1$ μm.

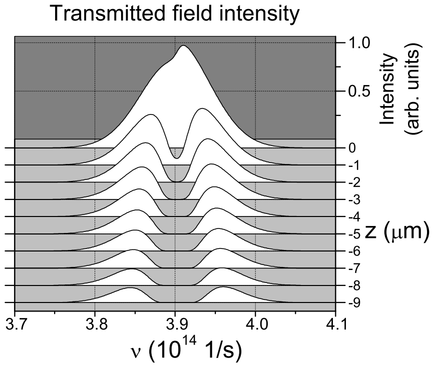

Figure 5.10: Transmitted field intensity versus frequency $|E^{+}_{trans}(z,\nu)|^2$.

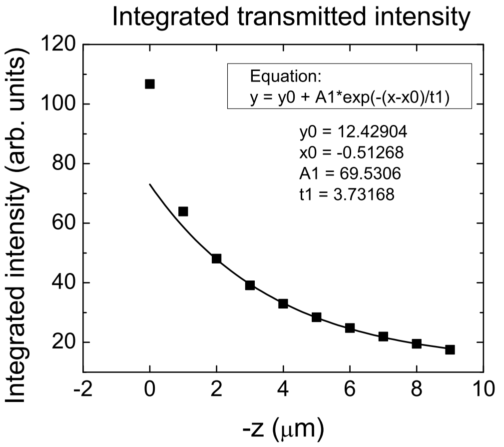

Figure 5.11: Integrated transmitted intensity $E^{+}_{trans}(z) = \int_0^\infty |E^{+}_{trans}(z,t)|^2 dt$. Follows Beer's law (exponential, line in figure) beyond 2μm.

Chapter 6

Conclusion

In this thesis we have presented results from 2- and 3-pulse transient four-wave mixing experiments and theoretical calculations of the material response. In Ch. 2 we derived the material response of a two- and three-level system to find that Markovian dynamics results in exponential dephasing, while non-Markovian dephasing is distinctly non-exponential and can be modeled based on an assumed two-time correlation function of frequency fluctuations. Chapter 3 on the photon echo experiments revealed distinct regimes of non-Markovian and Markovian dynamics in two- and three-pulse photon echo. The non-Markovian theory covered in Ch. 2 results in excellent fits for the two-pulse data, but the three-pulse peak shift data for high temperatures and densities exhibits bi-exponential behavior that cannot be modeled with a single exponential correlation function. In addition, time-resolved three-pulse data reveal clear photon echo-like behavior. To improve our understanding of the three-pulse experimental results, in Ch. 4 we presented a derivation of the correlation function of frequency fluctuations in an exciton picture from molecular dynamics simulations. The resulting calculated peak shifts exhibit bi-exponential behavior and reveal that the source of the slow component is the long-range interaction due to resonance broadening. The last chapter, Ch. 5, described the frequency- and time-domain signatures of the local field and presented experimental results with clear local field contributions.

A preliminary calculation of propagation effects was also presented that confirm that the experimental signals in reflection are not altered by propagation effects.

In summary, transient four-wave mixing experiments in a dense potassium vapor, which has the unusual quality of a long dephasing time compared to the collision duration, reveal distinct signatures of quantum dissipation in the form of both non-Markovian and Markovian dynamics. These results serve as a basis for understanding more complex systems such as molecular liquids due to the excellent agreement between the two-pulse experiments and theory assuming the stochastic correlation function. In addition, calculated correlation functions reveal that resonance effects may be the cause of the bi-exponential behavior observed in three-pulse photon echo peak shift experiments, giving insight into the dynamics of resonance-broadened vapors and disordered excitonic systems in general. Finally, the utility of time-domain techniques in the study of dense atomic vapors was supported throughout this research by the clear experimental signatures representing system response, both for non-Markovian dynamics and the local field effect.

We end by considering other avenues for contribution that could be explored in the future. A systematic study of the TFWM signals as a function of buffer gas density and temperature would yield insight into the difference between foreign-gas broadening and self-broadening. In conjunction with further theoretical molecular dynamics simulations we could gain a fundamental picture of the range of interactions in dense vapors. Once transmission cells (mentioned in App. E) are manufactured with a thickness on the order of a wavelength, transmission experiments can explore the transition from purely local field effects to propagation effects. In addition, with transmission cells dense vapors could then be studied with two-dimensional Fourier transform spectroscopy, which would enable the direct identification of excitonic effects, once again exhibiting signatures with unusual clarity due to the simplicity of the atomic system.

Finally, we acknowledge the support of the NSF JILA Physics Frontier Center for the duration of the research presented in this thesis.

Bibliography

[1] P. Hänggi and G.-L. Ingold, "Fundamental aspects of quantum Brownian motion," Chaos **15**, (2005).

[2] H. Margenau and W. W. Watson, "Pressure Effects on Spectral Lines," Rev. Mod. Phys. **8**, 2253 (1936).

[3] J. F. Ward, *Correlation effects in the theory of combined doppler and pressure broadening* (Thesis, University of Colorado, Boulder, 1964).

[4] J. Cooper, "Broadening of Isolated Lines in the Impact Approximation Using a Density Matrix Formulation," Rev. Mod. Phys. **39**, 167 (1967).

[5] J. H. V. Vleck and D. L. Huber, "Absorption, emission and linebreadths: A semihistorical perspective," Rev. Mod. Phys. **49**, 939 (1977).

[6] K. Niemax, M. Movre and G. Pichler, "Near-wing asymmetries of the self-broadened first Rb and Cs resonance lines," J. Phys. B **12**, 3503 (1979).

[7] R. E. Walkup, A. Speilfiedel and D. E. Pritchard, "Observation of Non-Lorentzian Spectral Line Shapes in Na-Noble-Gas Systems," Phys. Rev. Lett. **45**, 986 (1980).

[8] Y. Prior and A. Ben-Reuven, "Nonimpact theory of four-wave mixing and intracollisional dynamics," Phys. Rev. A **33**, 2362 (1986).

[9] N. Asida, M. Rosenbluh and S. Mukamel, "Nonimpact degenerate four-wave mixing in Na perturbed by He," Phys. Rev. A **40**, 41234126 (1989).

[10] K. Niemax and G. Pichler, "New aspects in self-broadening of alkali resonance lines," J. Phys. B **8**, 179 (1975).

[11] A. Laubereau and W. Kaiser, "Vibrational dynamics of liquids and solids investigated by picosecond light pulses," Rev. Mod. Phys. **50**, (1978).

[12] O. Kinrot and Y. Prior, "Four-wave mixing in optically dense media," Phys. Rev. A **50**, R1999 (1994).

[13] M. Sargent, III, M. O. Scully, W. E. Lamb and Jr., *Laser Physics* (Perseus, Cambridge, Mass., 1974).

[14] F. Bloch, “Nuclear induction,” Phys. Rev. **70**, 460 (1946).

[15] S. Mukamel, “Nonimpact unified theory of four-wave mixing and two-photon processes,” Phys. Rev. A **28**, 3480 (1983).

[16] S. Mukamel, *Principles of Nonlinear Optical Spectroscopy* (Oxford University Press, New York, 1995).

[17] D. Abramavicius and S. Mukamel, “Quartic Interband Exciton Couplings in Pump-Probe Spectroscopy of Light Harvesting Complexes,” J. Phys. Chem. B **108**, 10295 (2004).

[18] C. J. Fecko, J. D. Eaves, J. J. Loparo, A. Tokmakoff and P. L. Geissler, “Ultrafast Hydrogen-Bond Dynamics in the Infrared Spectroscopy of Water,” Science **301**, 1698 (2003).

[19] J. Stenger, D. Madsen, P. Hamm, E. T. J. Nibbering and T. Elsaesser, “A Photon Echo Peak Shift Study of Liquid Water,” J. Phys. Chem. A **106**, 2341 (2002).

[20] G. R. Fleming and M. Cho, “Chromophore- solvent dynamics,” Annu. Rev. Phys. Chem. **47**, 109 (1996).

[21] R. Jimenez, G. R. Fleming, P. V. Kumar and M. Maroncelli, “Femtosecond solvation dynamics of water,” Nature **369**, 471 (1994).

[22] T. Joo, Y. Jia, J. Y. Yu, M. J. Lang, and G. R. Fleming, “Third-order nonlinear time domain probes of solvation dynamics,” J. Chem. Phys. **104**, 6089 (1996).

[23] E. T. J. Nibbering, D. A. Wiersma and K. Duppen, “Femtosecond Non-Markovian Optical Dynamics in Solution,” Phys. Rev. Lett. **66**, 2464 (1991).

[24] J. G. Fugimoto and T. K. Yee, “Diagrammatic Density Matrix Theory of Transient Four-Wave Mixing and the Measurement of Transient Phenomena,” IEEE J. Quantum Electron. **QE-22**, 8 (1986).

[25] J. A. Armstrong, N. Bloembergen, J. Ducuing and P. S. Pershan, “Interactions between Light Waves in a Nonlinear Dielectric,” Phys. Rev. **127**, 1918 (1962).

[26] A. Abragam, *Principles of Nuclear Magnetism* (Oxford Univerity Press, Oxford, 1961).

[27] T. Yajima and Y. Taira, “Spatial Optical Parametric Coupling of Picosecond Light Pulses and Transverse Relaxation Effect in Resonant Media,” J. Phys. Soc. Jpn. **47**, 1620 (1979).

[28] A. Papoulis, *Brownian Movement and Markoff Processes*, 2nd ed. (McGraw-Hill, New York, 1984).

[29] G. E. Uhlenbeck and L. S. Ornstein, “On the Theory of the Brownian Motion,” Phys. Rev. **36**, 823 (1930).

[30] J. L. Doob, “The Brownian Movement and Stochastic Equations,” Ann. Math. **43**, 351 (1942).

[31] S. Mukamel and R. F. Loring, “Nonlinear response function for time-domain and frequency-domain four-wave mixing,” J. Opt. Soc. Am. B **3**, 595 (1986).

[32] R. Kubo, in *Fluctuation Relaxation and Resonance in Magnetic Systems*, edited by D. Ter-Haar (Oliver and Boyd, Edinburgh, 1962).

[33] R. Kubo, “A Stochastic Theory of Line Shape,” Adv. Chem. Phys. **15**, 101 (1969).

[34] R. Zwanzig, “Ensemble Method in the Theory of Irreversibility,” J. Chem. Phys. **33**, 1338 (1960).

[35] R. Zwanzig, “Memory Effects in Irreversible Thermodynamics,” Phys. Rev. **124**, 983 (1961).

[36] R. Zwanzig, in *Lectures in Theoretical Physics*, edited by W. E. Brittin (Interscience, New York, 1961).

[37] U. Fano, “Pressure Broadening as a Prototype of Relaxation,” Phys. Rev. **131**, 259268 (1963).

[38] W. Magnus, Commun. Pure Appl. Math. **7**, (1954).

[39] R. M. Wilcox, “Exponential Operators and Parameter Differentiation in Quantum Physics,” J. Math. Phys. **4**, 962 (1967).

[40] U. Haeberlen, *Advances in Magnetic Resonance* (Academic Press, New York, 1976), suppl. I.

[41] K.-E. Süsse, W. Vogel and D.-G. Welsch, “Femtosecond photon echoes via non-Markovian dephasing,” Chem. Phys. Lett. **162**, 287 (1989).

[42] N. A. Kurnit, I. D. Abella and S. R. Hartmann, “Observation of a Photon Echo,” Phys. Rev. Lett. **13**, 567 (1964).

[43] M. Cho, J.-Y. Yu, T. Joo, Y. Nagasawa, S. A. Passino and G. R. Fleming, “The Integrated Photon Echo and Solvation Dynamics,” J. Phys. Chem. **100**, 11944 (1996).

[44] E. C. C. Baly, *Spectroscopy* (Longmans, Green and Co., New York, 1924).

[45] L. Tterlikkis, S. D. Mahanti, and T. P. Das, “Theoretical Analysis of the Hyperfine Structure of Alkali Atoms,” Phys. Rev. **176**, 10 (1968).

[46] O. D. Zakharova and A. M. Semenov, “The Pressures at Which the Properties of Vapors of Alkali Metals Correspond to the Model of Ideal Reacting Gas,” High Temperature **40**, 150 (2002).

[47] A. N. Nesmeyanov, *Vapor Pressure of the Chemical Elements* (Elsevier, London, 1963).

[48] A. Honold, L. Schultheis, J. Kuhl and C. W. Tu, “Reflected degenerate four-wave mixing on GaAs single quantum wells,” App. Phys. Lett. **52**, 2105 (1988).

[49] T. Holstein, “Imprisonment of Resonance Radiation in Gases II,” Phys. Rev. **83**, 1159 (1951).

[50] W. A. Hügel, M. F. Heinrich, M. Wegener, Q. T. Vu, L. Bányai and H. Haug, “Photon Echoes from Semiconductor Band- to-Band Continuum Transitions in the Regime of Coulomb Quantum Kinetics,” Phys. Rev. Lett. **83**, 3313 (1999).

[51] M. Aihara, “Non-Markovian theory of nonlinear- optical phenomena associated with the extremely fast relaxation in condensed matter,” Phys. Rev. B **25**, 53 (1982).

[52] J. P. Lavoine, A. J. Boeglin, P. Martin and A. A. Villaeys, “Non-Markovian effects on quantum beats,” Phys. Rev. B **53**, 11535 (1996).

[53] Y. J. Yan and S. Mukamel, “Photon echoes of polyatomic molecules in condensed phases,” J. Chem. Phys. **94**, 179 (1991).

[54] P. Hamm, M. Lim and R. M. Hochstrasser, “Non-Markovian Dynamics of the Vibrations of Ions in Water from Femtosecond Infrared Three-Pulse Photon Echoes,” Phys. Rev. Lett. **81**, 5326 (1998).

[55] V. O. Lorenz and S. T. Cundiff, “Non- Markovian Dynamics in a Dense Potassium Vapor,” Phys. Rev. Lett. **95**, 163601 (2005).

[56] J. A. Leegwater and S. Mukamel, “Self- broadening and exciton line shifts in gases: Beyond the local-field approximation,” Phys. Rev. A **49**, 146 (1994).

[57] D. A. Farrow, A. Yu and D. M. Jonas, “Spectral relaxation in pumpprobe transients,” J. Chem. Phys. **118**, 9348 (2003).

[58] J. A. Leegwater and S. Mukamel, “Semiclassical Green function calculation of four wave mixing in polarizable clusters and liquids,” J. Chem. Phys. **101**, 7388 (1994).

[59] S. Mukamel, “Multidimensional Femtosecond Correlation Spectroscopies of Electronic and Vibrational Excitations,” Annu. Rev. Phys. Chem. **51**, 691 (2000).

[60] S. Mukamel and D. Abramavicius, “Many- Body Approaches for Simulating Coherent Nonlinear Spectroscopies of Electronic and Vibrational Excitons,” Chem. Rev. **104**, 2073 (2004).

[61] D. van der Spoel, E. Lindahl, B. Hess, G. Groenhof, A. E. Mark and H. J. C. Berendsen, “GROMACS: Fast, flexible, and free,” J. Comp. Chem. **26**, 17011718 (2005).

[62] S. Magnier, M. Auber-Frécon and A. R. Allouche, “Theoretical determination of highly excited states of K_2 correlated adiabatically above $K(4p)+K(4p)$,” J. Chem. Phys. **121**, 1771 (2004).

[63] H. A. Lorentz, “Ueber die Beziehung zwischen der Fortpflanzungsgeschwindigkeit des Lichtes und der Körperdichte,” Ann. Phys. Chem. **9**, 641 (1880).

[64] L. Lorenz, “Ueber die Refractionsconstante,” Ann. Phys. Chem. **11**, 70 (1880).

[65] H. A. Lorentz, *The Theory of Electrons*, 2nd ed. (Dover, New York, 1952).

[66] J. J. Maki, M. S. Malcuit, J. E. Sipe and R. W. Boyd, “Linear and nonlinear optical measurements of the Lorentz local field,” Phys. Rev. Lett. **67**, 972 (1991).

[67] J. Guo, J. Cooper and A. Gallagher, “Selective reflection from a dense atomic vapor,” Phys. Rev. A **53**, 1130 (1996).

[68] J. Guo, A. Gallagher and J. Cooper, “Lorentz-Lorenz shift in an inhomogeneously broadened medium,” Opt. Comm. **131**, 219 (1996).

[69] P. Wang, A. Gallagher and J. Cooper, “Selective reflection by Rb,” Phys. Rev. A **56**, 1598 (1997).

[70] J. D. Jackson, *Classical Electrodynamics*, 2nd ed. (Wiley, New York, 1975), chap. 4.

[71] J. P. Woerdman and M. F. H. Schuurmans, “Spectral narrowing of selective reflection from sodium vapour,” Opt. Comm. **14**, (1975).

[72] S. T. Cundiff, “Time domain observation of the Lorentz-local field,” Laser Phys. **12**, 1073 (2002).

[73] J. M. Shacklette and S. T. Cundiff, “Role of excitation-induced shift in the coherent optical response of semiconductors,” Phys. Rev. B **66**, 045309 (2002).

[74] J. E. Sipe, “New Green function formalism for surface optics,” J. Opt. Soc. Am. B **4**, 481 (1987).

[75] S. Y. Yee and T. K. Gustafson, “Diagrammatic analysis of the density operator for nonlinear optical calculations: Pulsed and CW responses,” Phys. Rev. A **18**, 1597 (1978).

[76] R. W. Boyd, *Nonlinear Optics*, 2nd ed. (Academic Press, New York, 2003).

[77] N. B. Vargaftik, *Handbook of Physical Properties of Liquids and Gases: pure substances and mixtures*, 2nd ed. (Hemisphere, Washington, 1975).

[78] D. S. Hughes and P. E. Lloyd, “Pressure Effects of Homogeneous K Vapor in Absorption,” Phys. Rev. **52**, 1215 (1937).

Appendix A

Optical Bloch Equations Derivation Details

This appendix contains details for the derivation of the optical Bloch equations for a two-level system.

Starting from Eq. 2.10, we have

$$\rho_{nm}^{(q)}(t) = -\frac{i}{\hbar}\int_{-\infty}^{t} dt' e^{(i\omega_{nm}+\gamma_{nm})(t'-t)}[-\mu\cdot\mathbf{E}(t'), \rho^{(q-1)}]_{nm}. \tag{A.1}$$

To third order we then have

$$\begin{aligned}\rho_{ba}^{(3)}(t) = {}& -2i\rho^{(0)}\big(\frac{\mu_{ba}}{\hbar}\big)^3 \exp[-(i\omega_{ba}+\frac{1}{T_2})]\int_{-\infty}^{t} dt' \int_{-\infty}^{t'} dt'' \int_{-\infty}^{t''} dt''' \\ & \mathbf{E}(\mathbf{r},t')\mathbf{E}(\mathbf{r},t'')\mathbf{E}(\mathbf{r},t''')\exp[\gamma(t'-t'')+t'''/T_2] \\ & \times\{\exp[i\omega_{ba}(t'-t''+t''')]+\exp[-i\omega_{ba}(t'+t''-t''')]\},\end{aligned} \tag{A.2}$$

where $\gamma = \frac{1}{T_2}-\frac{1}{T_1}$, $\mu_{ab}=\mu_{ba}$ and the population was assumed to start in the ground state, $\rho_D^{(0)}=\rho^{(0)}$, $\rho_{ba}^{(0)}=0$.

Now if we write the fields as $\mathbf{E}_i(\mathbf{r},t) = E_i(t)\exp[-i\omega t + i\mathbf{k}_i\cdot\mathbf{r}] + \text{c.c.}$ then we can separate the term in direction $\mathbf{k}_4 = 2\mathbf{k}_2 - \mathbf{k}_1$ and make the rotating wave approximation in which we ignore terms with sums of frequencies $\omega_{ba}+\omega$ and $-\omega_{ba}-\omega$. We have

$$\begin{aligned}\rho_{ba}^{(3)}(t) = {}& -2i\rho^{(0)}\big(\mu_{ba}/\hbar\big)^3\exp\big[-\big(\frac{1}{T_2}+i\omega_{ba}\big)t+i\mathbf{k}_4\cdot\mathbf{r}\big]\int_{-\infty}^{t}\int_{-\infty}^{t'}\int_{-\infty}^{t''} dt'dt''dt''' \\ & \exp\big[\gamma(t'-t'')+\frac{t'''}{T_2}\big]\big\{E_2(t')E_2(t'')E_1^*(t''')\exp[i\Delta\omega(t'+t''-t''')] \\ & +E_2(t')E_1^*(t'')E_2(t''')\exp[i\Delta\omega(t'-t''+t''')]\big\},\end{aligned} \tag{A.3}$$

where $\Delta\omega = \omega_{ba} - \omega$. This is equivalent to Eq. 2.14.

Now we let the field envelopes be delta-function pulses, defined by $E_i(t) = \delta(t - t_i)$:

$$\begin{aligned}\rho_{ba}^{(3)}(t) = -2i\rho^{(0)}\big(\frac{\mu_{ba}}{\hbar}\big)^3 \\ \exp[i\mathbf{k}_4 \cdot \mathbf{r} - \frac{1}{T_2}(t - t_1)] \exp[-i\omega_{ba}t + i\Delta\omega(2t_2 - t_1)]\theta(t - t_2)\end{aligned} \tag{A.4}$$

where we have used the definition

$$\int_{-\infty}^{x} \delta(t - y)f(t)dt = \int_{-\infty}^{x-y} \delta(t)f(t + y)dt = f(y)\theta(x - y), \tag{A.5}$$

where $\theta(t)$ is the Heaviside step function, $\theta(t) = 0$ for $t < 0$, $\theta(t) = 1/2$ for $t = 0$, $\theta(t) = 1$ for $t > 0$. Now if we consider pulses with center frequency on resonance, $\omega = \omega_{ba}$, and use the definition $\hat{\mathbf{P}}^{(3)} = N\mu_{ba}\hat{\rho}_{ba}^{(3)}(\mathbf{r}, t, \omega_0)$ we find

$$\hat{\mathbf{P}}^{(3)}(\mathbf{r}, t) = -i\rho^{(0)}CN\mu_{ba}\theta(t - t_2)\exp[i\mathbf{k}_4 \cdot \mathbf{r} - T_2^{-1}(t - t_1)] \tag{A.6}$$

which is Eq. 2.16.

Appendix B

Non-Markovian Theory Derivation Details

B.1 Density Matrix Diagrams

All of the relevant diagrams contributing to the response of a three-level system in 3-pulse TFWM in direction $-\mathbf{k}_1 + \mathbf{k}_2 + \mathbf{k}_3$ are shown in Fig. B.1.

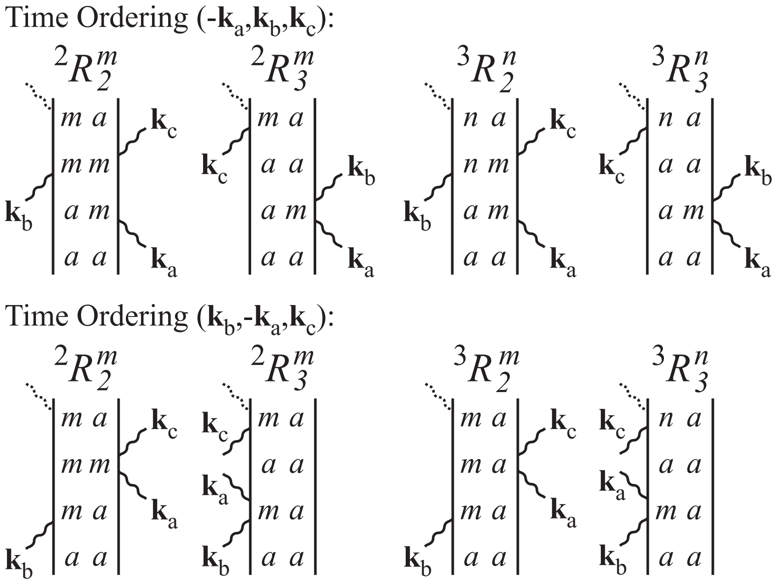

Figure B.1: Double-sided Feynman diagrams representing the relevant pathways for 3-pulse TFWM in a 3-level system in direction $-\mathbf{k}_1 + \mathbf{k}_2 + \mathbf{k}_3$ for all time orderings, with $n, m = b, c; n \neq m$. Orderings $(-\mathbf{k}_1, \mathbf{k}_3, \mathbf{k}_2)$ and $(\mathbf{k}_3, -\mathbf{k}_1, \mathbf{k}_2)$ are the same as for $(-\mathbf{k}_1, \mathbf{k}_2, \mathbf{k}_3)$ and $(\mathbf{k}_2, -\mathbf{k}_1, \mathbf{k}_3)$, with 3 and 2 switched, while orderings $(\mathbf{k}_2, \mathbf{k}_3, -\mathbf{k}_1)$ and $(\mathbf{k}_3, \mathbf{k}_2, -\mathbf{k}_1)$ have no diagrams.

Each diagram in Fig. B.1 is a unique pictorial representation of one of the third-order density matrix terms [24]. These diagrams are called double-sided

Feynman diagrams because their representation of density matrix perturbations is similar to that provided by Feynman diagrams used to determine perturbations on wavefunctions [75]. The left-hand side of each diagram indicates the time-evolution of $|\psi\rangle$ and the right-hand side indicates the time evolution of $\langle\psi|$, with time increasing vertically upward [76]. The incident fields are represented by wavy lines labeled by the wavevector number of the field. Each interaction of the applied field with the material system is indicated by a vertex of a wavy line (the field) with a straight vertical line (the ket or bra component of the density matrix). The letters before and after the vertex represent the density matrix state of the system before and after the interaction. From these diagrams we can write the mathematical solution for $\rho^{(3)}$ by using the appropriate set of translation rules.

Double-sided Feynman diagrams give us the ability to form both a mathematical and physical description of a TFWM process. Reading off of the diagram labeled ${}^{2}R_{3}^{m}$ for time ordering $(-\mathbf{k}_a, \mathbf{k}_b, \mathbf{k}_c)$ in Fig. B.1, we see that the system begins in the ground state, which corresponds to the zeroth-order density matrix element $\rho_{aa}^{(0)}$. The first pulse, $-\mathbf{k}_a$, interacts with the material system to induce a polarization represented mathematically by $\rho_{am}^{(1)}$. This intermediate density matrix state is off-diagonal and dephases in time T_2. This diagram corresponds to the convolution integral over t_1. At a subsequent time t_2, the second field $\mathbf{E}_2^*$ forms a ground state population represented by $\rho_{aa}^{(2)}$, correponding to the convolution integral over t_2. Finally, at a time t_3, the third pulse $\mathbf{k}_c$ interacts with the system to produce a polarization in the direction $\mathbf{k}_4 = \mathbf{k}_1 - \mathbf{k}_2 + \mathbf{k}_3$ represented by $\rho_{ma}^{(3)}$. This polarization, according to the definition of Eq. 2.11, is $\mathbf{P}^{(3)} = N(\langle a|\mu|m\rangle\rho_{ma}^{(3)} + c.c.)$. The other diagrams in Fig. B.1 can be read in a similar manner. The bottom row of diagrams correspond to field interactions with a different time ordering.

B.2 The Cumulant Expansion

To show the steps taken in the cumulant expansion we derive as an example the cumulant expansion of a one-point correlation function,

$$F(t) = \mu\langle \exp[i\int_0^t dt_1 \delta\omega(t_1)]\rangle. \tag{B.1}$$

The first step is to Taylor expand the expression for F to second order in the fluctuation (as in Eq. 2.26):

$$\begin{aligned} F = \mu\Big\{1 + i\int_0^t dt_1\langle\delta\omega(t_1)\rangle - \frac{1}{2}\int_0^t dt_1\int_0^t dt_2\langle\delta\omega(t_1)\delta\omega(t_2)\rangle + \cdots \\ + \frac{(-i)^{2n}}{(2n)!}\int_0^t dt_1 \ldots \int_0^t dt_{2n}\langle\delta\omega(t_1)\ldots\delta\omega(t_{2n})\rangle + \cdots\Big\} \end{aligned} \tag{B.2}$$

Now we make the ansatz that the one-point correlation function has the form

$$F \equiv \exp[-\mathcal{F}] \tag{B.3}$$

We expand $\mathcal{F}$ itself in powers of $\delta\omega$, with λ as the expansion parameter:

$$\mathcal{F} \equiv \lambda\mathcal{F}^{(1)} + \lambda^2\mathcal{F}^{(2)} + \cdots \tag{B.4}$$

If we now expand the ansatz in a Taylor series including this expansion of $\mathcal{F}$ and collect terms of like order we find

$$\begin{aligned} F &= 1 - (\lambda\mathcal{F}^{(1)} + \lambda^2\mathcal{F}^{(2)} + \cdots) - \frac{1}{2}(\lambda\mathcal{F}^{(1)} + \lambda^2\mathcal{F}^{(2)} + \cdots)^2 - \ldots \\ &= 1 - \lambda\mathcal{F}^{(1)} + \lambda^2\big(\mathcal{F}^{(2)} - \frac{1}{2}\mathcal{F}^{(1)2}\big) + \cdots \end{aligned} \tag{B.5}$$

Comparing this equation with the expansion of F in Eq. B.2 and solving for $\mathcal{F}^{(1)}$ and $\mathcal{F}^{(2)}$ we find

$$\begin{aligned} \mathcal{F}^{(1)} &= i\int_0^t dt'\langle\delta\omega(t')\rangle \\ \mathcal{F}^{(2)} &= \frac{1}{2}\int_0^t dt'\int_0^t dt''\langle\delta\omega(t')\delta\omega(t'')\rangle - \frac{1}{2}\Big[i\int_0^t dt'\langle\delta\omega(t')\rangle\Big]^2 \\ &= \int_0^t dt'\int_0^t dt''\langle\delta\omega(t')\delta\omega(t'')\rangle \end{aligned} \tag{B.6}$$

Thus our expression for F in the cumulant expansion truncated to second order is

$$F(t) = \mu \exp\Big[i \int_0^t dt' \langle \delta\omega(t') \rangle + \int_0^t dt' \int_0^t dt'' \langle \delta\omega(t') \delta\omega(t'') \rangle \Big] \tag{B.7}$$

These steps are performed similarly for a four-point correlation function.

B.3 Response Functions

All of the relevant diagrams contributing to the response of a three-level system in 3-pulse TFWM are shown in Fig. B.1. The response functions for time ordering $(\mathbf{k}_2, -\mathbf{k}_1, \mathbf{k}_3)$ in terms of the four-point correlation functions defined in Eqs. 2.63 and 2.64 and the lineshape function g of Eq. 2.74 are

$$\begin{aligned}
&(ma, mm, ma, aa) \; {}^2R_2^m(\tau_1, \tau_2, \tau_3) = {}^2F(\tau_3, \tau_2, \tau_1, 0)\mathrm{e}^{-i\omega_{ma}(\tau_1 - \tau_2 + \tau_3)}, \\
&(ma, aa, ma, aa) \quad {}^2R_3^m(\tau_1, \tau_2, \tau_3) = {}^2F(\tau_1, \tau_2, \tau_3, 0)\mathrm{e}^{-i\omega_{ma}(\tau_1 - \tau_2 + \tau_3)}, \\
&(ma, mn, ma, aa) \; {}^3R_2^m(\tau_1, \tau_2, \tau_3) = {}^3F(\tau_3, \tau_2, \tau_1, 0)\mathrm{e}^{-i\omega_{ma}(\tau_1 - \tau_2 + \tau_3) - i\omega_{mn}(\tau_2 - \tau_3)}, \\
&(na, aa, ma, aa) \quad {}^3R_3^n(\tau_1, \tau_2, \tau_3) = {}^3F(\tau_1, \tau_2, \tau_3, 0)\mathrm{e}^{-i\omega_{na}(\tau_1 - \tau_2) - i\omega_{ma}(\tau_3)}
\end{aligned} \tag{B.8}$$

The response functions in terms of the lineshape function g are

$$
\begin{aligned}
&{}^2R_2^m(\tau_1,\tau_2,\tau_3) = \mu_{am}^4 \mathrm{e}^{-i\omega_{ma}(\tau_1-\tau_2+\tau_3)} \\
&\times \exp\Big\{\frac{1}{2}\big[-g_{am}(\tau_3-\tau_2)+g_{am}(\tau_3-\tau_1)-g_{am}(\tau_2-\tau_1) \\
&-g_{am}(\tau_3)+g_{am}(\tau_2)-g_{am}(\tau_1)\big]\Big\}, \\
&{}^2R_3^m(\tau_1,\tau_2,\tau_3) = \mu_{am}^4 \mathrm{e}^{-i\omega_{ma}(\tau_1-\tau_2+\tau_3)} \\
&\times \exp\Big\{\frac{1}{2}\big[-g_{am}(\tau_1-\tau_2)+g_{am}(\tau_1-\tau_3)-g_{am}(\tau_2-\tau_3) \\
&-g_{am}(\tau_1)+g_{am}(\tau_2)-g_{am}(\tau_3)\big]\Big\}, \\
&{}^3R_2^n(\tau_1,\tau_2,\tau_3) = \mu_{am}^2\mu_{an}^2 \mathrm{e}^{-i\omega_{ma}(\tau_1-\tau_2+\tau_3)-i\omega_{mn}(\tau_2-\tau_3)} \\
&\times \exp\Big\{-\frac{1}{2}\big[\,2g_{am}(\tau_3-\tau_2)+2g_{an}(\tau_1) \\
&-g_{am}(\tau_3-\tau_1)+g_{am}(\tau_3)+g_{am}(\tau_2-\tau_1)-g_{am}(\tau_2) \\
&-g_{an}(\tau_2-\tau_1)+g_{an}(\tau_3)+g_{an}(\tau_2-\tau_1)-g_{an}(\tau_2) \\
&+g_{mn}(\tau_3-\tau_1)-g_{mn}(\tau_3)-g_{mn}(\tau_2-\tau_1)+g_{nm}(\tau_2)\big]\Big\}, \\
&{}^3R_3^m(\tau_1,\tau_2,\tau_3) = \mu_{am}^2\mu_{an}^2 \mathrm{e}^{-i\omega_{na}(\tau_1-\tau_2)-i\omega_{ma}(\tau_3)} \\
&\times \exp\Big\{-\frac{1}{2}\big[\,2g_{am}(\tau_1-\tau_2)+2g_{an}(\tau_3) \\
&-g_{am}(\tau_1-\tau_3)+g_{am}(\tau_1)+g_{am}(\tau_2-\tau_3)-g_{am}(\tau_2) \\
&-g_{an}(\tau_1-\tau_3)+g_{an}(\tau_1)+g_{an}(\tau_2-\tau_3)-g_{an}(\tau_2) \\
&+g_{nm}(\tau_1-\tau_3)-g_{nm}(\tau_1)-g_{nm}(\tau_2-\tau_3)+g_{nm}(\tau_2)\big]\Big\},
\end{aligned}
$$

with $m, n = b, c$; $m \neq n$.

Appendix C

Some Properties of Potassium

This appendix lists some properties of potassium relevant to the experiments and simulations. All frequencies are in inverse time (no 2π) unless otherwise stated.

Physical Quantity	D_1 **line**	D_2 **line**
Lines		
Resonance[1]	769.89645 nm	766.48991 nm
	389.393 THz	391.124 THz
	1.6104 eV	1.61756 eV
	$12,985\,\mathrm{cm}^{-1}$	$13,043\,\mathrm{cm}^{-1}$
Angular Frequency ω_0	2446.63 THz	2457.5 THz
Strengths[2]		
Oscillator strength f_{ik}	0.339463548	0.6817342151
Stat. weight, lower lvl g_i	2	2
Stat. weight, upper lvl g_k	2	4
Transition prob. A_{ki}	0.382	0.387

---

[1] from *A Physicist's Desk Reference*, Ed. H. L. Anderson, AIP Press, Springer (1989).

[2] *ibid.*

Physical Quantity	D_1 **line**	D_2 **line**

Linewidths[3]

Natural	0.0755279×10^{-3} nm 38.2 MHz 0.157982 μeV	0.0758408×10^{-3} nm 38.7 MHz 0.16005 μeV
Natural lifetime τ_k	26.2 ns	25.8 ns
Doppler (700 °C)	1.37497×10^{-3} nm 0.695423 GHz 2.87604 μeV	1.36888×10^{-3} nm 0.698513 GHz 2.88882 μeV
Resonance (700 °C)	1.61786 nm 0.818269 THz 3.38409 meV	2.26709 nm 1.15685 THz 4.78435 meV
Total (700 °C)	1.61927 nm 0.818984 THz 3.38704 meV	2.2685 nm 1.15757 THz 4.78732 meV
$1/\gamma_{tot}$	1.22103 ps	0.86388 ps
Exptl Linewidths[4] (700 °C)	1.88622 nm 0.954 THz 3.96294 meV	2.32422 nm 1.186 THz 4.88317 meV

Shifts[5]

Collisional shift coefficient β	$-0.05\,\mathrm{m}^3/\mathrm{ps}$	$-0.03\,\mathrm{m}^3/\mathrm{ps}$
Collisional shift (700 °C)	0.0583112 nm −29.4923 GHz	0.0346778 nm −17.6954 GHz

---

[3] *ibid.*

[4] from Thesis of J. Shacklette, University of Colorado (2001).

[5] from *A Physicist's Desk Reference*, Ed. H. L. Anderson, AIP Press, Springer (1989).

Physical Quantity	D_1 **line**	D_2 **line**
	−0.12197 meV	−0.0731822 meV
Lorentz-Lorenz Shift (700 °C)	0.08583 nm −43.4105 GHz −0.179531 meV	0.170092 nm −86.7943 GHz −0.358952 meV
Shifted Resonance (700 °C)	770.041 nm 389.32 THz 1.6101 eV	766.695 nm 391.019 THz 1.61713 eV

Other Quantities

Level splitting	3.40654 nm 1.73059 THz 7.15717 meV	
Shifted Level splitting (700 °C)	3.34591 nm 1.69901 THz 7.02653 meV	
Atomic Mass	39.0983 amu	
Thermodynamic properties[6]	melting 63.4°C	boiling 759.2°C[7]

---

[6] from [77]

[7] at 760 mm Hg

Appendix D

Experimental Details

In this appendix the details of the pulse picker and other experimental components are given.

D.1 The Pulse Picker

The pulse picker is based on the use of acousto-optic modulators (AOMs). In an AOM, acoustic waves create a strain-induced change in the index of refraction, resulting in optical beam diffraction. By modulating the acoustic waves with an RF signal it is possible to divide down the number of pulses in a pulse train by refracting some pulses and transmitting others. The control is enabled by a NIDAQ 6602 Counter/Timer on the computer. The pulse picker electronic design is shown in Fig. D.1.

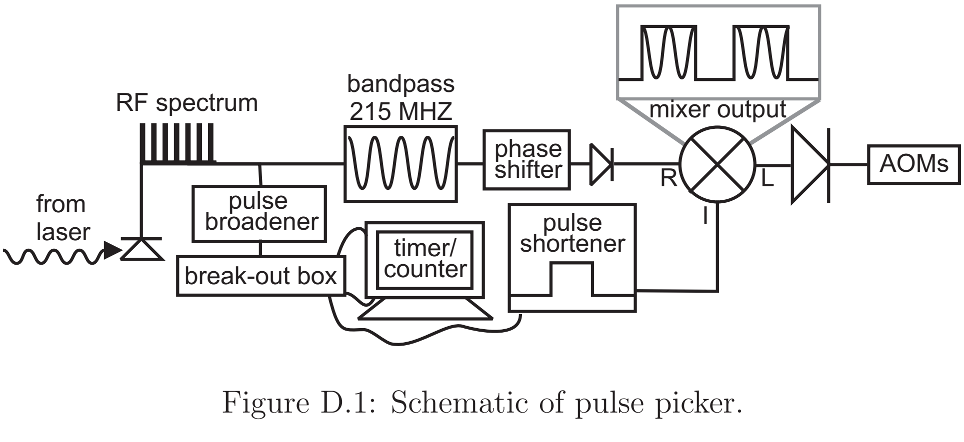

Figure D.1: Schematic of pulse picker.

Here we provide a brief overview of the components and appropriate inputs at various stages. We start with the photodiode-detected pulses from the laser, which are divided into two arms, here referred to as "First" and "Second."

First:

(1) take to tunable bandpass filter (remember to impedance match at input) and dial to $\sim$ 211 MHz RF frequency (use RF spectrum analyzer – remember to impedance match again). Note the filter is a linear device, so it doesn't matter which port is chosen for input/output.

(2) because the phase shifter cannot handle powers above 0 dBm, send the 211 MHz frequency to the phase shifter first

(3) then amplify the 211 MHz carrier with one ZAD-1 amplifier to about 1 V on the scope

(4) send it to the R port on the mixer

Second:

(1) take to pulse broadener and then to computer's source pin (PFI39)

(2) take from computer output and plug into input of pulse shortener; inside are three chips:

    - a comparator (makes analog signal into digital) and
    - two inverters (shifts pulse and "AND"'s it with unshifted pulse to create short pulse)
    - note the -5 V is used to remove any DC from the signal, and is connected directly to the output; technically this is not the best way to do it, but because the signal is so fast and short making a summer with the AD8561 op amp would be more complicated

(3) take output from pulse shortener and send it to the mixer's I port; note the mixer is somewhat leaky, so make sure there is not too much of the 211 MHz leaking through (check by unplugging the modulating pulse and looking at the L port on the scope); attenuate as needed

(4) send about 1 V to the big amp from the mixer and then to the AOM; a final output of about 5 V results in a good first-order diffraction; if more power is needed, attenuate less at the big amp input

Typical values for input/output at various important junctions:

- output from laser on scope: $\sim$ 140 mV direct from laser, $\sim$ 85 mV after 3-junction
- output from bandpass filter: $\sim$ 10 mV on scope and into phase shifter
- values going into / out of mixer:
  - R: 300 mV (after phase shifter and one amplifier ZFL-500LN)
  - I: 300 mV (attenuated by 10 dB after pulse shortener; is 1 V before 10 dB)
  - L: output $\sim$ 160 mV peak-to-peak (attenuated by 3dB before entering large amplifier; originally 225 mV peak-to-peak)
- input to large amps: $\sim$ 160 mV peak-to-peak
- output to AOMs: $\sim$ 9 V peak-to-peak (DC is $\sim$ 500 mV)
- AOM power (% of input) with unmodulated input: input $\sim$ 136 mW, output $\sim$ 13 mW; $\sim$ 9.5%.
- AOM power with modulated input: for 1/14, 210μW; for 1/21, 177μW

For second AOM, lower input/output of pulse shortener:

- values going into / out of mixer:
    - ∗ R: 400 mV (after phase shifter and one amplifier ZFL-500LN)
    - ∗ I: 800 mV (attenuated by 10 dB after pulse shortener; is 1.6 V before 10 dB)
    - ∗ L: output ∼ 200 mV peak-to-peak (attenuated by 3dB before entering large amplifier; originally 300 mV peak-to-peak)
- input to large amps: ∼ 200 mV peak-to-peak
- output to AOMs: ∼ 11 V peak-to-peak (DC is ∼ 100 mV)
- AOM power (% of input) with unmodulated input: input ∼ 125 mW, output ∼ 20 mW; ∼ 16%.
- AOM power with modulated input: for 1/14, 445μW; for 1/21, 405μW

D.2 Experimental Components

In this section a detailed description of experimental components used for the most general time-resolved three-pulse experimental setup is given.

The laser used for all of the experiments of this thesis is a home-built extended-cavity Kerr-lens mode-locked Ti:sapph pumped by a green laser. The pump laser is a Spectra Physics Millenia V diode-pumped CW laser (neodymium yttrium vanadate, $NdYVO_4$, gain medium) centered at 532 nm with a maximum power output of 5 W. The Millenia is usually set in power mode at 4 W for the experiments to extend the lifetime of the diodes, which were replaced in April of 2005. With this power the average modelocked Ti:Sapph output is approximately 380 mW. The Millenia laser is cooled by a Neslab RTE-III Chiller and controlled via the Millennia V control module. The T40 power supply is connected to a universal power supply to prevent damage from power outages, which had previously led to diode failure.

The Ti:sapph laser has an extended cavity with curved telescope mirrors from Newport (Part#10BV200UF.20, 25.4 mm dia, 2000 mm R, $R > 99\%$, 0-20 degrees, 710-890 nm). Figure D.2 is a diagram of the components with approximate distances. The cavity mirors have a $\sim$ 2-inch focal length. The Ti:sapphire laser rod is from Crystal Systems (3 mm $\phi \times$ 10mm PL, specs $\alpha 514 = 1.65$). The output coupler has 20% transmission (CVI PR2-750-80-1025).

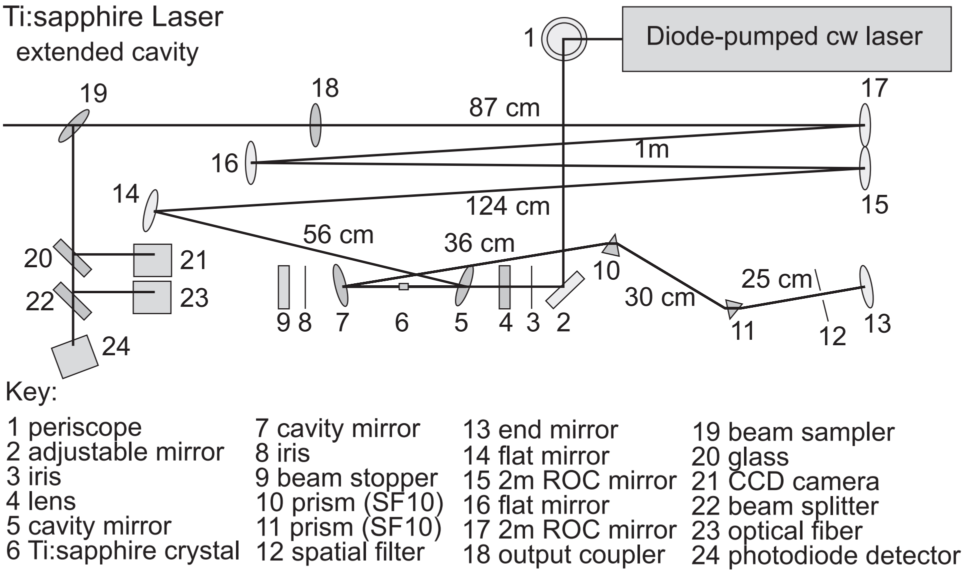

Figure D.2: Schematic of the Ti:sapph laser.

Immediately downstream of the laser two prisms (SF10) are used for dispersion compensation, with approximately 90 cm between prisms for the full setup. In addition, a 1 m focal length lens (Thorlabs LA1464-B) is placed immediately outside the laser to keep beam size small. The beam is then split up into four arms, two of which are focused down by 10 cm lenses (Thorlabs LA1509-B) into AOMs (Isomet 1250C) and recollimated. The reference arm includes two 10 cm lenses and a thick piece of glass to compensate for the lack of an AOM. To keep track of the spectral width without the need for an optical spectrum analyzer a sample of one beam is used to obtain a real-time trace of the spectrum using a slit, diffraction grating (Optometrics U.S.A., 1200 g/mm, 7500 blaze) and CCD camera. The camera image is sent to a Tektronix TDS210 Digital Real-time Oscilloscope triggered against a video synchronization generator. In general the mirrors used are Newport 10D20ER.2 silver-coated pyrex mirrors. Most of the beam samplers are wedged at 30' (CVI W1-IF-1012-UV-670-1064-45P) and the beamsplitters are also mostly wedged and vary in percentage (typically CVI FABS-800-45P-50-IF-1012-UV and CVI FABS-850-80-PW-45P). The stages used in the experiments are all from Newport:

- Newport MTM100CC.1, motor UE404CC, 25 cm stage
- Newport IMS500CCHA, motor UE511S2, 600 cm stage with a 1" diam. retroreflector (Newport UBBR1-2I)
- Newport MFN25PP, motor UE16pp, 25 mm stepper stage

The longer stage can be used for population measurements. The stages are controlled with a Newport XPS-C4 controller.

The temperature of the cell is controlled with an Omega CN8200 temperature controller with multiple ramp/soak capability. Usually only one ramp/soak sequence is used, typically taking 2 hours to reach 700°C from room temperature (~ 0.1 deg/sec). A Marshall color CCD camera and a monitor are used to check for spatial overlap and as a visual check for changes in the cell. A 150 W illuminator from RAM Optical Instrumentation with a tube neck was also used to view the cell. The autocorrelation trace is taken in a BBO crystal, with the red light blocked from entering the detectors by blue filters (e.g. Thorlabs FGB37). To obtain the upconverted signal a BBO crystal 0.5 mm thick was used, with a half-wave plate beforehand rotated such that optimal phase matching is achieved (i.e. the horizontally-polarized beams are rotated to be vertically-polarized and are then focused on a plane parallel to the table onto the BBO). To reduce noise sometimes the signals were focused with 5 cm lenses onto the detectors with $50\mu m$ pinholes. The detectors used to detect the signals were built in JILA (model CS022A2-02). They use a silicon photodiode, 1.5 mm diameter, 300 MHz, 6 pF; the signal gain is 1 MΩ. The detected signals are sent to two Stanford Research Systems 830 DSP lock-in amplifiers, connected via GPIB to a computer. The program used to control these components is written in Visual Basic. The data were analyzed in Origin or Mathematica.

Interference filters were used for spectrally-resolved excitation experiments (CVI F03-766.5-4-0.50 (3 nm BW) and CVI F1.5-769.9-4-0.50 (1.5 nm BW)). In addition, a 300 mm achromatic doublet lens was obtained for three-pulse experiments (Thorlabs AC508-300-B) along with a regular lens for collimation in transmission experiments (Newport KPX205AR.16 PCX BK7). In the three-pulse experiments of this thesis a 250 mm achromatic lens was used (Thorlabs AC508-250-B) along with a regular lens for transmission experiments (Newport KPX202AR.16 PCX BK7).

Appendix E

Novel High-Temperature Alkali Vapor Cell

Over the course of the work described in this thesis, novel high-temperature vapor cells were constructed with ever-improving design. These improvements are relevant for enabling the spectroscopy of alkali-metal vapors at high densities, which has been hampered by the extremely corrosive nature of these vapors at elevated temperatures. Early work used magnesium oxide windows for studies of potassium vapor up to 500°C [78]. Alkali-resistant glasses (for example Gelanite or 1720 glass) were developed for use at temperatures as high as 500°C. We have constructed novel potassium vapor cells for use in both reflection and transmission experiments that survive temperatures ranging from 25°C up to 800°C (densities up to 10^{19} cm^{-3}). The high-vacuum sapphire-to-titanium seals are achieved via diffusion bonding, without the need for gaskets or compression rings. The vacuum seal maintains its integrity for an average of 90 hours above 500°C with about 10 heating / cooling cycles.

E.1 Cell Design

The materials of titanium and sapphire were chosen based on their resistance to corrosion by potassium and their similar coefficients of thermal expansion. Grade-2 commercially pure titanium from the McMaster-Carr Supply Co. is machined for the body. Sapphire windows custom-made by Meller Optics are used for optical access. They have an anti-reflection coating on one side and are wedged in order to spatially separate the front and back reflections. The specifications for the sapphire windows are for c-axis orientation, 9.00 mm dia. × 0.50 mm thick, 0.50 degree wedge, A/R coated for maximum transmission at 768 nm on one face. See Figs. E.1 and E.2 for diagrams of the cell components. The screws are made of Inconel. The face of the cell is polished for bonding to the sapphire window.

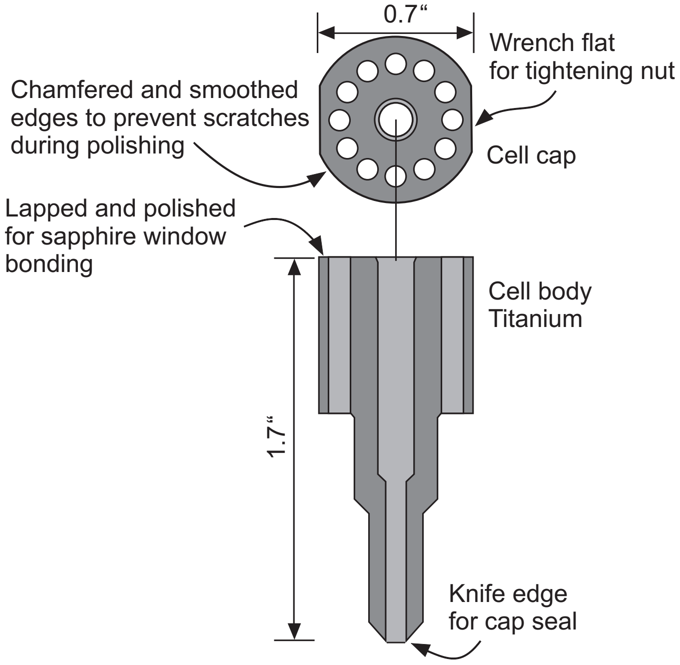

Figure E.1: Potassium cell components.

E.2 Bonding Procedure

We bond the sapphire to the titanium through diffusion bonding (this can be thought of as “welding” them together: apply pressure and heat to softening point of titanium). First the cell body is baked without the window to make sure debris are not released during bonding. The sapphire window is cleaned with methanol and set on top of the polished end of the cell, AR coating facing out. The window is pressed against the cell with a custom-made holder that applies

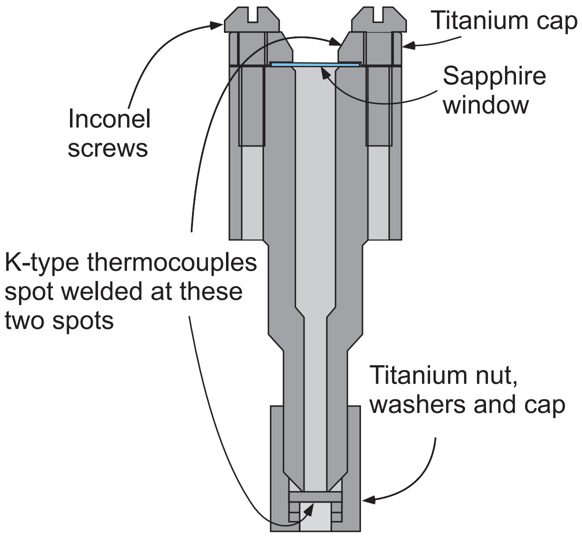

Figure E.2: The loaded potassium cell.

constant pressure across the outer diameter and placed inside a vacuum tube with a cylindrical current-controlled heater surrounding the tube. The cell is heated under vacuum at 800°C for 2 hours to bond the window to the cell. The ramp rate is set to reach 800°C from room temperature in about 4 hours.

E.3 Loading Procedure

To load the cell with potassium, we use a custom-made attachment on a vacuum system, shown in Fig. E.3. The attachment is in the shape of a “T” and has three openings, one to the pump, one for the empty cell and one for the nut, washers and cap that seals the cell once it is filled with potassium. It also has a cold trap to prevent particles from entering the pump.

Once the attachment is connected to the pump, we place the nut, washers and cap together into a wrench socket connected to a steel rod that allows us to tighten the nut with the washers and cap onto the cell inside the vacuum attachment. This is inserted into an arm of the attachment. We then load the potassium into the cell in a glove bag which has an opening connected to the

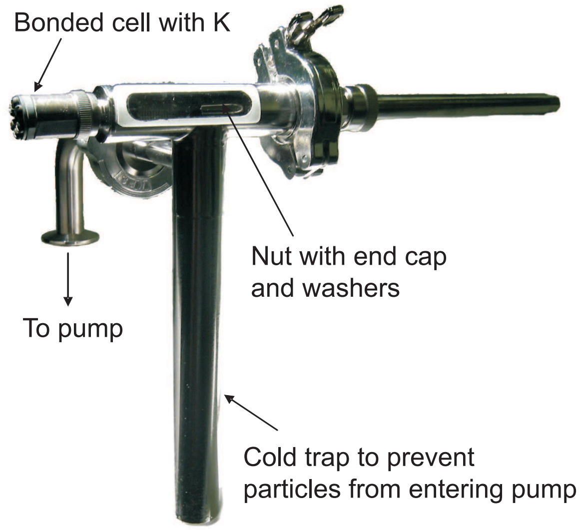

Figure E.3: Vacuum attachment for loading the cell.

other arm of the attachment. We fill the cell under an argon atmosphere to prevent the potassium from oxidizing and use a simple stainless steel scraper to place an amount of potassium corresponding to about a 2 mm diameter sphere into the back end of the cell. Once filled, we connect the cell, open side in, to its end of the attachment. Then we evacuate the cell to about 7×10^{-7} Torr using a turbo pump. At this point we screw on the nut to seal the cell while under vacuum until a torque meter reads about 60 inch-lbs and then close the valve to the turbo pump, vent to atmosphere and take out the assembled cell.

Thermocouples from Omega Engineering are then spot-welded onto the titanium both at the front of the cell by the window and at the back of the cell on the cap. We slip an oven custom-made for the cell onto the back end of the cell and bind the leads of the oven and thermocouples together with a stainless steel wire. The oven's body is made out of Sauerisen. Six leads come out of the oven, which fit into the holes drilled parallel to the cell body. The oven is designed to keep the temperature at the window a few degrees higher than the temperature at the nut in order to keep the potassium from pooling at the window. Nickel

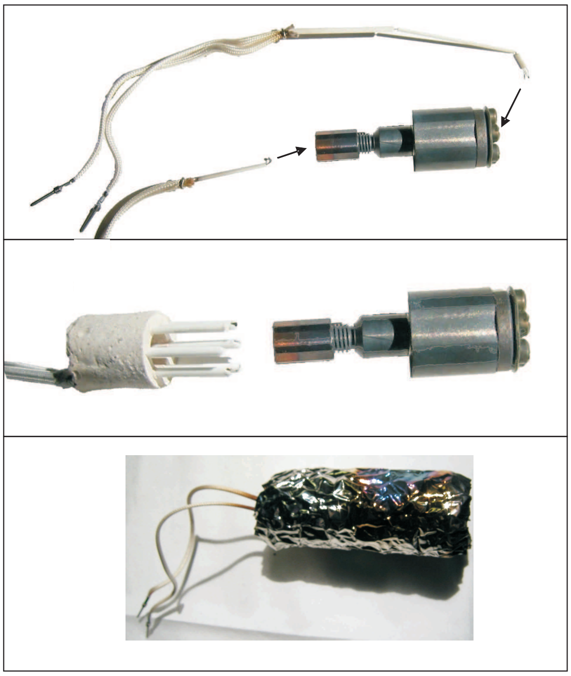

Figure E.4: Heating components attached to the potassium cell. Top: thermocouples are attached to the front and back of the cell, Middle: the oven leads fit into holes drilled parallel to the cell, Bottom: the cell is wrapped in nickel foil for heat shielding.

foil is cut and crinkled to wrap around the cell for heat shielding. Figure E.4 is a series of photos showing these steps.

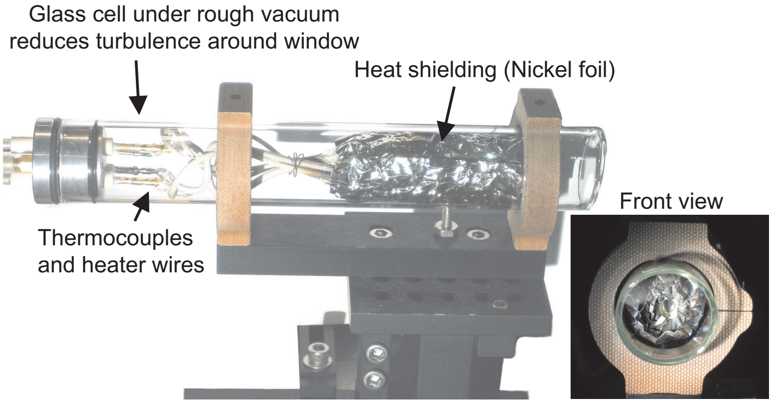

Figure E.5: Potassium vapor cell inside secondary glass cell to reduce turbulence and for heat shielding.

The wrapped cell is then put inside a secondary glass cell to reduce turbulence around the window and also for heat shielding (see Fig. E.5). The glass cell is in the shape of a hollow cylinder with length ∼8.5" and diameter ∼1.25". One end of the glass cell is closed at an angle to prevent back-reflections and the other end is open and can be sealed with a metal plug that is removable. The cell is placed so that the sapphire window faces the closed end of the glass cell. The wires from the oven and thermocouples are connected through the glass cell's plug for attachment to the temperature controller. The glass cell is pumped down to vacuum and the potassium cell is heated up to 300°C to allow the potassium to pool at the back of the cell. Figure E.6 shows the various pieces of the cell lined up for assembly and Fig. E.7 shows an assembled cell.

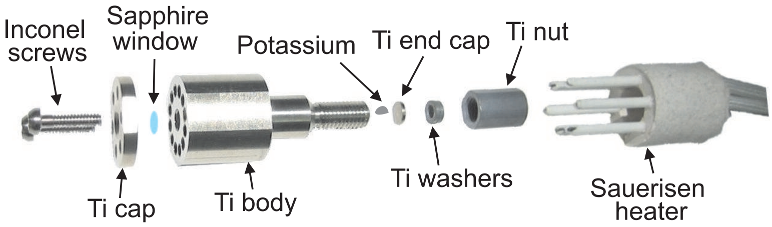

Figure E.6: Pieces of the vapor cell lined up for assembly.

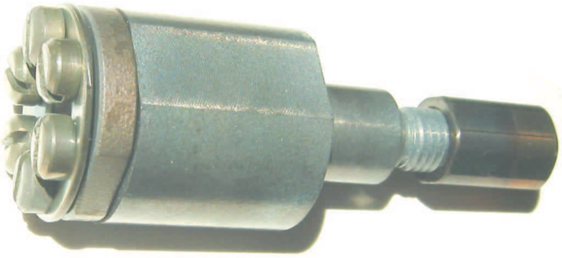

Figure E.7: An assembled vapor cell.

If the process goes well, the cell can last up to 130 hours above 500°C. The cells eventually fail at the titanium-sapphire interface. When the seal fails, a yellow film forms on the outside of the cell. Figure E.8 shows a cell whose titanium-sapphire seal failed. The lifetime (averaged over four cells) is about 90 hours (ranging from 85 to 108 hours) with about 10 heating/cooling cycles.

Figure E.8: A used cell.

E.4 Previous Designs

Here we present a brief record of past designs and how they were improved.

The "first generation" of vapor cells had bodies made of poly-crystalline alumina. Potassium was loaded in liquid form with a pipette into a molybdenum cavity. The sapphire window was bonded to the polycrystalline alumina with a high-temperature frit. These cells were more difficult to load and did not last as long as those of the current design.

The "second generation" of vapor cells had bodies made of titanium and sapphire windows like the current generation, but to assemble the cell, we set the window on top of the titanium cell, AR coating facing out, and placed three thin titanium washers on top of the window, followed by a cap and spring, and tightened it down with six screws. The cell was heated in this configuration for bonding. Using this method the rate of success was not as good as with the current method in which in the bonding process we apply pressure more carefully with a custom-made holder. The current method also does not require the use of the washers or pressure from the cap, making the process simpler. We also tried depositing a titanium ring onto the sapphire before attaching the window to the cell; this method did not make for better results.

E.5 Transmission Cell

Potassium has an absorption length on the order of a wavelength at the densities attained in these experiments. We made some progress towards a transmission cell thin enough for experiments at the lower densities. These cells would enable transmission experiments such as 2D Fourier transform spectroscopy, which would shed light on the coupling between levels and many-body effects. They would also allow more precise studies of propagation and local field effects. Figure E.9 is a schematic of the manufacturing process and Fig. E.10 is a photo of a thin cell. Initial success was fortuitous in that there was a leak in the holding packet, then made of stainless steel, just small enough to retain potassium during bonding and allow its release for experiments. A later attempt using silver as the holding packet successfully retained the potassium and released it as temperatures approached the melting point of silver, which is approximately 962°C, and seems a more reliable route. The primary remaining technical problem is how to keep the potassium from seeping into the thinnest parts of the cell, where it tends to remain due to capillary action. Figure E.11 shows transmitted TFWM data for a 14μm-thick cell, with dynamic beats due to propagation.

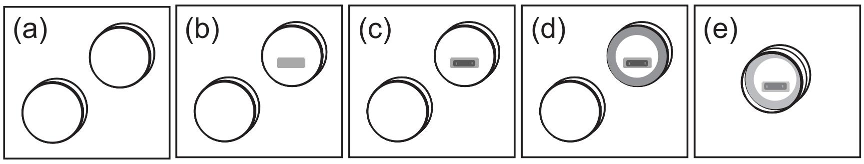

Figure E.9: Schematic of thin cell manufacture. (a) Two sapphire windows are used. (b) First a pocket is drilled into one of the sapphire windows. (c) Then a thin silver packet is filled with potassium and placed into the pocket. (d) A 6 μm-thin titanium washer is placed between the windows, which are then (e) sandwiched together and heated up to 800°C for bonding.

Figure E.10: Photo of thin cell.

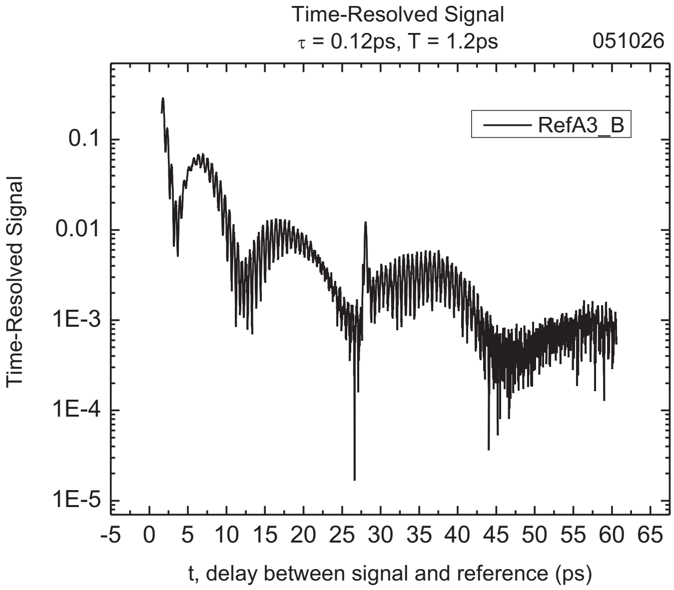

Figure E.11: Transmitted TFWM signal through a 14 μm-thick cell showing dynamic beats.

Appendix F

The Exciton Hamiltonian for a System of Two 2-Level Atoms

Here we derive the fluctuating exciton Hamiltonian for a system of two 2-level atoms. The fluctuating exciton Hamiltonian is

$$H_S = \sum_{m} \Omega_m \hat{B}_m^\dagger \hat{B}_m + \sum_{m,n}^{m \neq n} (J_{mn} \hat{B}_m^\dagger \hat{B}_n + K_{mn} \hat{B}_m^\dagger \hat{B}_n^\dagger \hat{B}_m \hat{B}_n), \tag{F.1}$$

where

$$\hat{B}_m^\dagger = |m1\rangle\langle m0| \tag{F.2}$$

and

$$\hat{B}_m = |m0\rangle\langle m1|. \tag{F.3}$$

For 2 atoms ($N = 2$) we have:

Atom basis → exciton basis:

atoms m, states a states e_m

$|ma\rangle|ma\rangle \rightarrow |e_m e_m\rangle$

1 ground state:

$|10\rangle|20\rangle \rightarrow |00\rangle$

$N = 2$ one-exciton states:

$|10\rangle|21\rangle \rightarrow |01\rangle$

$|11\rangle|20\rangle \rightarrow |10\rangle$

$N(N-1)/2 = 1$ two-exciton states:

$|11\rangle|21\rangle \rightarrow |11\rangle$.

We now write out the Hamiltonian explicitly:

$$\begin{aligned} H_S|00\rangle &= 0 \\ H_S|01\rangle &= \Omega_2|01\rangle + J_{12}|10\rangle \\ H_S|10\rangle &= \Omega_1|10\rangle + J_{21}|01\rangle \\ H_S|11\rangle &= \Omega_1|11\rangle + K_{12}|11\rangle + K_{21}|11\rangle \end{aligned} \tag{F.4}$$

$$H_S^{atom} = \begin{pmatrix} 0 & 0 & 0 & 0 \\ 0 & \Omega & J_{12} & 0 \\ 0 & J_{12} & \Omega & 0 \\ 0 & 0 & 0 & 2\Omega + 2K_{12} \end{pmatrix} \tag{F.5}$$

Now we diagonalize:

Solving to find the eigenvalues gives

$$\begin{aligned} &(\Omega - \lambda)^2 - J_{12}^2 = 0 \\ &\lambda^2 - 2\Omega\lambda + \Omega^2 - J_{12}^2 = 0 \\ &\rightarrow \lambda = \Omega \pm 1/2\sqrt{4\Omega^2 - 4(\Omega^2 - J_{12}^2)} = \Omega \pm |J_{12}| \end{aligned}$$

The eigenvectors then can be found using

$$\begin{pmatrix} \Omega & J_{12} \\ J_{12} & \Omega \end{pmatrix} = (\Omega \pm J_{12}) \begin{pmatrix} a \\ b \end{pmatrix}. \tag{F.6}$$

The equation

$$\Omega a + J_{12}b = (\Omega + J_{12})aJ_{12}a + \Omega b = (\Omega + J_{12})b \tag{F.7}$$

gives $b = a$, and the equation

$$\Omega a + J_{12}b = (\Omega - J_{12})aJ_{12}a + \Omega b = (\Omega - J_{12})b \tag{F.8}$$

gives $b = -a$. Thus the eigenvectors are

$$\left\{ \frac{1}{\sqrt{2}} \begin{pmatrix} 1 \\ 1 \end{pmatrix}, \frac{1}{\sqrt{2}} \begin{pmatrix} 1 \\ -1 \end{pmatrix} \right\} \tag{F.9}$$

To find the polarization, we use the relation $\hat{H}_{SF} = -\hat{P} \cdot \mathbf{E}(t)$, where $\hat{P} = \sum_m \mu_m (\hat{B}_m^\dagger + \hat{B}_m)$.

The eigenvectors written in the original space are then

$$\begin{aligned} |\alpha\rangle &= \frac{1}{\sqrt{2}} \begin{pmatrix} 1 \\ 1 \end{pmatrix} = \frac{1}{\sqrt{2}} \left[\begin{pmatrix} 0 & 1 \end{pmatrix} \begin{pmatrix} 1 \\ 1 \end{pmatrix} \begin{pmatrix} 0 \\ 1 \end{pmatrix} + \begin{pmatrix} 1 & 0 \end{pmatrix} \begin{pmatrix} 1 \\ 1 \end{pmatrix} \begin{pmatrix} 1 \\ 0 \end{pmatrix} \right] \\ &= \frac{1}{\sqrt{2}} (|01\rangle + |10\rangle), \end{aligned}$$

and similarly,

$$|\beta\rangle = \frac{1}{\sqrt{2}} (|10\rangle - |01\rangle) \tag{F.10}$$

So now we can write the polarization:

$$\begin{aligned} \hat{P}|00\rangle &= \mu_1|10\rangle + \mu_2|01\rangle \\ \hat{P}|01\rangle &= \mu_1|11\rangle + \mu_2|00\rangle \\ \hat{P}|10\rangle &= \mu_2|11\rangle + \mu_1|00\rangle \\ \hat{P}|11\rangle &= \mu_1|01\rangle + \mu_2|10\rangle \\ \hat{P}|\alpha\rangle &= \tfrac{1}{\sqrt{2}}[\mu_1|11\rangle + \mu_2|00\rangle + \mu_2|11\rangle + \mu_1|00\rangle] \\ \hat{P}|\beta\rangle &= \tfrac{1}{\sqrt{2}}[\mu_2|11\rangle + \mu_1|00\rangle - \mu_1|11\rangle - \mu_2|00\rangle] \\ \mu_1 &= \mu_2 = \mu \rightarrow \\ \hat{P}|\alpha\rangle &= \sqrt{2}\mu(|11\rangle + |00\rangle) \\ \hat{P}|\beta\rangle &= 0 \end{aligned} \tag{F.11}$$

$$P^{atom} = \begin{pmatrix} 0 & \mu & \mu & 0 \\ \mu & 0 & 0 & \mu \\ \mu & 0 & 0 & \mu \\ 0 & \mu & \mu & 0 \end{pmatrix} \tag{F.12}$$

The polarization in the exciton basis is (the columns and rows correspond to $\{|00\rangle, |\alpha\rangle, |\beta\rangle, |11\rangle\}$)

$$P^{exciton} = \begin{pmatrix} 0 & \sqrt{2}\mu & 0 & 0 \\ \sqrt{2}\mu & 0 & 0 & \sqrt{2}\mu \\ 0 & 0 & 0 & 0 \\ 0 & \sqrt{2}\mu & 0 & 0 \end{pmatrix}. \tag{F.13}$$

Appendix G

The GROMACS Package

This appendix gives directions on how to perform MD simulations using the package GROMACS. To perform a molecular dynamics simulation (commands are given in UNIX):

- modify grompp.mdp for T, P: change dt, nsteps, ref_t, ref_p, gen_temp e.g. type `emacs grompp.mdp &`
- modify topol.top for number of atoms
- modify conf.gro for box size. To simplify this step, run input.c with `gcc input.c` and then `./a.out`, which will create a conf.gro file with random atom positions
- ensure there are not over ten or so trajectory files (traj.) in the output folder, otherwise GROMACS won't overwrite. That is, delete traj.trr, .xtc files.
- type `grompp -v`
- type `mdrun -v`
- type `gmxdump -f > traj.dat` to convert the output to data files

- type `scp traj*.dat username@jilau1:/.` to secure shell copy to a more accessible location

To repeat this multiple times, run the program run.c with `gcc run.c` and then `./a.out`, which will ask you what temperature the run is for and will print out the input you would need for the number of runs you would like. Be sure to type `gcc input.c` after run.c and before inputing the lines from run.c.

To run interactively, type the command `qsub -IV` and be sure to `exit` when done. If the program reads/writes quite a bit, `cd` to /data. To allow opening of windows, type `ssh -X jilau1`.

Appendix H

Constants and Conversions

This appendix contains some handy constants and conversions related to the calculations performed in this thesis.

- Wavelength (m) to frequency (Hz):

  $\lambda\mathrm{To}\nu(\lambda) = \frac{c}{\lambda}$

- Frequency (Hz) to wavelength (m):

  $\nu\mathrm{To}\lambda(\nu) = \frac{\lambda}{c}$

- Wavelength difference (m) to frequency difference (Hz):

  $\delta\lambda\mathrm{To}\delta\nu(\lambda, \delta\lambda) = \frac{c}{\lambda^2}\delta\lambda$

- Frequency difference (Hz) to wavelength difference (m):

  $\delta\nu\mathrm{To}\delta\lambda(\nu, \delta\nu) = \frac{c}{\nu^2}\delta\nu$

- Frequency (Hz) to wavenumbers (cm^{-1}):

  $\nu\mathrm{Toinvcm}(\nu) = \frac{\nu}{100\ c}$

- Wavenumbers (cm^{-1}) to frequency (Hz):

  $\mathrm{invcmTo}\nu(\mathrm{invcm}) = 100 \cdot c \cdot \mathrm{invcm}$

- Temperature (K) to wavenumbers (cm^{-1}):

  $\mathrm{KToinvcm(K)} = \frac{k_B}{100\ h\ c}K$

- Wavenumbers (cm^{-1}) to Temperature (K):

  $\mathrm{incmToK(invcm)} = \frac{100\ h\ c\ \mathrm{invcm}}{k_B}$

- Joules (J) to wavenumbers (cm^{-1}):

  $\mathrm{Jtoinvcm(J)} = \frac{J}{100\ h\ c}$

- Electron volts (eV) to wavenumbers (cm^{-1}):

  $\mathrm{eVtoinvcm(eV)} = \frac{e \cdot eV}{100\ h\ c}$

- Wavenumbers (cm^{-1}) to electron volts (eV):

  $\mathrm{invcmToeV(invcm)} = 100\ h\ c\ \mathrm{invcm}/e$

- Hartree to wavenumbers (cm^{-1}):

  $\mathrm{HartreeToInvcm(Hart)} = \frac{E_h\ \mathrm{Hart}}{100\ h\ c}$

- Wavenumbers (cm^{-1}) to kcal/mole:

  $\mathrm{invcmTokCpM(invcm)} = 0.0028591 \cdot \mathrm{invcm}$

- kcal/mole to wavenumbers (cm^{-1}):

  $\mathrm{kCpMToinvcm(kCpM)} = \mathrm{kCpM}/0.0028591$

Table H.1: Constants

Physical Quantity	**MKSA Units**	**CGS “Gaussian”**
Speed of light (vacuum) c	2.99792458×10^{8} (m/s)	$2.99792458 \times 10^{10}$ (cm/s)
Electron charge e	$1.60217653 \times 10^{-19}$ (C)	4.803×10^{-10} (esu)
Boltzmann constant k_B	$1.3806503 \times 10^{-23}$ (J/K)	
Electron mass m	$9.1093826 \times 10^{-31}$ (kg)	$9.1093826 \times 10^{-28}$ (g)
Permittivity free spce ϵ_0	$8.854187817 \times 10^{-12}$ (F/m)	
Planck’s constant h	$6.6260693 \times 10^{-34}$ (Js)	
Classical electron radius r	$r = e^2/(4\pi\epsilon_0 mc^2)$ (m)	$r = e_{cgs}^2/(m_{cgs}c_{cgs}^2)$ (cm)
Avogadro’s number N_A	6.0221415×10^{23} (1/mol)	